



Technische Universität München

Fakultät für Maschinenwesen

Lehrstuhl für Bioverfahrenstechnik

Crystal Contact Engineering to Enhance
Protein Crystallization Processes

Phillip Grob

Vollständiger Abdruck der von der Fakultät für Maschinenwesen
der Technischen Universität München zur Erlangung des akademischen Grades
eines Doktors der Naturwissenschaften genehmigten Dissertation

Vorsitzender: Prof. Wolfgang Polifke, Ph.D.
Prüfer: 1. Prof. Dr.-Ing. Dirk Weuster-Botz
2. Prof. Dr. rer. nat. Michael Groll

Die Dissertation wurde am 28.05.2020 bei der Technischen Universität München
eingereicht und durch die Fakultät für Maschinenwesen am 20.10.2020 angenommen.

Acknowledgements

I wish to express my sincere appreciation to my doctoral supervisor, Prof. Dr.-Ing. Dirk Weuster-Botz, for providing excellent research conditions throughout the whole project time at the TUM Institute of Biochemical Engineering (BVT). The extraordinarily fair and transparent support was at any time the ideal balance between constructive criticism and sufficient flexibility.

There are many further essential contributors to this work I would like to thank:

Dr. Dariusch Hekmat and Johannes Hermann (both BVT) for fruitful, interdisciplinary discussions and several informative and entertaining DiSPBiotech status meetings and conferences.

All past and current BVT employees for technical and administrative assistance: Gabi, Ellen, Marlene, Markus, Norbert, Patrick, and Georg – thank you very much!

Dr. Dominik Maslak for great support with conception and realization of the scale up at the TUM Pilot Plant for Industrial Biotechnology.

Dr. Robert Janowski (Institute of Structural Biology, Helmholtz-Zentrum München), Dr. Sabine Schneider (Chair of Biochemistry, TUM), Dr. Tobias Schrader (Jülich Centre for Neutron Science), Dr. Andreas Ostermann (Heinz Maier-Leibnitz Centre, TUM) for crystallographic measurements and Johannes Hermann and Daniel Bischoff (both BVT) for refinements.

Cooperation partners in DiSPBiotech: Dr. Michael Barros-Groß (Prof. Kind, Institute of Thermal Process Engineering, Karlsruhe Institute of Technology KIT), Benjamin Radel (Prof. Nirschl, Institute of Mechanical Process Engineering and Mechanics, KIT), Philipp Vormittag, and Anna Wöll (both Prof. Hubbuch, Institute of Food and Biotechnology, KIT) for great collaborations and very pleasant get-togethers.

Annika Strauch (Prof. Buchner, Chair of Biotechnology, TUM) for CD measurements and Dr. Wouter Engelen (Prof. Dietz, Biomolecular Nanotechnology, TUM) for providing user time with RT-PCR equipment.

My students Jingyi, Philipp, Bianca, Angela, Kai, Luca, Dima, Charlotte, Jianing, Patric, Brigitte, and Max for planning and conducting this research with me – I learned a lot from you!

The funders: Deutsche Forschungsgemeinschaft (DFG) and TUM Graduate School.

And finally, all my colleagues at the Institute of Biochemical Engineering and the Professorship for Systems Biotechnology for lots of experimental support, mutual Foosball tournaments (especially Andrés, Markus, Ljubo, Burger, Luis, Jerry, Alex Z), BVT bike tours

Acknowledgements

Muc-Garch-Muc (Martin, Peter), the whole TUM Campus run team *OléOléBioVT*, tennis matches (Peter, Alex Z, Lukas), Comedy/Music/Magic sessions inside and outside of BVT (Nigel, Sayuri, Philipp, Andrés, Torben, Gui), Lederhosentraining (Xenia, Alex M, Torben, Andrés), BVT Christmas parties, and BVT excursions.

Contents

1	Introduction.....	1
2	Motivation and Objective	3
3	Theoretical Background	7
3.1	Proteins.....	7
	3.1.1 Structures and Fundamental Interactions.....	7
	3.1.2 Protein Engineering Strategies.....	12
	3.1.3 Biomanufacturing of Recombinant Proteins.....	13
	3.1.4 <i>Lactobacillus brevis</i> Alcohol Dehydrogenase (<i>LbADH</i>).....	17
3.2	Protein Crystallization	18
	3.2.1 Fundamentals	19
	3.2.2 Crystallization Methods and Agents.....	23
	3.2.3 Crystallography	25
	3.2.4 Protein Crystal Engineering	27
	3.2.5 Technical Protein Crystallization	29
4	Material and Methods.....	35
4.1	Material.....	35
4.2	Molecular Biological Methods.....	35
	4.2.1 Site-Directed Mutagenesis.....	35
	4.2.2 DNA Separation by Agarose Gel Electrophoresis	36
	4.2.3 DpnI Digestion	36
	4.2.4 Plasmid DNA Amplification, Extraction and Sequencing	36
	4.2.5 Molecular Subcloning.....	36
4.3	Bacterial Transformation and Protein Production.....	37
	4.3.1 Production of Chemically Competent Bacterial Cells	37
	4.3.2 Heat Shock Transformation of Chemically Competent Cells.....	38
	4.3.3 Recombinant Protein Production with <i>E. coli</i>	38
	4.3.4 OD ₆₀₀ and Biomass Determination.....	40
	4.3.5 Cell Harvest and Disruption	40
4.4	Protein Purification and Processing	41
	4.4.1 Preparative Chromatography	41
	4.4.2 Buffer Exchange and Protein Concentration	41

4.5	Protein Crystallization	42
4.5.1	Static μ L-Scale Crystallization	42
4.5.2	Stirred mL-Batch Crystallization	43
4.5.3	Crystal Dissolution and Recrystallization.....	45
4.5.4	Calculation of the Crystallization Yield	45
4.5.5	Phase Diagrams.....	46
4.5.6	Crystal Preparation for Neutron and X-Ray Crystallography	46
4.6	Protein and Crystal Analyses	47
4.6.1	Protein Concentration Analysis	47
4.6.2	<i>LbADH</i> Purity Analysis.....	47
4.6.3	Enzymatic Activity Assay.....	48
4.6.4	Stability Analysis	49
4.6.5	Automated Light Microscopy	50
4.6.6	Structural Analyses	50
5	<i>LbADH</i> Process Implementation from Gene to Crystal	53
5.1	Choice for <i>LbADH</i> as Exemplary Protein.....	53
5.2	Production and Crystallization of <i>LbADH</i> WT	54
5.2.1	Linker Modifications.....	54
5.2.2	Recombinant Production.....	55
5.2.3	1-Step Chromatographic Purification.....	56
5.2.4	Initial Crystallization	57
5.3	Crystallization Screenings.....	58
5.3.1	Setup for The Neutron Crystallography Screening.....	58
5.3.2	Setup for the Mutant Screening	60
5.4	Crystallography of <i>LbADH</i> WT.....	61
5.4.1	Neutron Crystallographic Structure.....	61
5.4.2	X-Ray Crystallographic Structure.....	61
6	Crystal Contact Engineering of <i>LbADH</i>	63
6.1	Engineering Strategies	63
6.2	Crystal Contacts of <i>LbADH</i>	64
6.3	Crystallization of <i>LbADH</i> Variants on the μ L-Scale	65
6.3.1	Significance and Reproducibility of Varying Crystallization Results ...	65
6.3.2	Characterization of Crystallizability	68
6.3.3	Mutant Screening on the μ L-Scale.....	70
6.3.4	Phase Diagrams of Selected Mutants	74

6.4	Structural Analysis of <i>Lb</i> ADH Mutants.....	76
	6.4.1 Crystal Packing	76
	6.4.2 Altered Crystal Contact Interactions.....	77
6.5	<i>Lb</i> ADH Double Mutants – Investigation of Synergetic Effects	81
6.6	Protein Analysis	82
	6.6.1 Enzymatic Activities	82
	6.6.2 Thermal Stability	85
	6.6.3 CD Spectra – Secondary Structure Analysis.....	87
6.7	Crystallization Across Different Agents and Buffer Systems	87
7	Stirred mL-Crystallization of <i>Lb</i>ADH Variants	89
7.1	Crystallization of Purified Proteins	89
	7.1.1 Reproducibility of Stirred-mL Scale Crystallization.....	89
	7.1.2 Impact of PEG and Protein Concentration on WT Crystallization	90
	7.1.3 Crystallization of <i>Lb</i> ADH Single Mutants.....	93
7.2	Crystallization from Microbial Cell Lysate.....	95
	7.2.1 Crystallization Kinetics of Single Mutants.....	95
	7.2.2 Crystallization Kinetics of Double Mutants	97
	7.2.3 Reproducibility of Stirred-mL Crystallization from Lysate.....	98
	7.2.4 Crystal Dissolution and Recrystallization	100
	7.2.5 Purification Effect and Yield of Crystallization and Recrystallization	102
8	Conclusion	105
9	Outlook	111
	List of Figures.....	113
	List of Tables	117
	List of Abbreviations	119
	List of Bibliography	121
	Appendices.....	133
A.	Material.....	134
B.	Arduino script	144
C.	Amino acid and DNA sequences	145
D.	Crystallization microphotographs.....	146
E.	Enzymatic activities	147
F.	Stability measurements	148
G.	Crystallization screens	149

1 Introduction

Biotechnology applies biological systems, such as natural occurring or genetically modified microorganisms and elements thereof, for economic purposes. Biotechnological methods, tools, and devices have evolved substantially over the last few years, and yet, the first biotechnological product dates to 6000 B.C., when the Sumerians in Mesopotamia brewed the world's first beer. It took a long time before Antonie van Leeuwenhoek (1632–1723) recognized that it was yeast that was responsible for alcoholic fermentation in the brewing process. The term *biotechnology* was mentioned in 1919 by Karl Ereky for the first time. At that time, he defined it as all lines of work by which products are produced from raw materials with the aid of living organisms.

Today, biotechnology as a term, does not really mean very much to mankind. Probably the sole fact of the interdisciplinary combination of many scientific fields such as chemistry, biophysics, biochemistry and microbiology prevents many people from developing a deeper interest. Consequently, the unknown, such as the genetic manipulation of crops, is still viewed with suspicion by a large part of society. Although there is no rational distinction possible of a drought-resistant rice plant resulting from random (but astonishingly undisputable) breeding strategies or from novel, targeted approaches, e.g. CRISPR/Cas gene editing, a general skepticism remains in modern society.

Biotechnology as an industrial and pharmaceutical sector, however, that provides life-supporting products, is accepted to a great extent. The human hormone insulin, for example, has been successfully produced in genetically modified bacteria since 1979 and replaced insulin isolated from animal pancreases (Brange 1987, Harrison 2015). Much more products from the biopharmaceutical sector have become indispensable over the last few decades for modern society, for example vaccines or antibodies for diagnostics and therapeutics. During the current SARS-CoV-2 pandemic, it is the biotechnology industry that will produce these key products. Next to the medical sector ('red biotechnology'), which makes up approximately 50% of the biotechnology turnover, biotechnology has become increasingly important in the industrial sector ('white biotechnology'). This sector offers solutions, which address the ubiquitous climate debate, by the production of bulk and fine chemicals derived from renewable carbon sources or by the usage of efficient biocatalysts, which help saving energy, for instance in laundry detergents.

Current biotechnology (increasingly referred to as 'synthetic biology') is greatly driven by significant recent improvements and cost-reductions in process automation, IT power ('artificial intelligence'), genetic tools (e.g. CRISPR/Cas), and quick in-house DNA synthesis

and sequencing. These building blocks all together accelerate research processes by enabling high-throughput screenings from gene to product, for example to find novel antibiotics. Hence, it can be expected, that many biotechnological, innovative ideas and compounds are just around the corner. Besides research, the bioprocess and the subsequent purification and formulation processes represent the biomanufacturing core that needs to be adapted individually for every new compound to convert new ideas into financially accessible products for customers or patients. Due to the continuously rising demand for biotechnological products, biomanufacturing unit operations must meet the increased demand. The cultivation process can be optimized by engineering both the process technology and the applied microorganisms. Downstream processes (DSP), such as purification and formulation, offer great variety and combination possibilities regarding purification technologies through various chromatographic, filtration, precipitation or crystallization approaches, which need to be adapted to the corresponding compound's properties and market demands.

2 Motivation and Objective

In biotechnological downstream processes (DSP), preparative chromatography is the most applied protein purification technology. However, DSP costs can exceed those of the preceding process steps by far if high purities of the target protein are required, as it is the case for therapeutic molecules, such as hormones or antibodies (Costioli *et al.*, 2010). Chromatographic resins are expensive and can only be applied for a limited number of process runs, before they must be renewed. Moreover, preparative chromatography is complex to scale-up and to perform continuously (Przybycien *et al.*, 2004). Since product titers in biotechnological cultivation processes have been increased continuously, e.g. by improvements in genetic engineering, preparative chromatography is becoming a DSP bottleneck that needs to be optimized (Shukla *et al.*, 2010; Natarajan & Zydney, 2013). One opportunity is the development and optimization of alternative purification methods. To date, there are only few alternative *Anything But Chromatography* purification methods in selected industrial applications, which are capable of replacing chromatographic steps: Aqueous two-phase systems, magnetic fishing, membrane separation systems, precipitation, and crystallization (Hammerschmidt *et al.*, 2015; Dos Santos *et al.*, 2016). However, these alternative purification approaches are preferable over chromatography only in distinct cases, which is why great effort is being made to optimize these partially re-emerging methods (e.g. crystallization) for broader application.

In this work, the focus is on technical protein crystallization as purification method. It requires no costly equipment and consumables, as well as less amount of buffer volumes, and thus addresses the key bottlenecks of preparative chromatography. Additionally, this method even benefits from continuously increasing product titers, since high concentrations of the target molecule increase the probability of supersaturation that triggers crystallization. From a technological perspective, all requirements are met for an effective process integration of protein crystallization as a purification step. The most prominent example, recombinant human insulin has been industrially crystallized from pre-purified solution for formulation purposes (Brange 1987, Harrison 2015). Recent various studies have shown that technical protein crystallization is a viable alternative to preparative chromatography, which enables high purity and high yields even in the presence of high impurity concentrations, allowing for a capture and purification step (Carbone & Etzel, 2006; Takakura *et al.*, 2006; Smejkal *et al.*, 2013b). Furthermore, technical crystallization, as a final polishing or formulation step, was validated with several enzymes and an antigen-binding fragment demonstrating high purities of $\geq 99\%$ after crystallization

and crystal washing (Hebel *et al.*, 2013b; Hekmat *et al.*, 2015c). Smejkal *et al.* demonstrated that the scalability of technical crystallization is most feasible via the maximum energy dissipation, providing an important solution to the initial scale-up issue (Smejkal *et al.*, 2013a). Recently, the first continuous crystallization of a monoclonal whole-length antibody from concentrated and dialyzed cell harvest was reported (Hekmat *et al.*, 2017).

Like biotechnology, protein crystallization as a purification method has not emerged recently. It was already applied in the middle of the 19th century by Hünefeld *et al.* for the purification of hemoglobin from the blood of an earthworm (Hünefeld, 1840). However, protein crystallization has mainly been used for the elucidation of a protein's three-dimensional structure, beginning with the first published three-dimensional structure of myoglobin (Kendrew *et al.*, 1958). To date, crystallography still is the most widely applied technique for structural analysis of macromolecules and thus, protein crystallization still is the fundamental prerequisite. However, principles of nucleation and crystal growth have only been superficially elucidated. The state of the art still is far off rational adjustment of parameters, such as pH, ionic strength, or type of crystallization agent, which enable crystallization of proteins. Instead, the identification of crystallization conditions still is the prevailing empiric approach with high-throughput screenings on a nano- or microliter-scale applying various conditions that have been demonstrated in the past to induce protein crystallization for certain proteins. This empiric procedure also represents the first step of an industrial application of protein crystallization and in spite of the ongoing progress in screening automation, this step still is a major bottleneck, which limits the applicability of technical crystallization to a small number of industrial or pharmaceutical proteins.

For crystallographic purposes, Lawson *et al.* were the first having the idea to engineer a protein in such a way that it crystallizes and exhibits sufficient diffraction capability of X-ray beams (Lawson *et al.*, 1991). Other successful early work followed, which focused on protein engineering to generally enable and enhance crystallizability. It was found that single amino acid exchanges can have a distinct effect on the crystallization properties of the protein (Mc Elroy *et al.*, 1992; Jenkins *et al.*, 1995; D'Arcy *et al.*, 1999). A general engineering strategy towards enhanced crystallizability was developed by Derewenda's group, the so-called Surface Entropy Reduction (*SER*) strategy, which intended to generate 'low-entropy' surface patches leading to improved crystal quality for X-ray crystallography of a number of engineered proteins (Longenecker *et al.*, 2001; Derewenda & Vekilov, 2006; Derewenda & Godzik, 2017).

So far, to the best to the author's knowledge, no studies were published on engineering proteins towards improved technical crystallization, that is, enhanced crystallization kinetics instead of improved diffraction quality. In the present work, the effectiveness of protein engineering, to render a protein more prone to technical crystallization, was investigated. Therefore, the industrial biocatalyst *Lactobacillus brevis* alcohol dehydrogenase (*LbADH*) was chosen as exemplary protein and the in-house process implementation from gene to crystal was approached. Answers and experimental solutions to the following questions were targeted:

- i. Crystallization is often referred to low **reproducibility** – is it possible to trace varying crystallization behavior back to single amino acid exchanges? Is the effect of a single amino acid exchanges significant enough (and environmental or process variations minimal enough)?
- ii. What parameters define '**improved technical crystallizability**' and how can mutants be screened and characterized experimentally on a high-throughput μL -scale?
- iii. How could a rational **engineering strategy** look like?
- iv. Can **crystallographic methods** help to validate the engineering approach and elucidate altered crystallization behavior at the **atomistic level**? Is the **crystal packing** preserved when amino acids are exchanged at the wild-type's (WT) crystal contacts or does an unpredictable reorientation of crystal contacts occur?
- v. How do amino acid exchanges influence the **protein's intrinsic properties**, such as structure, stability, and catalytic activity?
- vi. What are the effects of protein engineering on crystallization on a **larger scale in stirred crystallizers**? Are crystallization results reproducible and transferable from previous screening conditions (static μL -scale)? Can technical crystallization of engineered *LbADH* variants be applied for capture and purification?

Summarized, the present work should elucidate whether protein engineering is applicable to generate mutants with improved properties for technical protein crystallization. For this purpose, an experimental setup should be implemented that allows a balance between a) fundamental molecular biological, biochemical, and crystallographic investigations (engineering strategies and structural analysis), and b) application-oriented, process engineering investigations (crystallization as a purification method).

3 Theoretical Background

3.1 Proteins

Every cell of any organism is mainly composed of the four major types of biological macromolecules: Lipids, carbohydrates, nucleic acids, and proteins. These macromolecules are all organic, meaning that they contain carbon. Inside and outside the cells they are responsible for a wide range of highly diverse functions. In biotechnology, all four macromolecule classes are modified and produced, whether for research or application purposes. This chapter focuses, as does the entire present work, on the class of proteins.

3.1.1 Structures and Fundamental Interactions

Proteins are commonly characterized at four structural levels: Primary, secondary, tertiary, and in certain cases the quaternary structure.

The **primary structure** is the linear sequence of amino acids in the polypeptide chain that predetermines the native three-dimensional structure of each protein. An amino acid is chemically linked to another amino acid (or a sequence) by the formation of a peptide bond between its amino nitrogen and the partner amino acid's carboxyl carbon (amide linkage) (see **Figure 3.1**). 20 natural amino acids are encoded in the genetic code. They are distinguished by their characteristic side chain (see **Figure 3.2**). Common methods to investigate the length of the linearized protein is SDS-PAGE or mass spectrometry.

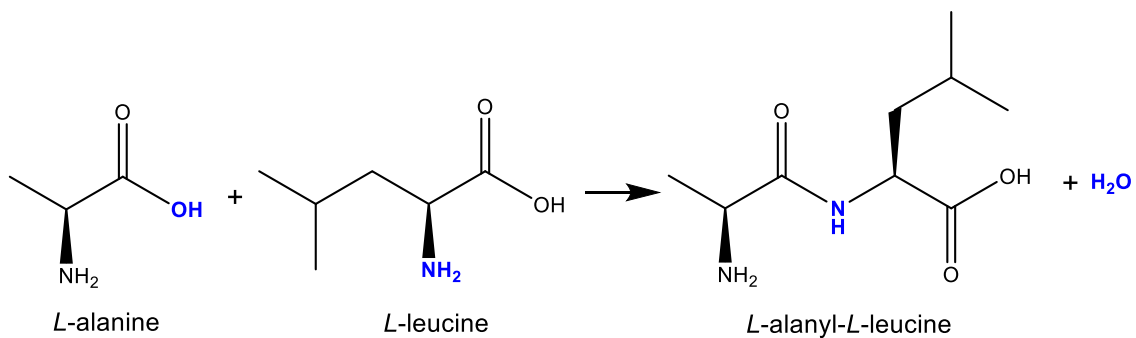
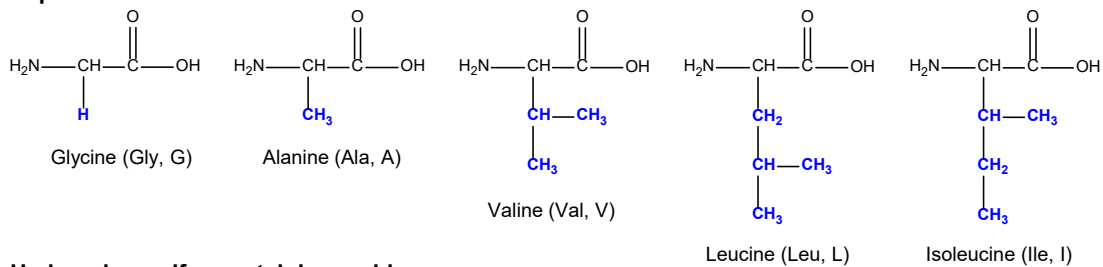
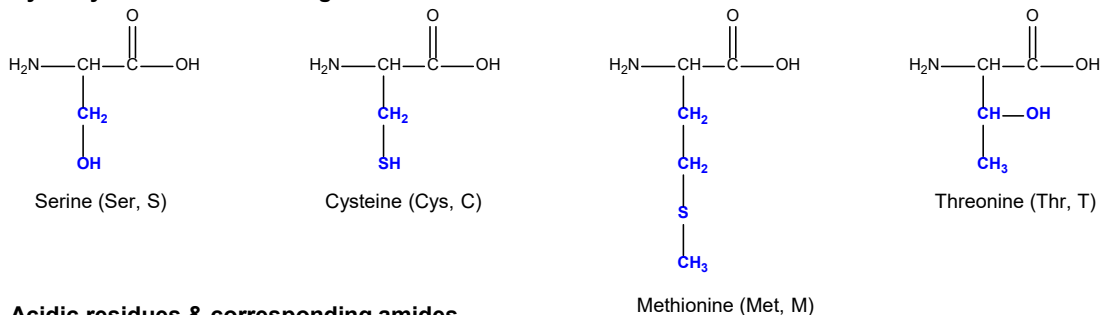


Figure 3.1: Two amino acids (alanine + leucine) forming a dipeptide (peptide bond via amide linkage) and a water molecule. (The figure was created using ChemDraw v19.0).

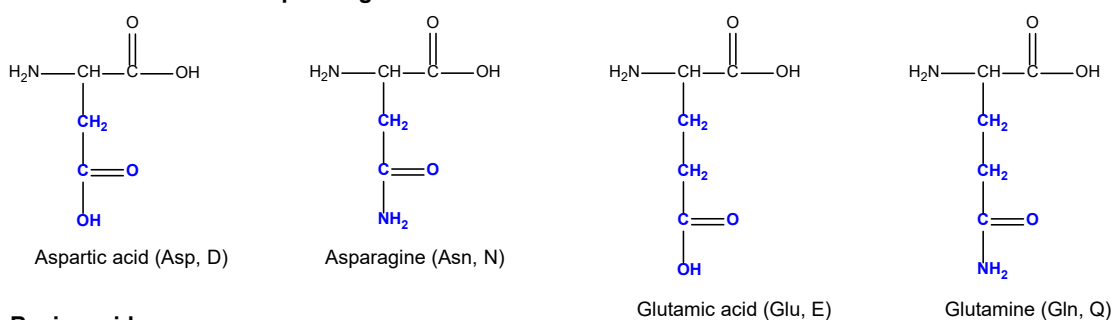
Aliphatic residues



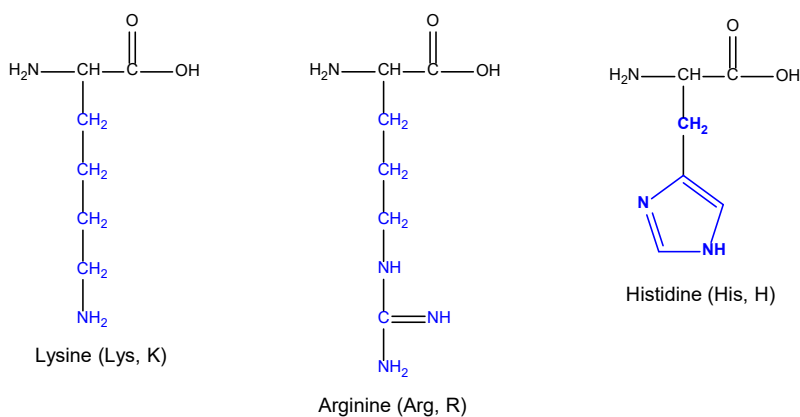
Hydroxyl or sulfur containing residues



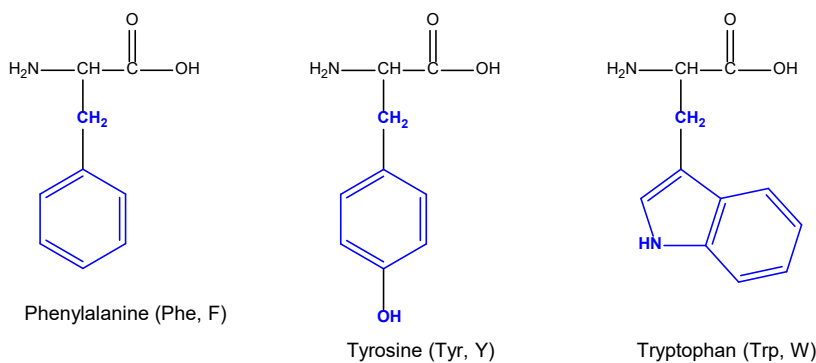
Acidic residues & corresponding amides



Basic residues



Aromatic residues



Special case

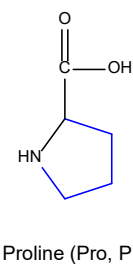


Figure 3.2: Chemical structures of all 20 encoded proteinogenic amino acids, categorized according to their residue's biochemical characteristics. Residues are depicted in blue. Three-letter and one-letter codes are given in brackets. (The figure was created using ChemDraw v19.0).

Secondary structures are mainly composed of α -helices and β -sheets. These are coordinated by hydrogen bonding between the partially negative oxygen and the partially positive nitrogen of the protein backbone, resulting in structures with high stability. The α -helix is a usually right-handed coil, stabilized by hydrogen bonding between every fourth amino acid. The most frequent amino acids in α -helices are alanine, leucine, and glutamate. The least frequent are proline, glycine, and aspartic acid (Davies, 1964). β -sheets are developed when two distinct regions of the amino acid sequence are interfering side-by-side (parallel or antiparallel) via hydrogen bonding. The β -turn is a structural element that often connects antiparallel β -sheet strands. Additionally, cation- π interactions – the interactions between positively charged amino acids lysine and arginine with aromatic residues tyrosine, phenylalanine, and tryptophan – play an important role in secondary structure stabilization, especially in α -helices (Gallivan and Dougherty, 1999). It was shown that arginine is more likely involved than lysine; among the aromatic residues, tryptophan occurs most frequently in cation- π interactions. Similarly, salt-bridges have been reported additionally as stabilizers of α -helices and β -sheets (Donald *et al.*, 2010). Common methods to investigate secondary structures are circular dichroism (CD) or nuclear magnetic resonance spectroscopy (NMR).

The combination of several secondary structures and flexible, unfolded regions result in a three-dimensional structure, the **tertiary structure**. During the process of protein synthesis, secondary structures form first. Hydrophobic amino acids fold towards the center of the protein. A study of Pace *et al.* concludes that hydrophobic effects contribute ~60% and hydrogen bonding ~40% of a protein's stability (Pace *et al.*, 2011 and 2014, respectively). Van der Waals forces are the dominant contributor to attractive interactions involving the aromatic amino acids phenylalanine, tyrosine, and tryptophan within the hydrophobic core, resulting in aromatic π - π stacking. Aromatic systems are predominantly attracted by van der Waals forces and the stabilization energy in the benzene dimer is rather small (Riley & Hobza, 2013). Three attractive geometries of aromatic residues are the T-shaped, the edge-to-face, and parallel-displaced conformation (see. **Figure 3.3**).

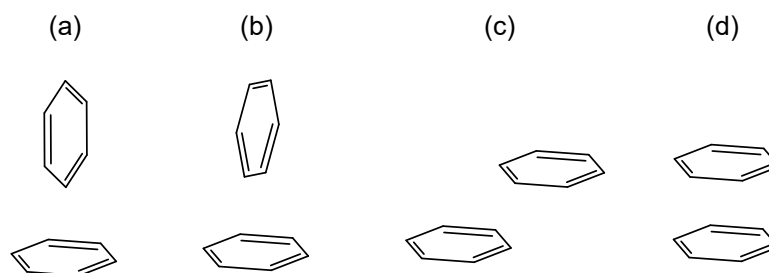


Figure 3.3: Illustration of attractive (a–c) and repulsive (d) π - π interactions of aromatic rings (represented by two facing benzenes). Different conformations: (a) T-shaped, (b) edge-to-face, (c) parallel-displaced, (d) parallel-stacked. (Adapted from Neel *et al.*, 2017; created using ChemDraw v19.0).

Burley and Petsko studied 34 proteins and summarized that 60% of aromatic residues are involved in π - π stacking, where the T-shaped arrangement was the most prominent one (Burley and Petsko, 1985). Contrary to this study, McGaughey concluded that the parallel-displaced geometry is the most frequent one (McGaughey *et al.*, 1998). Also, salt bridges are beneficial interactions by connecting secondary structures and contribute to folding kinetics (Donald *et al.*, 2010). Thermal stability of tertiary structures can be due to an increase in the number of salt bridges and aromatic residues, and in increased hydrophobicity, as concluded from studying thermophilic proteins (Zhou *et al.*, 2008; Fields *et al.*, 2015). Tertiary structures can be experimentally assessed by crystallography or NMR. With regard to recombinant protein production, the folding process often is a critical point, since the correct folding depends on a broad range of factors which need to be identified in order to prevent unfolded proteins (inclusion bodies), e.g. the right choice of expression system, the metabolic burden (stress level), temperature, etc. In many cases, already the tertiary structure represents the native structure of a protein, which fulfills the desired stability, shape, and functionality (e.g. catalytic activity).

Other proteins are only functional when two (dimers) or more monomers (oligomers) are combined to a **quaternary structure**. The quaternary structure is maintained by covalent disulfide bonds and/or by non-covalent bonds, such as aforementioned cation- π interactions or salt bridges. Quaternary structures can be visualized by crystallography, NMR or cryo-electron microscopy (cryo-EM). Types of quaternary structures are further discussed in the following.

Intermolecular Interactions

In the previous section various *intramolecular* interactions were described to build secondary, tertiary, and quaternary structures. The formation of a quaternary structure is a combination of individual molecules and can therefore be considered as a permanent *intermolecular* connection. Types of protein-protein interactions were comprehensively reviewed by Nooren & Thornton (2003). All the interaction possibilities mentioned in the previous section are prevalent also in the binding process of proteins with other proteins or with other classes of molecules.

Homo- and hetero-oligomeric complexes: Hetero-oligomers consist of non-identical monomers. Homo-oligomeric proteins consist of identical monomers, such as *Lactobacillus brevis* alcohol dehydrogenase (*LbADH*). The latter group can be further differentiated into isologous complexes (same surface on both monomers is involved, leading to a 2-fold symmetry), and heterologous complexes (using different interfaces, leading to infinite aggregation).

Obligate and non-obligate complexes: Protomers of non-obligate complexes also exist individually (e.g. in receptor-ligand or enzyme inhibitor interactions). Protomers of obligate complexes are instable on their own, e.g. the obligate homodimer Arc repressor of bacteriophage P22. The interfaces of the latter group were shown to be more hydrophobic, more densely packed, less planar and with fewer hydrogen bonds than non-obligate complexes (Jones and Thornton, 1996).

Permanent and transient complexes: Permanent complexes reveal very stable interactions, which need a molecular trigger to dissociate (e.g. the membrane-associated complex of heterotrimeric G protein). In contrast, transient complexes have a reduced complexed lifetime, and thus interactions are formed and split up continuously and can be controlled by slight environmental changes, for instance pH changes, as reported for lysin (Nooren & Thornton, 2003).

Besides protein-protein interactions, proteins have evolved to also bind other types of macromolecules, such as DNA or RNA. In these cases, π -stacking between nucleic acids and aromatic residues are often involved in protein/DNA and protein/RNA binding processes, which is of high importance at transcription and translation (Riley and Hobza, 2013). Other interactions, such as carbohydrate-protein interactions for cell communication are predominantly coordinated by CH- π interactions (Asensio *et al.*, 2013).

Cation- π interactions represent the interactions between the positively charged amino acids lysine and arginine with aromatic residues. Besides the stabilization of the intramolecular structure of proteins, these strong non-covalent, electrostatic forces were shown to be responsible for ligand-receptor interactions, which is relevant in engineering biopharmaceutical proteins (Dougherty 2007).

3.1.2 Protein Engineering Strategies

Protein engineering is used to improve a protein towards one or more selected properties or to generate these properties *de novo*. Industrially applied enzymes are usually used under harsh conditions, for example at high temperatures or at high acidity or alkalinity, far away from physiological pH. Therefore, the engineering approaches of most industrially applied enzymes have been focusing on improved stability at industrial conditions and simultaneously on the preservation of the catalytic activity. The engineering strategies are mainly divided into rational and random approaches.

For rational approaches protein structural analysis, such as X-ray crystallography, is a highly relevant method that enables site-directed engineering. A higher stability (higher melting temperature, T_m) of proteins can be achieved in different ways. Common is the introduction of extra cysteines, which are in proximity in the folded protein and form disulfide bonds in an oxidizing milieu (e.g. in the bacterial periplasm). Additionally, existing cavities in the center of a protein can be filled with larger, mainly hydrophobic amino acids, such as phenylalanine, to reduce the conformational freedom, and thus to reduce structural alternatives to the native state. At the surface, especially neutral asparagine and glutamine are prone to convert to the corresponding acids aspartic and glutamic acids under harsh conditions. Since the different biochemical properties of these negatively charged acids might lead to conformational changes at the active site, one approach is to substitute asparagines and glutamines with similar uncharged and hydrophilic residues, such as threonine. In other cases, proteins are redesigned to accept less expensive cofactors, e.g. NAD(H) instead of NADP(H). Here, amino acid exchanges need to be targeted near the enzyme's active site, to be more precise, on the 'bottom' of the cofactor binding pocket. Since NAD(H) lacks one negatively charged phosphate group, the binding pocket of enzymes favoring NAD(H) over NADP(H) is smaller and reveals a more negatively charged binding pocket. Similarly, a substrate binding site can be engineered towards novel or enhanced substrate acceptance. In particular, when engineering the enzymatic activity, the three-dimensional structural knowledge about the target protein is of high importance. A semi-rational engineering approach by site-directed saturation mutagenesis can be an alternative technique. For instance, when putatively relevant amino acid positions can be restricted to a few, but the most suitable amino acid residues cannot be estimated (e.g. engineering towards artificial cofactors, Campbell *et al.*, 2012). In this case, degenerated oligonucleotides are applied during PCR (saturation mutagenesis).

A contrary engineering approach has been proved to be efficient in case there is no protein crystal structure available or if rational approaches have not succeeded, e.g. due to unknown conformational effects. It is covered by the term directed evolution and is

characterized by random mutagenesis (e.g. by error-prone PCR) and high-throughput screening of resulting mutants (e.g. by phage display).

An alternative strategy is domain swapping, which is applied when single domains can be assigned to specific functions, which is then transferred to another protein. In this case, *de novo* functionalities can be introduced as applied for transcription factors or restriction enzymes (Younger *et al.*, 2018). Also, the transfer of unstructured loop regions ('loop swapping') was reported as highly effective in the case of changing cofactor preference of an ene reductase from NADPH to NADH (Mähler *et al.*, 2019).

Many further strategies exist. However, what applies to all engineering approaches is the statement made by Nobel Prize winner Francis H. Arnold (2018): "*you get what you screen for*" (Arnold, 1998). Arnold suggests that most of the experimental effort of directed evolution is put on validation and implementation of a suitable screening method. This statement can also be transferred to approaches where isolated and specific amino acid exchanges are performed.

3.1.3 Biomanufacturing of Recombinant Proteins

Biomanufacturing is the industrial production of compounds applying biological organisms or parts thereof in a scalable process. Due to the vast variety of organisms and products the biomanufacturing processes are highly diverse. It starts with the fact that fundamentally different organisms or cells from microbial, fungal, plant or mammalian source are applied, which reveal distinct growth and production optima. The products are also highly diverse and range from low-cost bulk chemicals, such as alcohols or acids, to more complex chemical structures, such as antibiotics, and from industrial biocatalysts to highly purified and high-value therapeutics, such as antibodies, hormones or vaccines. The produced industrial biocatalysts can in turn be applied in cell-free biotransformations in which these biocatalysts might catalyze the conversion of special chemicals in a well-defined, cell-free environment (Abdelraheem *et al.*, 2019). A prominent example is the use of immobilized glucose isomerase in high fructose corn syrup (HFCS) production (Bhosale *et al.*, 1996).

In general, the provision of recombinant proteins – for therapeutic, diagnostic, or industrial use – consists of two main process steps: The recombinant production with cells in stirred-tank reactors and the purification step. The latter process, the so-called downstream process (DSP), covers all steps from the crude fermentation broth that leaves the bioreactor to the final formulated biotechnological product. Some industrial protein applications are resistant towards impurities, such as host cell compounds, medium salts, or metabolites, and thus no or only few purification steps are required. Other applications, especially for diagnostic or therapeutic purposes, require highly purified proteins. In the latter case, a series of

consecutive process steps is necessary (illustrated in **Figure 3.4**). Cell-liquid separation can be realized by filtration or centrifugation. In case of intracellular protein production, the cells must be disrupted, and the cell debris clarified, whereas secretory pathways offer the advantage that these process steps are omitted.

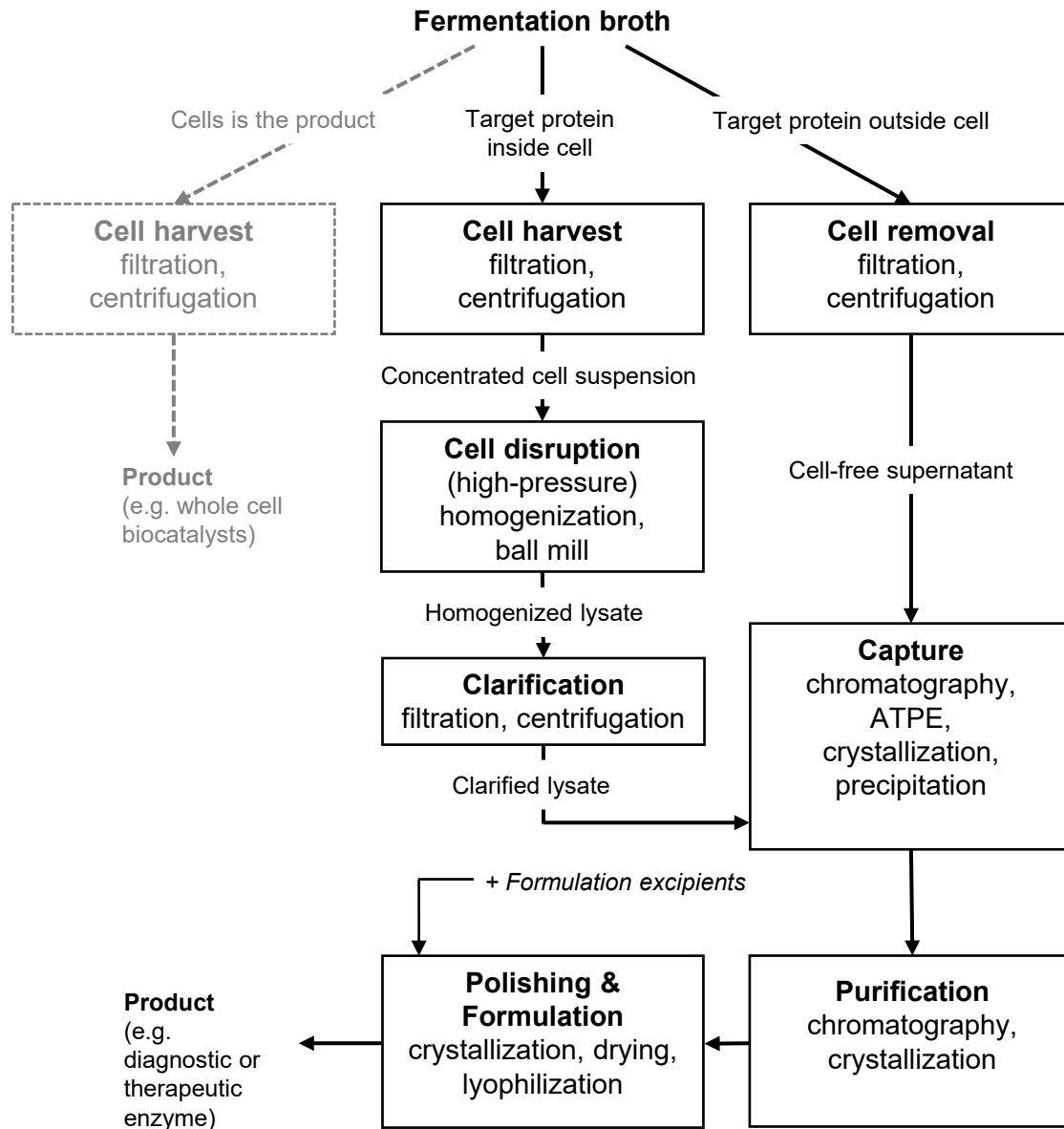


Figure 3.4: Schematic DSP illustration from crude fermentation broth to purified and formulated recombinant proteins. Since the cells themselves can also represent the final product (e.g. whole cell biocatalysts), these are also shown for the sake of completeness (left, dashed illustration). APTE = aqueous two-phase extraction. (Scheme modified from Doran, 2013.)

In general, DSP can be divided into capture, purification, polishing, and formulation. Capture is the initial isolation of the target. Substances are removed having substantially varying properties compared to the target molecule. Moreover, the reduction in volume is targeted by concentration. The subsequent purification step aims to remove remaining

impurities, which typically have similar chemical or physical properties, and to further concentrate the target protein. The final polishing and formulation steps are used to remove residual liquids and to bring the target into the desired storage or dosage form, if possible, with a preference for crystalline formulation (discussed in the following).

Among the existing great variety of capture and purification steps of the target molecule, which are industrially used, preparative chromatography is the most applied one. Alternatives are aqueous two-phase extraction, crystallization, precipitation and combined, methods, depending on the properties of the protein. In many processes, especially where high levels of purity are required, DSP costs can significantly exceed the costs of the preceding process steps (Costioli *et al.*, 2010). Therefore, the development of purification techniques is persistently relevant, as they have the greatest potential for reducing the overall process costs.

Selected Industrial DSP Methods

Chromatographic processes make use of the different affinities of usually dissolved molecules (mobile phase) towards a specific resin (stationary phase). All chromatographic processes are relatively slow separation processes because of diffusion limitation within the porous particles. Different types of chromatography particles (resins) have evolved for the purification of proteins. Common chromatographic methods are ion exchange, hydrophobic interaction, size exclusion, and affinity chromatography. **Ion exchange (IEX)** resins are derivatized with ionic groups divided in anion and cation exchangers. Anion exchangers (AEX), e.g. diethylaminoethyl cellulose (DEAE, $C_2H_4N^+H(C_2H_5)_2$, $pK_a \approx 9$) are basic, positively charged compounds, which attract opposite charged molecules (anions). Cation exchangers (CEX), e.g. carboxymethyl cellulose (CM, CH_2COO^- , $pK_a \approx 5$) carry negatively charged groups, and thus attract cationic molecules. The choice of method depends on the stability of the target proteins in the applied process buffers. If a protein is stable at a pH above pI (pH at which the net charge of the protein is zero), and thus is negatively charged, AE are used, and vice versa. High salt buffers are used to elute bound target molecules. **Hydrophobic interaction chromatography (HIC)** columns are functionalized with hydrophobic groups (e.g. phenyl, octyl) to separate proteins with differences in hydrophobicity. By applying high-ionic-strength buffer, hydrophobic interactions are additionally enhanced. This makes HIC a suitable subsequent purification step after high-salt elution during IEX or after high-salt precipitation. **Size exclusion chromatography (SEC)** separates molecules in a porous gel solely by their molecular size. The smaller a molecule the longer the retention time in the polymer, and the later the elution of the protein fraction. Due to the use of hydrophilic polymers, interactions with most proteins are minimized, which maximizes process yields. A major drawback is the low capacity of

SEC columns. In contrast, **affinity chromatography (AC)** offers high capacities and binding affinities, which allows for high elution concentrations and high purities, respectively. The method makes use of biological interactions, e.g. protein-ligand interactions (compare 3.1.1), which leads to highly selective separation. The most widely applied chromatographic method for the purification of antibodies still is protein A chromatography (Duhamel *et al.*, 1979). However, the major drawback is the high resin costs, which is one reason for the high cost ratio on the DSP side in the pharmaceutical industry. **Immobilized metal affinity chromatography (IMAC)** is a variant that takes advantage of the interaction of amino acid clusters with specific metals (e.g. Ni²⁺). A widely used tool for recombinant proteins is the fusion of a polyhistidine tag to one of the protein's termini. For elution, substances are usually used that compete with the tag of the target molecule and weaken the existing interactions (e.g. imidazole for IMAC). Very high purities can be achieved by connecting several chromatography methods in series. However, an economic balance needs to be found between the issues that the throughput is limited by above-mentioned inherent diffusion limitations and that chromatographic resins are expensive and short-life consumables (Przybycien *et al.*, 2004; Dos Santos *et al.*, 2016).

Aqueous two-phase extraction (ATPE) is a low-cost alternative to preparative chromatography for relatively mild protein capture and purification. An ATPE system is usually formed by mixing a polymer (e.g. PEG) with a kosmotropic salt (e.g. phosphate) or a second polymer (e.g. dextran). The partitioning between both aqueous phases depends on the surface properties of the proteins and the applied phases and so it is complex to predict. Asenjo and Andrews reviewed trends that could be derived from previous studies (Asenjo & Andrews, 2011). Recent studies have shown successful continuous processing, and thus an extended future use in industrial plants can be expected (Ferreira-Faria *et al.*, 2020). However, ATPE has decisive disadvantages due to the need for re-extraction and the high disposal costs, as the phases can hardly be recycled.

Protein precipitation is a further low-cost downstream method, which can achieve high yields with relatively simple process equipment (Hammerschmidt *et al.*, 2015 and 2016). In many recent studies, antibodies were successfully captured from impure solutions, that is, cell culture supernatant, making it to a relevant alternative to preparative chromatography in distinct cases (Hammerschmidt *et al.*, 2015; Burgstaller *et al.*, 2019). A large variety of precipitation compounds have been validated, ranging from salts, organic solvents, or long-chain polymers, such as PEG of varying molecular sizes (Sommer *et al.*, 2015). Similar to the process of crystallization, these compounds disrupt the hydration shell of proteins, which leads to less solvent-protein but more protein-protein interactions (salting out effect) (Englard & Seifert, 1990).

3.1.4 *Lactobacillus brevis* Alcohol Dehydrogenase (*LbADH*)

The investigated exemplary protein of this work is *Lactobacillus brevis* alcohol dehydrogenase (*LbADH*), which was discovered in the 1990s (Riebel 1997; Hummel *et al.*, 1997). It is a homotetrameric enzyme with a size of 106.4 kDa (26.6 kDa per monomer) that belongs to the short chain dehydrogenases (Enzyme class EC 1.1.1.2). Two bivalent magnesium ions (Mg^{2+}) coordinate the tetrameric assembly of the four monomers at the C-termini (see **Figure 3.5**). *LbADH* catalyzes the enantioselective conversion of a broad substrate spectrum, e.g. the reduction of prochiral ketones to the corresponding secondary alcohols to high enantiomeric excess of >99% in most cases and requires the cofactor NADPH. The first substrate residue typically is a methyl group, the second can be a bulky group, such as phenyl group (Leuchs & Greiner, 2011). One example is acetophenone, which is one of the preferred substrates (see **Figure 3.6**).

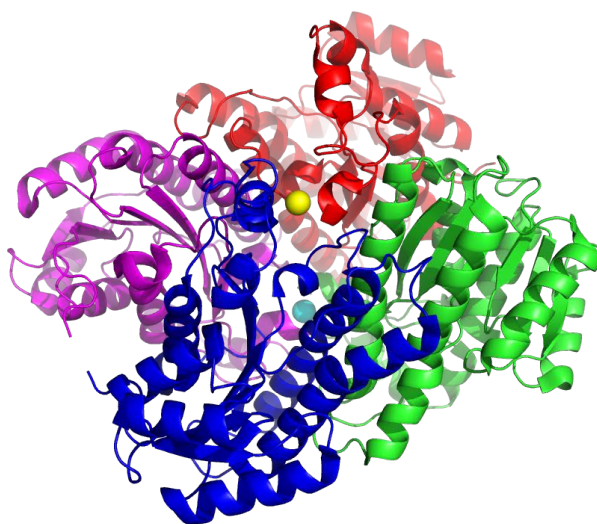


Figure 3.5: Three-dimensional structure of the *LbADH* homotetramer in cartoon view. The four monomers are illustrated in four different colors. The red and the blue colored monomers bind a Mg^{2+} -ion (yellow sphere) with the C-terminal glutamine residues at the top. The magenta and green colored monomers are rotated by 180° facing the C-termini and the respective Mg^{2+} (cyan sphere) downwards. (The figure was generated with PDB ID 6H07 using PyMOL, v.2.1, Schrödinger).

Several studies with *LbADH* have demonstrated feasible cofactor regeneration, e.g. enzyme-coupled using the glucose dehydrogenase (GDH) and substrate β -D-glucose (Kohlmann, 2011), or substrate-coupled using 2-propanol (Wolberg, 2001). *LbADH* is stable and enzymatically active at elevated temperatures with an activity optimum of $55^\circ C$ (Riebel, 1997). Further studies investigated the use of *LbADH* in whole-cell biotransformations (Ernst *et al.*, 2005; Bräutigam *et al.*, 2007; Bräutigam *et al.*, 2009; Dennewald *et al.*, 2011).

Biocatalytic activities have been observed even at high concentrations of organic compounds and in supercritical fluids. The combination of these biocatalytic properties have made *LbADH* a valuable biocatalyst in industrial applications, for example for the ethyl-3*R*-hydroxy-butanoate production in ton scale (Leuchs & Greiner, 2011).

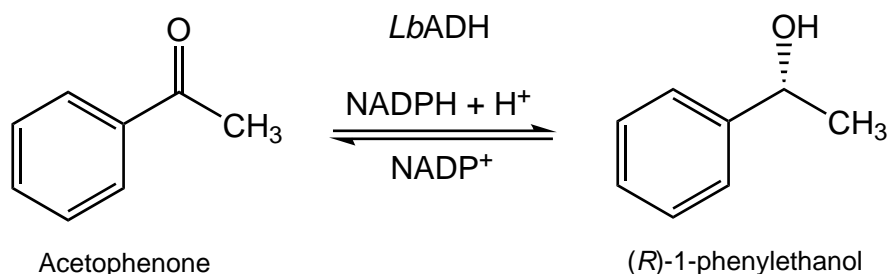


Figure 3.6: Reversible reaction from acetophenone to (*R*)-1-phenylethanol catalyzed by *LbADH* and cofactor NADP(H). (The figure was created using ChemDraw v19.0).

3.2 Protein Crystallization

When a protein crystallizes, it arranges itself in a highly ordered lattice, which can lead to sharp-edged crystal morphologies (see **Figure 3.7**). This is particularly remarkable when considering the structural flexibility and the large size of proteins compared to small molecules. The phenomenon of protein crystallization is rare in nature. During evolution, proteins have been designed in such a way that they do not crystallize because in crystallized form they can impair the viability of cells (Doye *et al.*, 2004). Thus, also in humans, mutations leading to protein crystallization can cause diseases such as eye cataracts (Siezen *et al.*, 1985). Nevertheless, humanity has been able to derive crucial benefits from protein crystallization for protein research and protein manufacturing. The fundamentals, methods and applications are explained in this chapter.

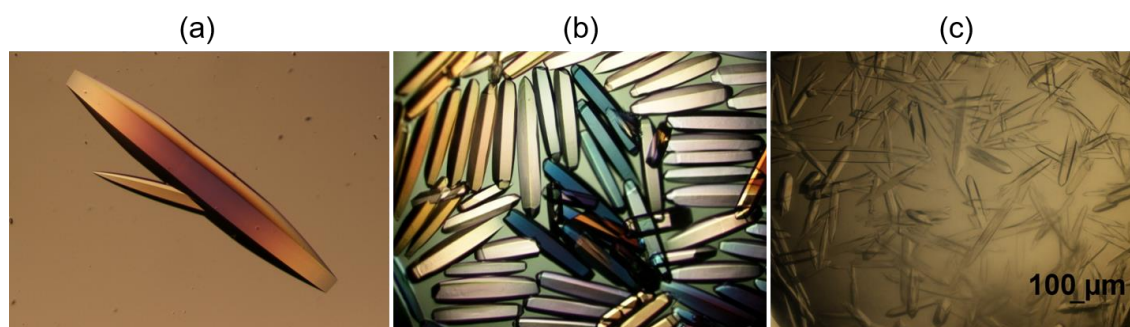


Figure 3.7: Crystals of different proteins. (a) *Thermomyces lanuginosus* lipase, (b) *Bacillus thermoproteolyticus* thermolysin, (c) Whole-length monoclonal antibody (mAb01). (Exemplary microphotographs from own crystallization experiments.)

3.2.1 Fundamentals

History

The history of protein crystallization dates back to 1840, when Hünefeld crystallized hemoglobin by slowly evaporating water from the blood of an earthworm (Hünefeld, 1840). The initial reasons for experimental protein crystallization were the purification of proteins and the validation of their purity. Franz Hofmeister made important discoveries, such as the role of salts in the precipitation and crystallization of ovalbumin (Hofmeister, 1888 and 1890). A further milestone in the history of protein crystallization was the crystallization of insulin in the 1920s (Abel *et al.*, 1926), followed by crystallization of the enzymes urease (Sumner, 1926), pepsin (Northrop, 1930), and lysozyme (Alderton and Fevold, 1946). James Batcheller Sumner, John Howard Northrop, and Wendell Meredith Stanley were finally awarded the Nobel Prize for their approaches in the field of protein crystallization in 1946. Starting with the advent of the first published three-dimensional structure of myoglobin (Kendrew *et al.*, 1958), protein crystallization came increasingly into focus from the 1960s onwards. Crystallography was further fueled in the following decades by major advances in genetics and recombinant protein production (reviewed by Chayen & Saridakis, 2008, and Krauss *et al.*, 2013). Today, protein crystallization still is applied for crystallographic purposes and technical crystallization for the purposes of purification and formulation of proteins.

Supersaturation, Nucleation and Crystal Growth

To crystallize proteins, they must be in a supersaturated state. This state does not correspond to the equilibrium state and it is above the solubility limit. Nevertheless, under certain physical and chemical conditions, this abundant protein can remain in solution for a certain period. The phase diagram illustrates the different states of protein crystallization at varying concentrations of protein and crystallization agent (see **Figure 3.8**). It is divided into an under-saturated region and an oversaturated region. In the undersaturated region, the protein is stable in solution. The supersaturated region can in turn be divided into three zones: At the highest concentrations of protein and crystallization agent the highest supersaturation is reached, which can lead to amorphous protein precipitation (precipitation zone). Significantly smaller is the area where nuclei are formed, and crystal growth takes place (nucleation zone). If the proteins are in the metastable zone, crystal growth can continue, but the degree of supersaturation is not sufficient for further nucleation. Supersaturation of proteins can be achieved by several crystallization methods.

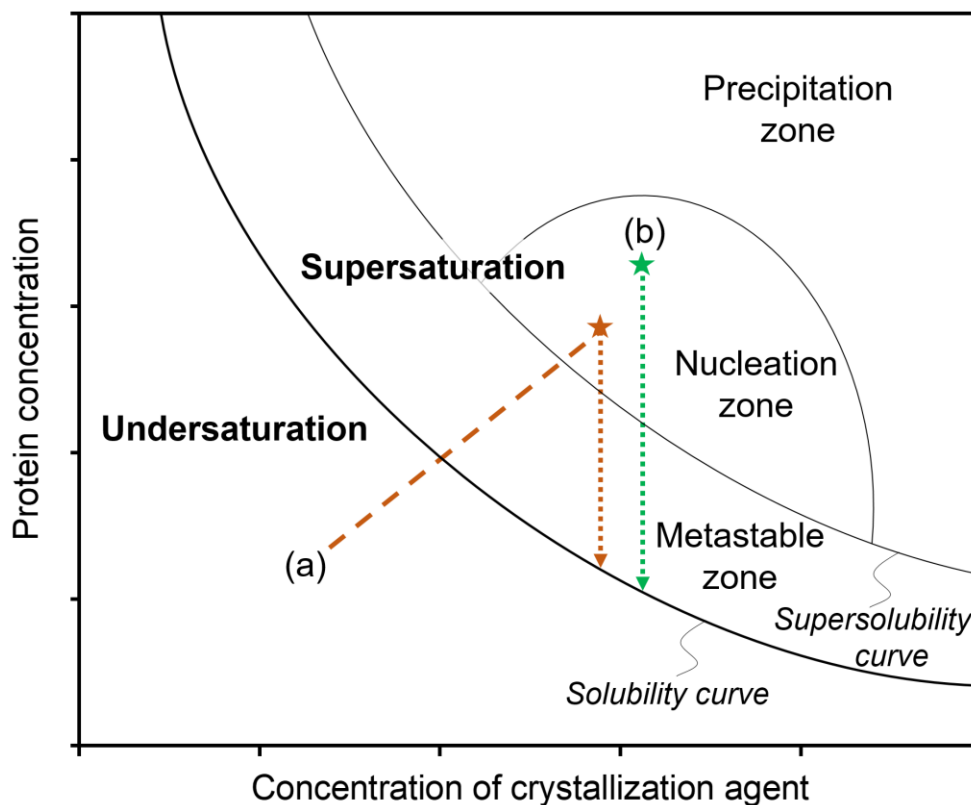


Figure 3.8: Protein crystallization phase diagram illustrated on the basis of varied concentration of crystallization agent and target protein. (a) The vapor diffusion crystallization is starting in the undersaturated zone and shifting towards the nucleation zone by vapor diffusion (dashed line). After nucleation ('star' symbol) crystal growth is continuing until reaching the solubility curve. (b) The batch crystallization process already starts in the nucleation zone (figure modified after Chayen, 1998).

On a molecular level, the formation of a crystal can be divided into two successive and fundamentally different steps: nucleation and crystal growth. Nucleation is a discontinuous phase transition from an entirely liquid phase (solution of completely dissolved protein) to an initial solid crystalline state (protein nucleus). The second step, crystal growth, is a continuous phase transition from liquid to solid.

The process of **nucleation** is difficult to control experimentally and even more difficult to describe theoretically. Recent reviews on protein nucleation conclude that also for nucleation, a two-step mechanism exists, in which a crystalline nucleus forms inside a metastable cluster of dense liquid (Vekilov, 2010). Igarashi *et al.* proposed a nucleation model based on differential scanning calorimetry (DSC) measurements for lysozyme in which a labile 'three-dimensional network' is formed with a size of 6.5 nm by electrostatic interactions. These formations in turn are assumed to build 'second ordered aggregates' by hydrophobic interactions, which then is assumed being the starting point for stable crystal growth (Igarashi *et al.*, 1999). Heigl *et al.* supported these assumptions, doing similar thermolysin crystallization experiments, but analyzed it by light scattering techniques such

as dynamic and static light scattering (DLS/SLS) and small-angle X-ray scattering (SAXS). They propose the formation of firstly dimers, followed by rodlike oligomers and ‘fractal clusters’. As soon as first crystals are visible, the concentration of the latter is reduced (Heigl *et al.*, 2018). Ooshima and co-workers propose a similar two-step nucleation for thermolysin (Ooshima *et al.*, 1997). Based on DSC studies, they found that three different groups exist, namely monomers, which aggregate to oligomers in the first nucleation step, and crystals, which arise from the aggregation of these oligomers. All three groups were clearly distinguishable by their thermal stability. Coherent with these results is a study from Sauter *et al.*, 2015, who applied real-time SAXS to investigate nucleation and crystallization behavior of bovine β -lactoglobulin. The authors also suggest a two-step nucleation mechanism, starting with protein intermediate aggregates and continuing with nucleation within these aggregations after a certain induction time. Unrestrained crystal growth only develops when the small crystals exceed the size of the intermediates, in which growth is assumed to be impeded by slowed diffusion.

All these examples mentioned describe *primary, homogeneous nucleation*, which is nucleation of a pure solution without the influence of foreign particles. This form of nucleation can only occur in the labile supersaturated (nucleation) zone. Besides, nuclei can also be formed in the presence of foreign particles, which can catalyze the nucleation process even in the metastable zone (*primary, heterogeneous nucleation*). The term *secondary nucleation* is used when crystallization is triggered by the presence of other crystals (or crystal abrasion), introduced into the crystallization system (Botsaris, 1976). However, this form is not a real nucleation form in the actual sense. Rather, it is the recruitment of molecules into existing newly introduced crystal structures, and in other words, crystal growth. Both, in crystallography and technical crystallization, it is a common strategy to grow crystals at reduced supersaturation.

The process of crystal growth occurs also at lower degrees of supersaturation, that is, in the metastable zone, until the solubility curve is reached. Compared to nucleation it is much better analytically accessible and better understood. McPherson describes two processes that must occur for crystal growth: Crystal face growth and tangential growth (McPherson *et al.*, 2000). The latter is the energetically favored one, as it describes the integration of molecules on an already existing level. Consequently, there are always at least two contact surfaces: the one with the layer below and at least one contact with the neighboring molecule that is already present on the same layer. Crystal face growth is the initiation of a new layer, building islands of molecules on top of the already existing layer. Since only one contact exists during this initiation step, crystal phase growth is the slower, rate-limiting step during crystal growth.

Protein crystallization is described as poorly reproducible since even small variations in crystallization conditions can significantly influence nucleation and crystal growth (Chernov, 2003; Newman *et al.*, 2007; Chen *et al.*, 2015). Not only the concentration of protein and crystallization agent, but also by a high number of biochemical, physical, and chemical variables have an impact on crystallization (McPherson, 2009). A selection is given in **Table 3.1**.

Table 3.1: List of biochemical, physical and chemical variables influencing protein crystallization. (Adapted from McPherson, 2009.)

Biochemical	Physical	Chemical
Purity	Temperature/ temperature variation	pH
Aggregation state of the protein	Time	Precipitant type and concentration
PTMs	Vibrations/ sound/ mechanical perturbations	Ionic strength
Source of the protein	Electrostatic/magnetic fields	Specific ions
Proteolysis/hydrolysis	Dielectric properties of the medium	Degree of supersaturation
Genetic modifications	Viscosity of the medium	Protein concentration
Inherent symmetry of the macromolecule	Rate of equilibration	Metal ions
Protein stability	Homogeneous or heterogeneous nucleants	Detergents/ surfactants/ amphophiles

Thermodynamic Considerations

From a thermodynamics perspective, crystallization is driven by the change in Gibbs free energy (ΔG) which can be expressed in the following equation:

$$\Delta G = \Delta H - T(\Delta S_{protein} + \Delta S_{solvent})$$

with ΔH = change in enthalpy, T = temperature, $\Delta S_{protein}$ = entropy change of the protein, and $\Delta S_{solvent}$ = entropy change of the solvent.

For a process to take place from a thermodynamic point of view, ΔG must be negative so that crystallization can occur. $\Delta S_{protein}$ is always negative since the surface residues become ordered during crystallization, which initially might contradict the laws of thermodynamics. However, the unfavorable, negative term $\Delta S_{protein}$ is compensated by a positive term $\Delta S_{solvent}$, which is due to the release of bound water molecules during protein crystallization. Furthermore, occurring attractive electrostatic interaction during the crystallization process result in a negative ΔH term. For protein crystallization, ΔG ranges between -10 and -100 kJ mol^{-1} , which is much smaller compared to crystallization of salts (Vekilov, 2003).

The respective proportion of the terms depends on the protein and the crystallization conditions (e.g. temperature, ionic strength, salt concentration). Vekilov proposes the change in entropy being the major driving force for several proteins (Vekilov *et al.*, 2002; Vekilov 2003; and reviewed in Derewenda, 2007). From that, the group of Derewenda derived the Surface Entropy Reduction (*SER*) strategy for engineering improved crystallizability by lysine or glutamic acid to alanine exchanges to reduce the entropic effort $\Delta S_{\text{protein}}$ during protein crystallization (Longenecker *et al.*, 2001; Derewenda & Vekilov, 2006; Derewenda & Godzik, 2017).

Crystal Contacts

Unlike all biological contacts, such as oligomerization or binding contacts, crystal contacts are purely artificial contacts that can only be produced *in vitro* under non-physiological conditions. Compared to oligomerization contacts (see 3.1.1), crystal contacts are significantly smaller in size. Cieslik *et al.* concluded from a large study of crystal contact areas that nearly 50% are built up by up to four residues with an average buried solvent-accessible surface area of $<100 \text{ \AA}^2$ (Cieslik & Derewenda, 2009). In most cases, overlapping crystal contacts were observed, with more than two participating molecules. The participation of secondary structures in crystal contacts (74% secondary structures) is highly similar to the amount found in oligomer interfaces (77%) (Dasgupta *et al.*, 1997). The most frequent amino acids at oligomerization contacts are arginine, leucine, and all aromatic residues phenylalanine, tyrosine, and tryptophan. In contrast, much more charged amino acids are found at the crystal contact interfaces, namely, serine, the basic amino acids arginine and lysine, and the acidic acids aspartic and glutamic acid (Dasgupta *et al.*, 1997). Many attempts have been pursued to engineer crystal contacts. In most cases, the intention was to obtain crystals that are better suited for crystallographic purposes, that is, with larger volumes or better scattering behavior of X-rays for higher resolution data sets.

3.2.2 Crystallization Methods and Agents

Protein crystallization can occur when the dissolved protein is in a supersaturated state. In theory, many ways can lead to supersaturation, such as altering the temperature, adding salts (salting out), removing salts (salting in), altering pH towards the pI, or increasing the protein concentration (addition of protein or evaporation of solvent). In practice, the most applied methods in crystallography are vapor diffusion, batch crystallization and microfluidics.

In **vapor diffusion experiments**, a droplet of protein solution mixed with a low concentration of crystallization agent is placed either in a crystallization well (sitting drop) or it hangs from the top of the cover glass slide (hanging drop). Below is the so-called

reservoir, which has a much larger volume and usually has a hygroscopic effect that realizes supersaturation by the salting out effect. Over time, water molecules transfer from the protein droplet to the reservoir solution until supersaturation is reached in the protein droplet. Consequently, the droplet follows a path through constantly rising concentrations of protein and crystallization agent, and it is therefore not possible to specify the conditions where nucleation occurred. This path of a droplet through the crystallization phase diagram is illustrated in **Figure 3.8 (a)**. Vapor diffusion is the most applied crystallization method for the identification of crystals suitable for crystallography.

In **microbatch crystallization** (microscale batch crystallization), supersaturation is achieved directly when the crystallization buffer is added to the concentrated protein solution. This means, that the mixed sample is in the nucleation zone just from the experimental start (see **Figure 3.8 b**). In some cases, paraffin oil on top of the droplet prevents evaporation. Alternatively, wells are sealed with adhesive foil. This allows for constant conditions within a longer time frame of several weeks. Contrary to vapor diffusion, the crystallization result can be attributed to concrete conditions, which is why this method is more suitable for the characterization of the crystallization behavior. Crystallization phase diagrams, for instance, are generated by a large number of microbatch experiments.

Microfluidics is a third method, which will probably play a greater role in the future. The reason for this is the minimal amount of sample volumes required and the possibility of automated high-throughput crystallization screening. Moreover, it can be applied for a variety of experiments, ranging from the generation of phase diagrams to the precise study of crystallization kinetics (Sommer & Larsen, 2005; Abdallah *et al.*, 2016). Similar to batch crystallization, the conditions can be adjusted, and crystallization success can be accurately traced back to these. Microfluidics has not only developed to a powerful characterization and screening tool but has also high potential towards industrial applications, termed ‘lab-on-a-chip’ technology. It was shown that enzymes can be crystallized and cross-linked in microchannels prior to its application in continuously working microfluidic biosensing (Conejero-Muriel *et al.*, 2016).

A huge variety of **crystallization agents** exists. Since the underlying effects of crystallizing agents are only marginal known and since no predictions can be made regarding which reagent is most suitable for certain proteins, empirical screens still are the method of choice when it comes to *de novo* crystallization of proteins. Commercial screenings are available that generally cover different agents with different buffers that have led to crystallization success before for several proteins. McPherson categorizes all crystallization agents into four main groups: salts, organic solvents, low-molecular-weight

define the locations of all atoms. Larger unit cells result in larger number of reflections. Based on resulting electron densities, structural data can be extracted during the refinement process, such as positions of all atoms, bond lengths, or measure of fixation or disorder.

The most widely used technique **X-ray crystallography** uses the effect of X-ray scattering by the electrons of the target protein. Therefore, hydrogen atoms can only be determined at resolutions below 1.0 Å, since they scatter X-rays only weakly (based on data from the Protein Data Bank (PDB), only 0.5% of all protein X-ray datasets have a resolution <1.0 Å). An alternative, but still rare method, is **neutron crystallography**. It is the dominant method for accurate determination of hydrogen atoms, which allows for a more detailed understanding of reaction mechanisms (e.g. protonation states) or networks of hydrogen bonding. The underlying basic physical difference is that neutrons are scattered by protons. The major disadvantage is the requirement of very large crystals with a size of >0.5 mm³ since neutrons interact less with matter than X-rays (Blakeley *et al.*, 2008). Furthermore, protein crystals need to be deuterated to improve the detection of hydrogens, to be more precise, deuterium (Shu *et al.*, 2000). The application opportunities are therefore currently limited due to the high crystal requirements and the high experimental effort, which is reflected in the low number of neutron structures published annually.

Crystallographic Terms Used in This Work

- i. **Asymmetric unit:** The smallest fragment from which the unit cell can be constructed by symmetry operations.
- ii. **Unit cell:** The smallest structure that allows to build up the entire crystal lattice by translation in all crystal directions (vectors) a, b, c.
- iii. **Space group:** Description of the symmetry of crystal structures. They are the combination of structural symmetry elements with the 14 translation lattices (*Bravais* lattices). Taking reflections and rotational reflections into account, the total number of crystallographic space groups is 230 (Kleber *et al.*, 2010). Depending on the crystallization conditions, some proteins crystallize in different space groups, leading to a different crystal packing of proteins in the crystal lattice (Gillespie *et al.*, 2014; Driessche *et al.*, 2018).
- iv. **Diffraction quality:** The ability of a protein crystal to give sharp diffraction patterns with clear reflections at large angles from the X-ray or neutron beam. The crystal appearance can be deceiving, but in most cases, crystals are used for the measurement which are as large as possible and exhibit sharp edges.

- v. **Resolution:** A measure for the degree of diffraction quality and the level of detail that can be seen in the density map. The given resolution represents the smallest distance that could be resolved in the diffraction pattern.
- vi. **Electron density:** A representation of the probability of finding an electron (in X-ray crystallography) at a certain location around an atom. The higher the electron density at a certain point, the higher the probability of the electrons being located there (and the better the resolution of this area).

3.2.4 Protein Crystal Engineering

Like engineering catalytic properties or thermal stabilities of proteins discussed earlier, proteins can be engineered towards improved crystallization behavior or enhanced crystal-properties. In the following, strategies are presented for the so far most common purposes of protein crystal engineering.

Engineering for Crystallographic Purpose

Crystallization of proteins is a prerequisite for structural determination via X-ray or neutron diffraction. However, it is suggested that only 30% of proteins, which are expressed in soluble form with *E. coli*, are crystallizable, and even a smaller part is suitable for crystallographic purposes (Dale *et al.*, 2003). If crystallization is not feasible, the protein of interest can be mutated to engineer the crystallizability. Since proteins have evolved not to crystallize due to negative effects on the viability of the cell, Doye and co-workers claimed that mutating a protein's surface would lead to a more crystallizable protein (Doye *et al.*, 2004). In fact, the first successful study was already published almost 30 years ago by Lawson *et al.*, who transferred a crystal contact from a crystallizable orthologue to non-crystallizable human ferritin H chain (Lawson *et al.*, 1991). Just by the exchange of a single amino acid, a Ca²⁺-binding bridge and consequently a crystal contact was created. Doye's theory was further supported by several studies of the group of Zygmunt Derewenda. The authors propose a generalized solution for the bottleneck crystallization in structure determination by X-ray diffraction. The respective above-mentioned semi-rational *SER* approach follows the site-directed exchange of large hydrophilic amino acids such as glutamic acid and lysine with the small and hydrophobic amino acid alanine. The consequently local reduction of conformational entropy leads, according to the author, to improved crystallization by 'low-entropy' or 'sticky' surface patches (Derewenda, 2004a,b; Derewenda and Vekilov, 2006; Cooper *et al.*, 2007; Goldschmidt *et al.*, 2007; Derewenda 2007; Cieslik and Derewenda, 2009; Derewenda and Godzik, 2017). In the studies of the Derewenda group, the term 'improved crystallization' is defined by the fact that proteins crystallize, which had been refused before, and that the diffraction quality of engineered

crystals is improved, resulting in high resolution X-ray datasets. In the case of the Rho-specific guanine nucleotide dissociation inhibitor (RhoGDI), it was shown that crystallization was promoted by mutating surface-oriented lysine to alanine (Longenecker *et al.* 2001). In comparable crystallization studies, the substitution of alanine or aspartic acid for glutamic acid (Mateja *et al.*, 2002) and arginine for lysine (Czepas *et al.*, 2004) led to improved crystallizability. Dasgupta *et al.* also suggested the mutation of lysine residues as a rational strategy for enhancing crystallizability (Dasgupta *et al.*, 1997). A further successful approach of improving crystallizability by surface mutations was published by Shimamura *et al.*, 2009. Here, the intention also was to improve the diffraction quality for structure determination by creation of an untwinned crystal (the WT crystals exhibit a strong twinning tendency). A double mutated β -lactamase was recombinantly produced, purified by one-step AEX chromatography and crystallized in the desired way. McElroy and co-workers improved the crystallizability of thymidylate synthase by mutational surface engineering of single amino acids (McElroy *et al.*, 1992). They additionally emphasized that the surface mutants each do crystallize under different conditions and in different space groups than the WT protein. A first review on protein engineering as a tool for crystallography was published by Price and Nagai (Price and Nagai, 1995).

However, these engineering results must be considered from a crystallographer's point of view, meaning that reproducible results are less important than the final recorded high-resolution X-ray dataset. In the presented studies, only little information is given about the effort to provide identical crystallization conditions (e.g. identical protein purity and concentration) for all tested mutants.

Although some authors point out that entropic effects have a larger impact on protein crystallization than enthalpic effects (Vekilov *et al.*, 2002; Vekilov, 2003), other crystallization studies let assume that the latter can also improve protein crystallization. D'Arcy *et al.*, for example, successfully generated better crystallizable mutants (evaluated by the number of 'hits') when hydrophobic residues were exchanged with more hydrophilic ones (D'Arcy *et al.*, 1999). Driessche *et al.* describe the strength of crystal contact interactions by the number of hydrogen bonds (Driessche *et al.*, 2018). By impairing these (generating 'knockouts'), the crystals were forced to crystallize in a different crystal lattice.

Engineering for Material Science Purpose

Mostly, protein crystals have been considered as a highly ordered molecule arrangements that allow for an X-ray diffraction pattern, and thus to elucidate its three-dimensional structure. From a material science prospective, the application of protein crystals can also have distinct technical advantages over protein solutions, nicely reviewed in detail by Hartje & Snow (2018). Protein crystals reveal a higher shelf-life (Shenoy *et al.*, 2001) and

higher thermal stability compared to dissolved protein (Basu *et al.*, 2004). The content of solvent in protein crystals in the range of 27–65% with pores ranging in size from 0.3 to 10 nm (Matthews, 1968; Vilenchik *et al.*, 1998). Due to the high solvent content in the crystal, proteins remain their native structure, and thus maintain their functionality, e.g. ligand binding or biocatalytic characteristics (McPherson & Gavira, 2014). Due to the porous structure, ligands, inhibitors, substrates, or cofactors can freely diffuse into the crystal lattice. An enzyme can therefore be easily immobilized in crystallized and enzymatically active form and applied in biocatalysis or in biosensors ('lab on a chip'; St. Clair & Navia, 1992; Luiz de Mattos *et al.*, 2001; Conejero-Muriel *et al.*, 2016). Lalonde *et al.* even reported a positive effect of cross-linked *Candida rugose* lipase crystals on enantioselectivity compared to the use of crude cell extract (Lalonde *et al.*, 1995).

One reason why the technical applicability of protein crystals is limited is their relatively low mechanical and thermal stability. This is due to the high solvent content and the relatively small size of crystal contact patches, which are connected by non-covalent interactions (Pifat-Mrzljak, 2007). One solution to this problem has been the crosslinking of enzyme crystals (cross-linked enzyme crystals, CLECs) by generating covalent bonds (Margolin & Navia, 2001). Several studies have approved the applicability of this approach, even under harsh conditions (St. Clair & Navia, 1992; Noritomi *et al.*, 1998). Suitable ionizable amino acid residues are aspartic and glutamic acid, lysine, and arginine, which can be cross-linked by various compounds, e.g. by aldehydes (linking amines) or by carbodiimides ('zero-length crosslinkers' linking amines with carboxyl groups) (Hermanson, 2013; Hartje *et al.*, 2018). Yang *et al.* demonstrated that engineered T4 lysozyme with introduced cysteines also formed disulfide bonds in the absence of chemical cross-linking agent, which allowed for a more biocompatible approach (Yang *et al.*, 2003). Alternative engineering approaches to improve the crystal stabilities promoted the artificial oligomerization of proteins as precursor for successful crystal nucleation and growth. This was either realized by introducing cysteines for disulfide linkages (Banatao *et al.*, 2006) or by introducing histidines for novel metal binding sites, which were coordinated by copper (Cu^{2+}), nickel (Ni^{2+}) or zinc (Zn^{2+}) (Laganowsky *et al.*, 2011).

3.2.5 Technical Protein Crystallization

Crystallography still is the most popular application of protein crystallization. As mentioned before, protein crystallization was used much earlier, almost 200 years ago, for the purification of proteins (Hünefeld, 1840). At that time, highly technological methods, such as chromatography did not yet exist, which meant there was no alternative to this basic protein purification method. Today, there are highly developed chromatographic

purification systems that use complex surface functionalization of polymer particles to separate proteins mixtures. Noticeably, it is the chromatographic methods that have recently been declared the bottleneck of biotechnological processes (Dos Santos *et al.*, 2016). In addition to the alternatives described above such as extraction or precipitation, it is protein crystallization that has been reemerged since the beginning of the 21st century. In the following, recent developments and applications of technical crystallization are discussed for the purpose of protein purification in DSP and for protein formulation. In this work, the term ‘technical crystallization’ is defined as an integrated DSP method to crystallize large quantities of recombinant protein for purification or formulation purposes in a reproducible manner. It is a synonym for industrial-scale, large-scale, or preparative protein crystallization (as referred to in several recent studies, which are discussed in the following).

Purification

The theoretical principles of protein crystallization, which are also valid for a larger scale, were discussed above (see 3.2.1). Technical crystallization for the purification of proteins is comparable to precipitation regarding the relatively simple process requirements, low costs, and high yields. Due to the nature of a protein crystal – being the densest possible formation of molecules – protein crystals enclose less impurities than amorphous precipitate. The crystallization process itself is also much more selective than precipitation since co-crystallization (e.g. of host cell protein (HCP)) does not occur due to the considerably smaller nucleation zone compared to the precipitation zone of proteins. In comparison to preparative chromatography (discussed in 3.1.3) crystallization lacks mass transfer limitations, and it requires no costly equipment, consumables and large buffer volumes.

While crystallography requires large, single, and well-diffracting crystals, technical crystallization requires a completely different crystallization behavior. First, the process of crystallization becomes important. Crystallization is desired to be fast, reproducible, and must lead to high yields (low residual equilibrium protein concentration). Second, a homogeneous and reproducible and narrow size distribution of crystals is important, and third, the further processing (e.g. crystal dissolution, recrystallization) must be realizable without affecting the functionality of the proteins (e.g. enzymatic activity).

These advantages and requirements have been recognized by several research groups, which developed new strategies for a successful application of crystallization in biotechnological DSP. Developments of the last two decades were comprehensively reviewed by Hekmat (2015b). Selected successful examples of protein purification by technical crystallizations are *L*-methionine γ -lyase (stirred 100-L-crystallizer; Takakura *et al.*, 2006), fungal lipase (stirred 225-mL-crystallizer; Jacobsen *et al.*, 1998), *Candida rugosa* lipase and yeast alcohol dehydrogenase (ADH I) (both in mixed 500-mL Duran bottles; Lee

et al., 2000), eGFP (stirred 5-mL-crystallizer; Hekmat *et al.*, 2015a). Crystallization was conducted in presence of impurities, such as HCP in crude cell lysate or manually spiked protein. Even in presence of up to 57% HCP crystallization yields of 87% were reported (Takakura *et al.*, 2006). Seeded stirred-batch crystallization experiments were reported for ovalbumin (stirred 1-L-crystallizer, seeded; Judge *et al.*, 1995) and lysozyme (stirred 15-mL-vials; Carbone & Etzel, 2006).

In the initial phase of technical crystallization as an emerging purification method, Schmidt *et al.* pointed out bottlenecks, such as crystallization from impure solutions and scale-up (Schmidt *et al.*, 2005). Regarding crystallization success from impure solutions, examples were published sporadically, but the results seemed to depend mainly on the intrinsic crystallization ability of the target protein and on the buffer composition. Referring to Schmidt's second suggestion for improvement, a process-related parameter was proposed for the scale-up from the mL- to the L-scale, exemplary by crystallization of a Fab-fragment of the therapeutic antibody Canakinumab and well-known lysozyme. The optimal scale-up parameter was the maximum local energy dissipation ϵ_{max} , which had only been assigned for small molecules before (Smejkal *et al.*, 2013a). ϵ_{max} was estimated by the equation from Henzler, 2000:

$$\frac{\epsilon_{max}}{\bar{\epsilon}} \approx \frac{a}{\left(\frac{d}{D}\right)^2 \times \left(\frac{h}{d}\right)^{\frac{2}{3}} \times z^{0.6} \times (\sin\alpha)^{1.15} \times z_1^{\frac{2}{3}} \times \left(\frac{H}{D}\right)^{-\frac{2}{3}}}$$

with $a = 4$ for baffled vessels, 16 for unbaffled vessels; h = height of the impeller blade (m); d = impeller diameter (m); z = number of impeller blades; α = blade inclination to the horizontal (degree); H = and tank filling height (m); D = tank inner diameter (m).

$\bar{\epsilon}$ is calculated by equation:

$$\bar{\epsilon} = \frac{P}{V \times \rho} = \frac{2\pi \times n \times M}{V \times \rho}$$

with P = power (W); V = crystallization volume (L); ρ = density of the liquid (kg m^{-3}); M = torque (Nm); and n = set stirrer speed, rpm (s^{-1}). M is measured at the crystallizer's agitator shaft at a set stirrer speed and corrected by subtracting the measured torque needed for stirring the empty tank.

The scale-up approach was subsequently confirmed by the purification of a therapeutic monoclonal IgG1 antibody via protein crystallization from clarified cell harvest in the stirred mL- and L-scale (Smejkal *et al.*, 2013b). In this study, high crystallization yields of

88–90% and high purities of 98.5% were achieved after a recrystallization step, demonstrating outstanding results towards chromatography-free capture and purification of a therapeutic protein. Recently, the first continuous crystallization of a monoclonal whole-length antibody from concentrated and dialyzed cell harvest was reported (Hekmat *et al.*, 2017).

Due to entirely different experimental set-ups (e.g. different reactor geometries, temperatures, protein/HCP concentration) and proteins used, no direct comparison should be made among the listed crystallization approaches. However, average yields in the range of 85 to >95% and purities >90% in presence of impurities clearly demonstrate the general high capture and purification potential of technical protein crystallization.

Formulation

Crystalline proteins can be additionally considered as a highly beneficial formulation form. Since crystals are the most concentrated form of a protein, crystalline drug formulations enable high-dose delivery with viscosities significantly lower than those of equally concentrated solutions (Yang *et al.*, 2003). This advantage of crystalline formulations is particularly noticeable in therapeutic applications in patients whose visits to the doctor would be significantly shortened and less uncomfortable with subcutaneous administration of a crystalline biotherapeutics compared to slow conventional infusions. Moreover, protein crystals reveal a high shelf-life and higher thermal stability compared to dissolved and precipitated proteins (Shenoy *et al.*, 2001; Basu *et al.*, 2004). The minimal volume and high storage stability, even under unrefrigerated conditions, results in lower transport and storage costs. For therapeutic drug delivery, crystalline formulations provide a controlled dissolution, as it has been beneficial for recombinant insulin (Merkle & Jen, 2002).

With regard to industrial formulations of proteins by crystallization, the latter one is the most prominent example. The DSP of insulin includes a 12 h crystallization step in a stirred 500-L-crystallizer at 5 °C in the final polishing and formulation section with a crystallization yield of 90%. Subsequently, the crystal slurry is recovered by centrifugation and finally freeze-dried (Harrison, 2015). Applying a similar crystallization set-up as Smejkal *et al.* (2013 a,b), but using pre-purified *Gallus gallus* lysozyme and *Thermomyces lanuginosus* lipase, Hebel *et al.* also successfully scaled-up to geometrically similar stirred crystallizers from microbatch up to the L-scale (Hebel *et al.*, 2013a). Furthermore, a similar scale-up approach of the antigen-binding fragment FabC225 was studied, resulting in yields of 99% after only 2 h (Hebel *et al.*, 2013b). Since crystallization agents, such as salts are likely to be imbedded in the solvent accessible crystal channels, formulation processes must aim for a removal of these eventually unwanted compounds. Hebel *et al.* demonstrated, that washing of the FabC225 crystal slurry led to a decrease in ammonium sulfate by 92% with a marginal

loss of the target protein of 2%. In a similar study, lysozyme, eGFP, and a lipase with spiked or residual HCP content of up to 16% HCP was crystallized in stirred 5-mL-crystallizers. The final yield of the respective target proteins after crystal washing was 80–94% at high purity grades of $\geq 99\%$ (Hekmat 2015b).

4 Material and Methods

4.1 Material

All materials used in this work are listed in the appendices (see A).

4.2 Molecular Biological Methods

4.2.1 Site-Directed Mutagenesis

The *LbADH* gene was modified by site-directed mutagenesis applying the standard QuikChange polymerase chain reaction (PCR) protocol. Primers were designed with overlapping sequences at the 3'-termini according to the protocol of Zheng *et al.*, 2004. PCR components are listed in **Table 4.1**. A PCR thermocycler was programmed and run according to the protocol described in **Table 4.2**.

Table 4.1: Applied PCR program for site-directed mutagenesis.

Component	Volume, μL
sterile H ₂ O	30.5
5x Phusion buffer	10
10 μM forward primer	2.5
10 μM reverse primer	2.5
DMSO	2
DNA template (50 ng μL^{-1})	1
10 mM dNTPs	1
Phusion Polymerase	0.5

Table 4.2: Thermocycler protocol used for all QC-PCRs. T_m = calculated melting temperature of paired primers.

Program step	Temperature, $^{\circ}\text{C}$	Duration
Initial denaturation	98	3 min
20 cycles of:		
- Denaturation	98	10 sec
- Annealing	5 below T_m	30 sec
- Elongation	72	30 sec per 1000 bp
Final elongation	72	10 min
Storage	15	∞

4.2.2 DNA Separation by Agarose Gel Electrophoresis

DNA agarose gel electrophoresis was conducted to verify correct PCR product sizes after QC-PCR. Midori green stained agarose gels were loaded with prepared PCR samples (10 μ L PCR product + 2 μ L 6x Loading Dye [New England Biolabs, Ipswich, USA]). Gels were placed in an electrophoresis chamber and covered with TAE buffer. Electrophoresis was conducted at 120 V for 1 h. Fluorescent DNA bands were rendered visible using UV light.

4.2.3 DpnI Digestion

DpnI-digestion of PCR product was conducted to digest parental, non-mutated plasmid DNA. 40 μ L PCR product was added to 7 μ L 10x Cut Smart Buffer, 2 μ L DpnI (both from New England Biolabs, Ipswich, USA), and 21 μ L H₂O (total volume: 70 μ L) and incubated at 37 °C for at least 1 h mixing frequently. No buffer exchange was conducted prior to DpnI digestion. After DpnI digestion, the DNA was purified, and the buffer exchanged applying the *FastGene PCR Extraction Kit* (Nippon Genetics Europe, Germany).

4.2.4 Plasmid DNA Amplification, Extraction and Sequencing

Plasmid DNA was amplified with *E. coli* DH5 α . Chemically competent *E. coli* DH5 α cells were either transformed with intact plasmid DNA or with PCR product generated during QC-PCR mutagenesis (resulting in ‘nicked’ plasmid DNA) (*E. coli* transformation see 1.3.2). Transformed *E. coli* DH5 α cells were selected on solid LB agar containing kanamycin by transferring single colonies to 6 mL liquid LB agar containing kanamycin in preculture tubes. Cells were grown at 37 °C for 16 h under continuous shaking.

DNA plasmid extraction was conducted using the FastGene Plasmid Mini Kit (NIPPON Genetics Europe, Dürren, Germany) according to the manufacturer’s protocol. The concentration and purity of the isolated plasmid DNA was determined using a spectrophotometer (BioSpectrometer Basic, Eppendorf AG, Hamburg, Germany). Plasmid DNA sequencing was conducted by Eurofins Genomics (Ebersberg, Germany). Sequencing data was analyzed using GenomeCompiler (www.genomecompiler.com).

4.2.5 Molecular Subcloning

The intention was to generate genetic variants of the initial His₆-tagged *LbADH* ‘NHis’ that exhibit no or a shortened linker sequence between the N-terminus of the *LbADH* and the hexahistidine (His₆) sequence. Moreover, a redundant methionine at the N-terminus of the *LbADH* (originally coding for the transcription start) was intended to be eliminated. Additionally, three amino acids N-terminal of the His₆ tag, were intended to be substituted by a single glycine (owed to the NcoI restriction site which introduces the start codon ATG

followed by a GNN triplet). Amino acid sequences of all three variants are given in Appendix C.1).

Overhang PCR on the existing pET28a_*LbADH*_NHis plasmid introducing the His₆ sequence directly 5'-terminal of the *LbADH* gene (nL-variant; no linker) or upstream of a shortened but flexible Glycin-Serin-Glycin linker (sL-variant; short linker). At the respective 5'-terminus and at the 3'-terminus restriction sites are added to allow subcloning via enzymatic digestion and ligation. Forward primer *LbADH*_nL (5'-3'; lower case: 5'-overhang): ggtccatgggccaccaccaccaccacatTCTAACCGTTTGGATGGTAAGGTA. Forward primer *LbADH*_sL (5'-3'; lower case: 5'-overhang): ggtccatgggccaccaccaccaccaccacggatcaggaTCTAACCGTTTGGATGGTAAGGTA. Mutual reverse primer: (100% complementary to the original plasmid sequence; 3' HindIII restriction site; 5'-3'): AGTGCGCCGCAAGCTTTTATTG.

The PCR product and the original pET28a_*LbADH*_NHis plasmid were each digested with NcoI and HindIII according to the manufacturer's protocol (New England Biolabs, Ipswich, USA). Agarose gel electrophoresis and subsequent gel purification (FastGene Gel Extraction Kit, Nippon Genetics Europe, Germany) of the digested backbone were conducted. Ligation of inserts and backbone using T4 DNA Ligase were conducted according the manufacturer's protocol (New England Biolabs, Ipswich, USA). Subsequently, chemically competent *E. coli* DH5 α cells were transformed with ligation product. *E. coli* DH5 α colonies on LB agar plates containing kanamycin were amplified, the plasmid DNA was extracted and sequenced. The pET28a_*LbADH*_sL plasmid DNA sequence is given in Appendix C.2).

4.3 Bacterial Transformation and Protein Production

4.3.1 Production of Chemically Competent Bacterial Cells

This method was applied under sterile conditions for the *E. coli* strains BL21(DE3) and DH5 α . A glycerol stock of non-competent BL21(DE3) or DH5 α cells were spread on an LB agar plate (antibiotic-free) and incubated at 37 °C overnight. Single colonies were transferred to 250 mL shaking flasks containing 50 mL LB medium (preculture) and incubated at 37 °C and 250 rpm overnight. 200 mL TB medium (main culture) was inoculated with 4 mL of the preculture. The main culture was incubated at 37 °C and 250 rpm until OD₆₀₀ = 0.5 (optical density at 600 nm) was reached. The cell suspensions were divided into four 50 mL polypropylene tubes and allowed to cool on ice for 10 min. The cell suspensions were centrifuged at 4 °C and 3260 g for 10 min. The supernatant was discarded, and the cell pellets resuspended in 10 mL solution I (10 mM sodium acetate, 50 mM MnCl₂, 5 mM NaCl). All resuspended pellets were combined in one tube and again allowed to cool on ice for 10 min. Centrifugation was repeated and the resulting pellet was resuspended in 8 mL

solution II and allowed to cool on ice for 10 min. 100 μL of the cell suspension was aliquoted in 1.5 mL tubes, frozen in liquid nitrogen and stored at $-80\text{ }^{\circ}\text{C}$.

4.3.2 Heat Shock Transformation of Chemically Competent Cells

Aliquots of chemically competent *E. coli* strains BL21(DE3) or DH5 α were thawed on ice for 5 min. 5 μL of DpnI digested, purified PCR product or 1 μL of purified plasmid DNA (100 ng μL^{-1}) were pipetted into the cell suspension. Cells were incubated two minutes on ice, prior to a 45 sec heat shock in a $42\text{ }^{\circ}\text{C}$ water bath. Cells were transferred back on ice for another 5 min. 300 μL SOC medium was added to the cells which then were incubated at $37\text{ }^{\circ}\text{C}$ under continuous shaking for 1 h, allowing one bacterial generation cycle. 150 μL of the cell suspension was plated on LB agar containing kanamycin, prior to incubation at $37\text{ }^{\circ}\text{C}$ overnight.

4.3.3 Recombinant Protein Production with *E. coli*

Most recombinant protein production were conducted in shaking flasks on the mL-scale. Initially, *LbADH* WT was additionally produced in a 50-L-bioreactor for larger crystallization screenings for Neutron diffraction crystals and for providing protein to cooperation partners.

Shaking Flasks

- i. Preculture: Generated by transferring a single colony to polypropylene tubes containing 7 mL TB medium (+ Kanamycin). Incubation at $30\text{ }^{\circ}\text{C}$ and 200 rev min^{-1} (5 cm eccentricity of the shaking table) in a shaking incubator overnight.
- ii. Main culture: OD_{600} was determined and part of the preculture was transferred to a 500 mL shaking flask (main culture) containing 100 mL TB medium (+Kanamycin) aiming for a start OD_{600} of 0.05 in the main culture.
- iii. *LbADH* production: Induced by the addition of IPTG (final concentration 1 mM) at $\text{OD}_{600} = 0.7$ (approx. 4 h, begin of the exponential growth phase). Cell growth was monitored by OD_{600} measurements. The correlation factor dry biomass/ OD_{600} was determined to be 0.5.
- iv. Cell harvest: After 14 h induction time, cells were equally transferred to 2x 50 mL tubes and centrifuged at 1500 g and $4\text{ }^{\circ}\text{C}$ for 15 min. The cell pellets were resuspended in 25 mL chilled PBS (phosphate-buffered saline), pooled and centrifuged again.
- v. Storage: The cell pellet was stored at $-20\text{ }^{\circ}\text{C}$ for at least 2 h before further processing.

50-L Bioreactor

- i. Pre-preculture: 2x 100 mL LB medium and 100 μ L *E. coli* BL21(DE3) pET28a_LbADH_WT glycerol stock solution were incubated in 2x 500 mL shaking flasks at 37 °C and 200 rev min⁻¹ (5 cm eccentricity of the shaking table) for 14 h).
- ii. Pre-culture: 4x 400 mL LB medium and 8 mL pre-preculture (OD₆₀₀ = 4,5) were transferred in 4x 2000 mL shaking flasks and incubated at 37 °C and 200 rev min⁻¹ for 6 h.
- iii. 50-L fed-batch process (main culture, LP75; Bioengineering AG, Wald, Switzerland): Inoculation of 32 L glucose/mineral salt medium (Riesenberg, 1991), pH 6.8, with 1.6 L pre-culture (start OD₆₀₀ = 0.175). Duration of batch phase: 6.3 h.
Bioprocess parameters (t = 0): n_{stirrer} = 300 min⁻¹; T = 37 °C; p = 0.2 bar; pH = 6.8; air flow = 25 L min⁻¹, pO₂ >45 % (controlled by rpm, airflow, pressure cascade), $\mu_{\text{set}} = 0.12\text{--}0.15\text{ h}^{-1}$. Cell growth was monitored by OD₆₀₀ measurements and dry biomass determinations. Glucose concentration during batch and fed-batch phase was estimated via *Accu-Check* device (Roche Diagnostics, Mannheim, Germany).
- iv. LbADH production: Induced by the addition of IPTG (final concentration 1 mM) at OD₆₀₀ = 65 (approx. after 27 h). Bioprocess parameters: T = 30 °C; pH = 6.8; pO₂ >45% (controlled by rpm, airflow, pressure cascade), $\mu_{\text{set}} = 0.12\text{ h}^{-1}$.
- v. Cell harvest after 48 h at OD 110 (prior to stationary growth phase).
- vi. Cell concentration via disc separator CSA_08 (GEA, Westfalia, Oelde, Germany) (volume reduction from 50 to 15 L).
- vii. Storage: The cell suspension was stored at -20 °C before further processing.

The methodological planning and implementation was realized at TUM Research Center for Industrial Biotechnology in cooperation with Dr. Dominik Maslak (Bioreactor see **Figure 4.1**).

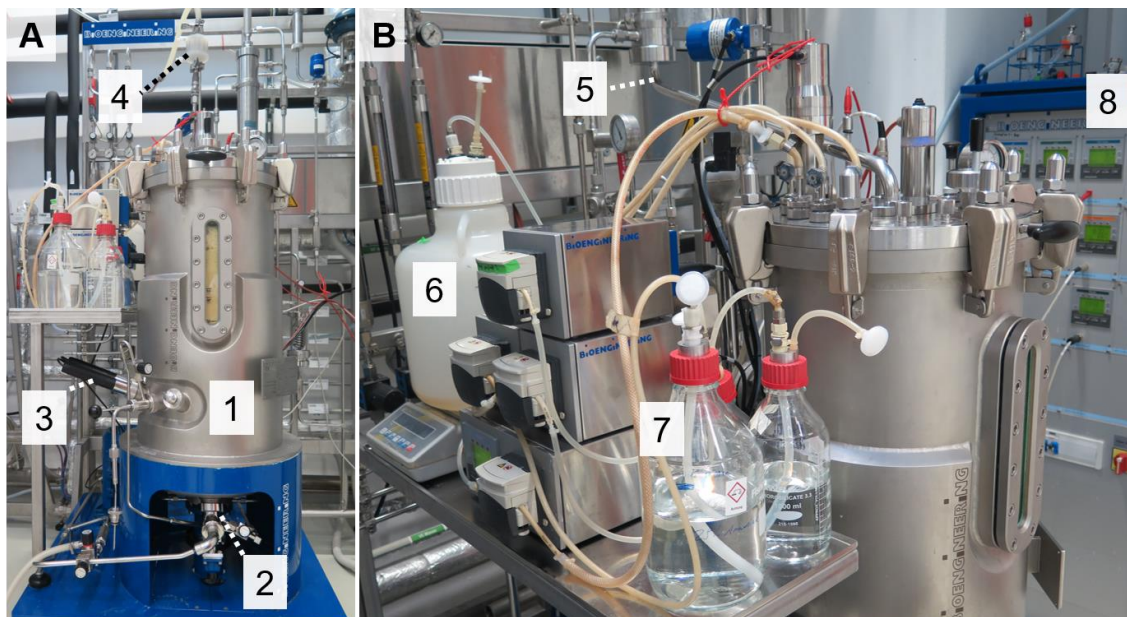


Figure 4.1: Front (A) and side view (B) of the 50 L bioreactor used for the production of *LbADH* WT. 1: Bioreactor, 2: Stirrer shaft, 3: pH, Temperature, and pO₂ sensors, 4: Sterile air flow (aeration at the reactor bottom), 5: Exhaust air flow, 6: Glucose feed supply (weight-controlled), 7: Acid/Base/Anti-foam supply, 8: Control units.

4.3.4 OD₆₀₀ and Biomass Determination

OD₆₀₀ of cell culture was determined in cuvettes using a UV/Vis spectrophotometer (GENESYS 10S, Thermo Fischer Scientific, Dreieich, Germany). Samples were diluted with the respective growth medium to reach absorption values within the linear range between 0.1 and 0.5.

Dry biomass determination was conducted in triplicates. 2 mL samples were transferred to 2 mL tubes, which were dried for 24 h and weighed beforehand. Tubes were centrifuged at 20 °C and 17,000 g for 2 min. The supernatant was discarded, and the opened tubes were dried at 80 °C for 48 h, prior to weighing.

4.3.5 Cell Harvest and Disruption

Cell pellets from shaking flask productions were thawed on ice and resuspended in 10 mL PBS containing 1 mM PMSF and 10 µg DNase I. Cells were disrupted by sonication (2×3 min, 90% intensity, 50% pulse, Sonoplus HD 2070 + Micro tip MS 72, BANDELIN electronic GmbH & Co. KG, Berlin, Germany). Cell debris were separated by centrifugation at 12000 g at 4 °C for 20 min and subsequent filtration through a 0.2 µm polypropylene syringe filter.

On the 50-L scale, cell disruption took place in a high-pressure homogenizer (Variete NS3015H; GEA Niro Soavi, Parma, Italy) (800 bar, Mass flow = 100 L h⁻¹). Cell debris were eliminated by technical filtration (1 µm pore size, WFMBA001; Wolftechnik, Weil der Stadt,

Germany) and crossflow microfiltration (0.45 mm pore size, Sartocon Hydrosart cassettes in Sartoflow Beta plus, Sartorius Stedim, Melsungen, Germany).

4.4 Protein Purification and Processing

Since some *LbADH* mutants even crystallized in protein buffer in the absence of PEG at low temperatures (<10 °C), all processing steps between protein purification and protein crystallization were conducted at room temperatures between 22–25°C.

4.4.1 Preparative Chromatography

On the mL scale, the supernatant was loaded onto a 1-mL nickel-affinity column (HisTrap High Performance column, ÄKTA Pure system, GE Healthcare Life Science, Munich, Germany) which was pre-equilibrated in binding buffer (20 mM sodium phosphate pH 7.0, 40 mM imidazole, 500 mM NaCl). After washing with an increased imidazole concentration of 67.6 mM, bound *LbADH* was eluted in the elution buffer (20 mM sodium phosphate pH 7.0, 270 mM imidazole, 500 mM NaCl).

On the 50-L scale, the permeate was loaded onto a 1 L nickel-affinity column (PureCube 100 Ni-NTA Agarose; Cube Biotech, Monheim, Germany) preequilibrated in binding buffer (20 mM sodium phosphate pH 7.0, 40 mM imidazole, 500 mM NaCl). Bound protein was eluted by running a linear gradient of 40–500 mM imidazole.

4.4.2 Buffer Exchange and Protein Concentration

On the mL-scale, *LbADH* fractions were dialyzed at 22–25°C against the protein buffer (20 mM HEPES-NaOH pH 7.0, 1 mM MgCl₂) by a factor of 1:10⁶ using a 14 kDa dialysis membrane (Membra-Cel, Serva, Heidelberg, Germany) while they were stirred gently. Generally, three subsequent dialysis steps were conducted with a duration of 1 h per dialysis step. Subsequently, protein solutions were concentrated to up to 20 g L⁻¹ by ultrafiltration (10 kDa MWCO Vivaspin 500, Sartorius, Göttingen, Germany) in a centrifuge which was tempered to 25 °C to prevent unwanted crystallization.

On the 50-L-scale, the main peak fraction was dialyzed against the protein buffer (20 mM HEPES-NaOH pH 7.0, 1 mM MgCl₂) via cross-flow ultrafiltration (10 kDa molecular-weight cutoff, Sartocon Slice Hydrosart Cassettes in Sartojet Alpha; Sartorius Stedim AG, Melsungen, Germany) and subsequent concentration to 30 g L⁻¹.

The purity of all purified *LbADH* solutions was assessed by SDS-PAGE. The *LbADH* concentration was determined by UV absorbance at 280 nm with a spectrophotometer (see 1.6.1).

4.5 Protein Crystallization

4.5.1 Static μL -Scale Crystallization

Vapor diffusion crystallization was mainly applied for the generation of large crystals suitable for neutron diffraction analysis in 24-well plates. Protein solution (usually 10–30 g L⁻¹ *LbADH*, 20 mM HEPES-NaOH pH 7.0, 1 mM MgCl₂) and crystallization buffer (usually 1 mM Tris-HCl varying pH, 0–200 mM MgCl₂, up to 100–200 g L⁻¹ PEG 550 MME [PEG monomethyl ether 550]) were mixed in identical amounts of 10 μL each and crystallized in CrystalBridges placed in 24-well ComboPlates (Greiner Bio-One, Frickenhausen, Germany) as sitting-drop vapor diffusion at 20 °C. Also, hanging drop vapor diffusion was applied by pipetting 10–20 μL of the solution onto a glass slide which then was placed upside down on top of the well and hermetically sealed with grease (see **Figure 4.2**). In both approaches, 1 ml of crystallization buffer was used as hygroscopic reservoir solution.



Figure 4.2: Crystallization well of a 24-well vapor diffusion crystallization plate. Inner well diameter = 16 mm. Depicted is the hanging drop technique.

Additionally, sitting drop vapor diffusion was applied for empiric crystallization screenings at the X-ray Crystallography Platform at Helmholtz Zentrum München. Two commercial screens (MPD and JCSG+ Suite, Qiagen, Venlo, Netherlands) were used, each with 96 different conditions. 0.2 μL of purified *LbADH* solution (3.5 g L⁻¹) was added to the same volume of the respective crystallization buffer. The reservoir contained 80 μL of the crystallization buffer. Pipetting was conducted using a mosquito nanodrop dispenser (SPT Labtech, Melbourn, England) (see **Figure 4.3**).

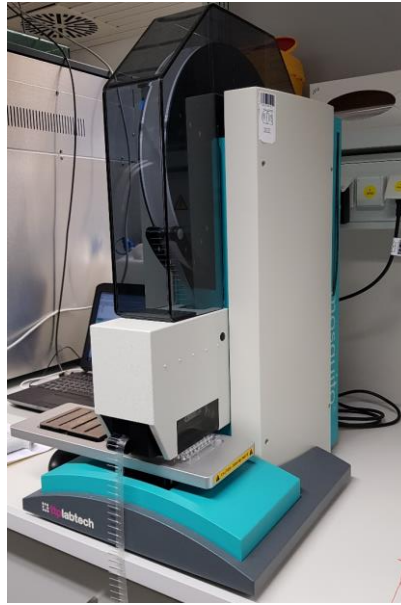


Figure 4.3: Mosquito nanodrop dispenser applied for empiric crystallization screenings (located at the X-ray Crystallography Platform at Helmholtz Zentrum München, Neuherberg, Germany).

Microbatch crystallization of *LbADH* variants was performed in 96-well microbatch plates (MRC UnderOil Crystallization Plate, SWISSCI, Neuheim, Switzerland). The protein solutions contained 1–10 g L⁻¹ *LbADH* in the protein buffer. The crystallization buffer was composed of 100 mM Tris-HCl at pH 7.0, 50 mM MgCl₂, and 0–200 g L⁻¹ PEG 550 MME. Equal amounts of crystallization buffer and protein solution were mixed in a 1.5 mL-polypropylene tube. Ten microliter drops were transferred to 96-well microbatch plates and sealed with transparent adhesive tape. Protein crystallization was conducted at 20 °C and monitored by automated microscopic imaging (see 4.6.5).

4.5.2 Stirred mL-Batch Crystallization

Stirred mL-batch crystallization was conducted in stirred crystallizers with a stirrer speed of 150 rpm (experimental DIY-setup, see **Figure 4.4**; Applied Arduino script to control the stirrer speed, see Appendix **B**). Experiments were performed with a total crystallization volume of 5 mL. Crystallization was conducted with purified protein and with dialyzed or clarified *E. coli* cell lysate. Experiments with purified protein started with an initial *LbADH* concentration of 10 g L⁻¹ (adjusted by spectrophotometric measurements). Experiments with cell lysate started with an initial *LbADH* concentration of approximately 2.5 g L⁻¹ (total protein concentration: 5 g L⁻¹). All crystallizers were placed in a temperature-controlled refrigerated circulator at 20 °C (No. 1157P, VWR, Darmstadt, Germany). 40 µL samples were taken manually, diluted with protein buffer by a factor of 1:10 to prevent further crystallization, and centrifuged for 30 s at 16,000g and 20 °C. The protein concentration of the supernatant was assessed by BCA assay.

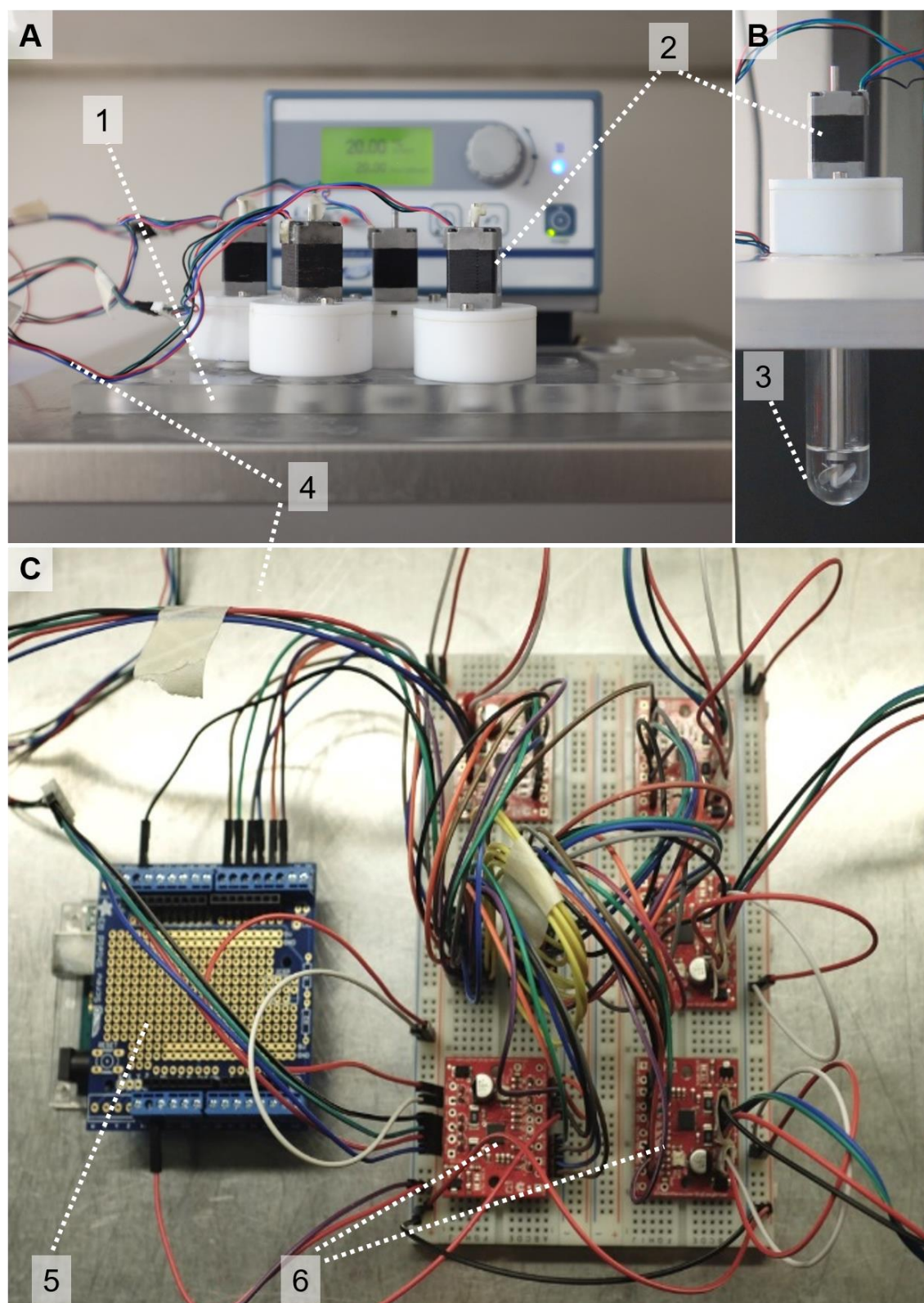


Figure 4.4: Experimental set-up for the stirred mL-experiments. (A) Stirred mL-crystallizers placed in the temperature-controlled water bath. (B) Side view of one stirred crystallizer (Working volume: 5 mL). (C) Stirrer control board. 1: Temperature-controlled water bath, 2: Stepper motors (Nanotec ST2818L1006-B), 3: Pitched-bladed impellers driven by a stepper motor ($n = 150 \text{ min}^{-1}$), 4: Cables connecting stepper motors and drivers, 5: Microcontroller (Arduino UNO Rev 3), 6: Stepper motor driver (Big easy driver, SparkFun Electronics).

4.5.3 Crystal Dissolution and Recrystallization

After reaching crystallization equilibrium, the crystal suspensions of the stirred mL-scale experiments were centrifuged (16,000g, 20 °C, 3 min) and the supernatant was discarded. Protein buffer was added, the crystal pellet was resuspended, centrifuged again, and the supernatant discarded. Different buffer were examined according to the ability to dissolve *LbADH* variants (see **Table 4.3**). The best buffer A (Protein buffer + 1 M MgCl₂) was added with the fourfold of the initial crystal suspension volume to dissolve the protein crystals. The samples were dialyzed against protein buffer and concentrated via ultrafiltration to obtain a volume of 2.5 mL. The spectrophotometric absorption at 280 nm of all samples was adjusted and recrystallization was started in stirred 5-mL-crystallizers by adding 2.5 mL of crystallization buffer (100 mM Tris-HCl pH 7.0, 50 mM MgCl₂, 200 g L⁻¹ PEG 550 MME) to 2.5 mL of *LbADH* solution.

Table 4.3: Buffer applied in the screening with the aim to find suitable conditions for quick and non-denaturing crystal dissolution of *LbADH* variants.

Dissolution buffer	Composition
A	Protein buffer + 1 M MgCl ₂ , pH 7.0
B	Protein buffer + 0.5 M MgCl ₂ , pH 7.0
C	Protein buffer + 0.5 M MgCl ₂ , pH 6.0
D	Protein buffer + 0.5 M MgCl ₂ , pH 8.0
E	1 M MgCl ₂
F	Protein buffer (pH 7.0)

4.5.4 Calculation of the Crystallization Yield

Crystallization yield (Y) in % was calculated according to the following equation:

$$Y = \left(1 - \frac{\Delta E_{LbADH, equ.} - \Delta E_{control, equ.}}{\Delta E_{LbADH, t=0} - \Delta E_{control, t=0.}} \right) \times 100$$

- with $\Delta E_{LbADH, equ}$ Extinction rate of *LbADH* sample in crystallization equilibrium, s⁻¹
 $\Delta E_{LbADH, t=0}$ Extinction rate of *LbADH* sample at crystallization start (t=0), s⁻¹
 $\Delta E_{control, equ}$ Extinction rate of negative control in crystallization equilibrium, s⁻¹
 $\Delta E_{control, t=0}$ Extinction rate of negative control at crystallization start (t=0), s⁻¹

ΔE values were obtained from spectrophotometric measurements at 6 s intervals for 10 min (Multiskan FC Microplate Photometer, Thermo Fisher Scientific, Darmstadt, Germany). The rate was determined from the initial linear slope. 20 μ L of crystal slurry supernatant were added to 180 μ L of protein buffer containing 10 mM acetophenone and 0.5 mM NADPH (further information on the enzymatic reaction and measurement see 4.6.3).

4.5.5 Phase Diagrams

Phase diagrams covering 96 conditions per *LbADH* variant were conducted at the group of Prof. Jürgen Hubbuch (Biomolecular Separation Engineering, KIT, Karlsruhe, Germany). 12 different PEG concentrations (X-axis) and 8 different *LbADH* concentrations (Y-axis) were tested according to the protocol of Baumgartner *et al.*, 2015, using 10 μL drops (5 μL of protein solution + 5 μL of crystallization buffer). Pipetting was conducted manually. The crystallization plate (MRC UnderOil Crystallization Plate, SWISSCI, Neuheim, Switzerland) was transferred to an imaging platform (Rock Imager 54, Formulatrix, Waltham, MA, USA), which periodically captured images of all plates. Temperature was set to 20 °C. Microscopic images were evaluated after all variants had reached equilibrium state (= no changes in visible by microscopy), which was true for *LbADH* variants after ~10 days. Evaluation was conducted by Anna Wöll (Biomolecular Separation Engineering, KIT, Karlsruhe, Germany) according to the of protocol of Baumgartner *et al.*, 2015.

4.5.6 Crystal Preparation for Neutron and X-Ray Crystallography

For neutron crystallography, the largest singular *LbADH* crystals with volumes above 0.3 mm^3 were selected. To achieve hydrogen/deuterium exchange of *LbADH* crystals, the reservoir solution in the 24-well crystallization plates was replaced four times with D_2O crystallization buffer using D_2O instead of H_2O (1 mM Tris-HCl pD 7.5, 50 mM MgCl_2 , 150 g L^{-1} PEG 550 MME) over 14 days at equal intervals. In preliminary diffraction experiments, we examined cryocooled conditions ($T = 100 \text{ K}$ and cryoprotection with 50% (v/w) deuterated glycerol before cooling in a cryostream) to be not conducive to high resolution diffraction, most likely due to micro cracks in the large, fragile protein crystals. The crystals only diffracted to 3.6 Å resolution. Therefore, all *LbADH* crystals investigated in this work were prepared and measured at room temperature which resulted in significantly higher resolutions compared with the cryocooled conditions. Prior to the room-temperature diffraction experiments, the crystals were mounted in self-made Teflon cryoloops (thread diameter 0.1 mm) on stainless-steel pins (catalogue No. MD-7-410, 18 mm; Molecular Dimensions, Suffolk, England), which were glued into the goniometer base (type GB-B3S; MiTeGen, Ithaca, New York, USA) and inserted into a quartz capillary (catalogue No. Z567361-5EA; Sigma-Aldrich, St Louis, USA). A drop of reservoir solution was placed at the opposite end of the capillary to avoid drying of the crystal. The capillary was sealed with epoxy glue. The preparation procedure was performed at room temperature at the Heinz Maier-Leibnitz Centre (MLZ), Garching, Germany.

For X-ray crystallography, single crystals were selected, which were longer than 10 μm . Crystals used for structural X-ray analysis were obtained both from the crystallization

experiments with purified *LbADH* and non-purified lysate. The crystals were mounted on a nylon fiber loop and flash-cooled to 100 K in liquid nitrogen. The cryoprotection was performed for two seconds in the crystallization buffer, which was supplemented with 25-30% (v/v) ethylene glycol. Crystal preparation was conducted by Dr. Sabine Schneider (Chair of Biochemistry, TUM, Garching, Germany) or by Dr. Robert Janowski (Institute of Structural Biology, Helmholtz-Zentrum München, Neuherberg, Germany).

4.6 Protein and Crystal Analyses

4.6.1 Protein Concentration Analysis

UV/Vis Spectroscopy

The absorbance at 280 nm of purified *LbADH* solutions was measured with a spectrophotometer BioSpectrometer Basic (Eppendorf, Hamburg, Germany) using a theoretical molar extinction coefficient of 19,940 L g⁻¹ cm⁻¹ (calculated with ProtParam; Gasteiger *et al.*, 2005). The protein concentration was calculated according to Lambert-Beer's law:

$$c = \frac{\varepsilon \times d}{E}$$

with	c	<i>LbADH</i> concentration	g L ⁻¹
	ε	Extinction coefficient <i>LbADH</i> at 280 nm	L g ⁻¹ cm ⁻¹
	E	Extinction	-
	d	Path length	cm

Bicinchoninic Acid (BCA) Assay

The BCA assay was applied to determine total protein concentration in impure solutions, such as cell lysate. BCA assay was also applied during stirred milliliter batch experiments with purified protein. The assay was conducted according to the manufacturer's protocol (Pierce BCA Protein Assay Kit, Thermo Fisher Scientific, Darmstadt, Germany).

4.6.2 *LbADH* Purity Analysis

SDS-PAGE

Samples were adjusted between 0.5 g L⁻¹ (purified *LbADH*) and 1 g L⁻¹ (cell lysate), denatured, and negatively charged using Laemmli buffer (Laemmli, 1970) prior to application into the wells of the SDS gel. No heating was conducted since this had been shown to result in partial degradation of *LbADH*. 35 mA per gel (300 V) were applied for

45 min. Protein staining was achieved by Coomassie staining according to Fairbanks *et al.*, 1971, or by InstantBlue staining (Expedeon, Cambridgeshire UK).

HCP-ELISA

HCP-ELISA was applied to measure the HCP concentration in *LbADH* samples, which were purified by crystallization and recrystallization. The method was conducted according to the manufacturer's protocol (*E. coli* BL21 (DE3) 360-HCP-ELISA type D, BioGenes GmbH, Berlin, Germany). Duplicates for the standards and triplicates for samples were measured.

4.6.3 Enzymatic Activity Assay

It was not the aim to achieve an activity optimum with the applied assay conditions, but to allow for fast and reliable measurements. The assay conditions were adapted from Kulishova, 2010, Schlieben, 2001, and Machielsen *et al.*, 2009. Enzymatic activities of *LbADH* variants were determined spectrophotometrically by detection of the NADPH oxidation to NADP⁺ during reduction of acetophenone to 1-phenylethanol in microtiter plates at 25 °C (Multiskan FC Microplate Photometer, Thermo Fisher Scientific, Darmstadt, Germany). 20 µL of *LbADH* solution (6 mg L⁻¹ *LbADH* in the protein buffer) was added to 180 µL of protein buffer containing 10 mM acetophenone and 0.5 mM NADPH. The absorption was measured at 340 nm (absorption maximum of NADPH) at 6 s intervals for 10 min. Additionally, NADPH oxidation rates were measured at reduced acetophenone (2.5 mM) or reduced NADPH (0.1 mM) concentrations to assess possible changes in the Michaelis-Menten constant (K_M). Specific enzymatic activities of *LbADH* variants were calculated using the following equation:

$$s = \frac{\Delta E \times V_{total}}{\varepsilon \times c \times d \times V_{enz}}$$

with	s	Specific enzymatic activity	U mg ⁻¹ (U = µmol min ⁻¹)
	ΔE	Extinction	min ⁻¹
	V _{total}	Total volume	[0.2] mL
	ε	Extinction coefficient NADPH at 340 nm	[6.22] mL µmol ⁻¹ cm ⁻¹
	c	<i>LbADH</i> concentration	[0.006] mg mL ⁻¹
	d	Path length	[0.59] cm
	V _{enz}	Volume of enzyme solution	[0.02] mL

Values in [brackets] were constant in all measurements. In most cases, enzymatic activities were given in relation to the WT, which was always measured in parallel on the same microtiter plate.

4.6.4 Stability Analysis

Thermal Shift Assay (TSA)

The TSA was applied to assess the thermal stability of *LbADH* variants. SYPRO Orange was used as hydrophobic fluorescent dye, which attaches to hydrophobic regions of the protein upon heating. The temperatures increased from 25 to 95 °C, with a heating rate of 1 K min⁻¹. The increasing fluorescence signal was measured (λ_{ex} 470 nm / λ_{em} 570 nm) by a Real-Time-PCR device, according to the protocol of Huynh *et al.*, 2015. 50 μL samples in triplicates were transferred to optical tubes (Agilent Technologies, Santa Clara, USA). A 50x SYPRO Orange solution with protein buffer (20 mM HEPES, 1 mM MgCl₂, pH 7.0) was diluted to a 6x concentrated solution and transferred to the protein solution shortly before the measurement. A sigmoidal fit of the curves was applied to calculate the turning points, which correspond to the melting temperatures (T_{m}) of the protein variants. All measurements were conducted at the Chair of Biomolecular Nanotechnology (Prof. Dietz, TUM, Garching, Germany).

Circular Dichroism (CD) – Thermal Transitions

Analogue to the TSA measurements a similar heat ramp was applied using a CD device (Chirascan plus CD spectrometer flushed with dry nitrogen; Applied Photophysics, Leatherhead, UK) and recording the thermal transitions of secondary to unfolded structures. *LbADH* samples were diluted to 0.25 g L⁻¹ with protein buffer (20 mM HEPES, 1 mM MgCl₂, pH 7.0) and transferred to a 106-QS quartz cuvette (Hellma, Müllheim, Germany) with 0.5 mm path length. A ramp was applied from 20–90 °C with a heating rate of 0.5 K min⁻¹. Thermal transitions were recorded at 210 nm. T_{m} was derived from a sigmoidal Boltzmann fit or double Boltzmann fit (Glover *et al.*, 2017) using the software Origin. Data were normalized by setting the signal of the folded protein to 0 and the unfolded protein to 1. All measurements were conducted in cooperation with Annika Strauch at the Chair of Biotechnology (Prof. Buchner, TUM, Garching, Germany). Furthermore, Far-UV CD spectra were recorded (see 4.6.6).

4.6.5 Automated Light Microscopy

Microscopic images of *LbADH* crystals in 96-well plates were photographed automatically at various time points and at multiple focus levels until crystallization equilibrium using a light microscope (Nikon Eclipse 50i, Nikon, Düsseldorf, Germany) with a 4-fold objective (CFI Plan Fluor) and an attached digital camera (DS-2Mv, Nikon). The microscope was operated and programmed via the software NIS Elements v3.2 imaging (Nikon, Düsseldorf, Germany). The software also allowed for crystal size measurements. The Microscope was placed inside an incubator (KB115, Binder, Tuttlingen, Germany) whose temperature was kept constant at 20 °C (see **Figure 4.5**).

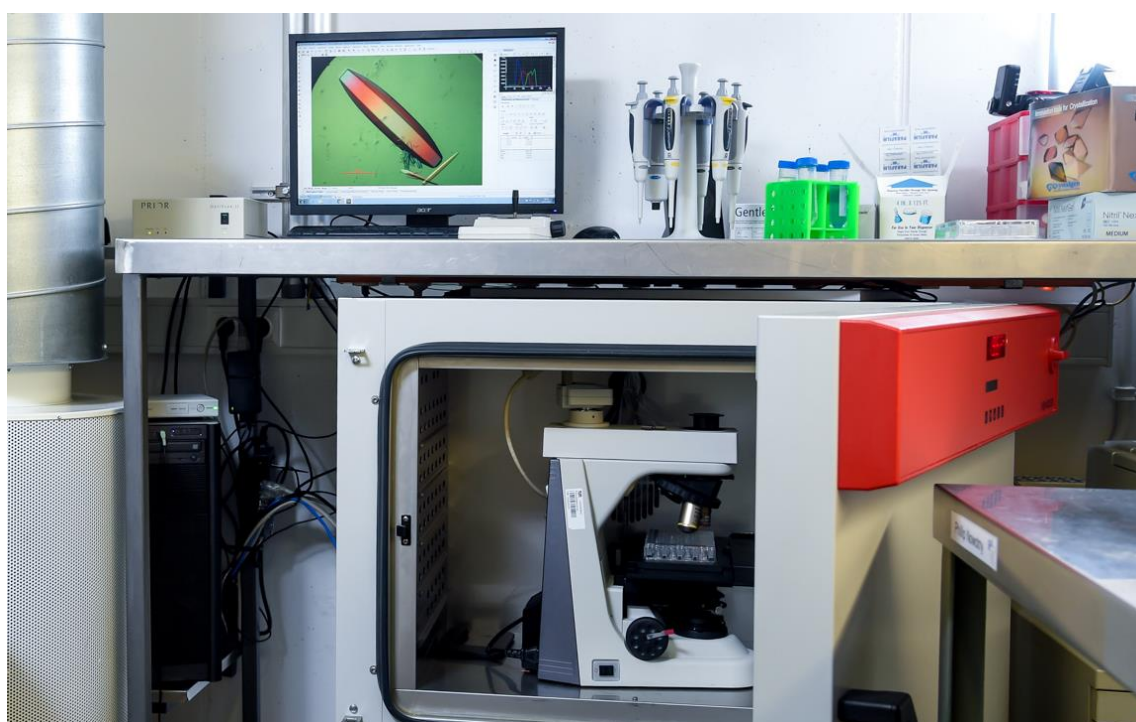


Figure 4.5: Applied automated light microscope for crystallization plates placed in an incubator (located in the crystal lab of the Institute of Biochemical Engineering, TUM, München, Germany).

4.6.6 Structural Analyses

Circular Dichroism (CD) Spectra

Far-UV circular dichroism (CD) spectra of *LbADH* variants were recorded at 20 °C using a Chirascan plus CD spectrometer (Applied Photophysics, Leatherhead, UK) flushed with dry nitrogen. *LbADH* samples were diluted to 0.25 g L⁻¹ with protein buffer (20 mM HEPES, 1 mM MgCl₂, pH 7.0). Spectra were collected from 280 to 185 nm in a 106-QS quartz cuvette (Hellma, Müllheim, Germany) with 0.2 mm path length. The measurement time per data point was 0.7 s. The depicted spectra reflect the average of ten individual measurements. As reference, the absorption spectrum of the protein buffer was measured.

The mean residual weight ellipticity (θ_{MRW}) was calculated using the following formula and plotted over wavelength.

$$\theta_{MRW} = \frac{\theta}{10 \times n \times c \times d}$$

with	θ	Measured ellipticity	mdeg
	n	Number of peptide bonds	-
	c	Protein concentration	M
	d	Cuvette path length	cm

All measurements were conducted in cooperation with Annika Strauch at the Chair of Biotechnology (Prof. Buchner, TUM, Garching, Germany).

Neutron Crystallography

Room-temperature neutron data were obtained with the BIODIFF instrument (monochromatic single crystal diffractometer; a joint project of TUM and Jülich Centre for Neutron Science (JCNS) at Heinz Maier-Leibnitz Centre (MLZ), Garching, Germany) by Dr. Tobias Schrader (JCNS, MLZ) and Dr. Andreas Ostermann (TUM, MLZ) (Ostermann & Schrader, 2015). For the neutron data set presented in this study and published in Hermann *et al.*, 2018, a crystal with approximate dimensions of 1.4 x 1.2 x 0.4 mm was used. A neutron data set was collected by Dr. Tobias Schrader at a wavelength of 2.7 Å at room temperature within 16 days. Data collection was performed over a total angular range of 82.5°, with a rotation range of 0.3° per frame and an exposure time of 1.5 h. The data were integrated by Johannes Hermann (Institute of Biochemical Engineering, TUM, Garching, Germany) in space group *I222*, with unit cell parameters a = 56.5, b = 84.6, c = 115.4 Å, at a resolution of 2.15 Å. Data reduction was performed by Johannes Hermann using HKL-2000 v.705b (Otwinowski & Minor, 1997).

X-Ray Crystallography

Diffraction data was collected on the ESRF beamline ID30A (The European Synchrotron Radiation Facility, Grenoble, France) by Dr. Sabine Schneider (Chair of Biochemistry, TUM, Garching, Germany) or on the SLS PXI X06SA and PXIII X06DA beamlines (Paul Scherrer Institute, Villigen, Switzerland) by Dr. Robert Janowski (Institute of Structural Biology, Helmholtz-Zentrum München, Neuherberg, Germany). All measurements were performed at 100 K. The following data analysis was conducted by Johannes Hermann and Daniel Bischoff (both Institute of Biochemical Engineering, TUM, Garching, Germany). The data

sets were indexed and integrated using *XDS* (Kabsch, 2010) and *AIMLESS* (Evans *et al.*, 2013). The structures were solved and refined using the *CCP4* software suite (version 7.0) (Winn *et al.*, 2011). An *in silico* mutated structure of PDB ID 6H07 (Hermann *et al.*, 2018) served as search model for molecular replacement with Phaser (McCoy *et al.*, 2007). Model rebuilding was performed in *COOT* (Emsley *et al.*, 2010). Further refinement was done with *REFMAC* (Murshudov *et al.*, 2011). The final structure was validated with *PDB-REDO* (Joosten *et al.*, 2014).

5 *LbADH* Process Implementation from Gene to Crystal

5.1 Choice for *LbADH* as Exemplary Protein

A suitable exemplary protein for this study needed to pertain to a list of criteria. To trace varying crystallization results back to single amino acid exchanges, the variations during processing of the protein should be minimized to limit their influence on the crystallization results. Furthermore, the preserved functionality of the mutants should be easily measured, and the protein should be of industrial relevance. The following list was developed initially and addresses the most prioritized criteria for suitable exemplary proteins, together with reasons why the decision was taken on *LbADH*.

- i. **Recombinant production in bacteria:** Bacterial cultivations are characterized as faster, more reproducible, and more facile in semi-controlled mL-scale cultivations compared to eukaryotic yeast or cell cultures. Plasmid-DNA-based cloning and mutagenesis is less time-consuming and less elaborate to validate.

E. coli BL21 (DE3) was chosen as production organism. Plasmid *pET28a*, bearing the *LbADH* gene and the kanamycin resistance gene, was used as template DNA for all cloning and mutagenesis steps. *LbADH* was recombinantly produced in the cytosol of the selected *E. coli* strain.

- ii. **Prokaryotic source:** Following up on the previous point, a prokaryotic protein was favored that can be produced in its native and active form in the cytosol of *E. coli*. Hence, the protein should lack posttranslational modifications, e.g. glycosylations and intermolecular disulfide bonding.

Native alcohol dehydrogenase from gram-positive lactic acid bacterium Lactobacillus brevis does not exhibit posttranslational modifications or disulfide bonding.

- iii. **Efficient protein purification:** The crystallization of protein variants was screened in purified form. To minimize process time and process variations, a 1-step purification via immobilized metal affinity chromatography (IMAC) was targeted.

While the C-termini of LbADH coordinate the tetrameric structure, the N-terminus does not possess such a crucial structural function (Niefind et al., 2003). Therefore, a His₆ tag was fused to the N-terminus. Three enzymatically active LbADH variants with different linker sequences were generated and successfully produced, purified, and crystallized after a single IMAC-step.

- iv. **Published crystallization conditions:** The approach of this study was to compare the crystallization behavior of redesigned mutants to that of the wild-type (WT) protein. Therefore, a protein was required, which was known to crystallize in its native, non-modified form. An own in-house empiric *de novo* crystallization screening of protein candidates was not considered as it was not the focus of this work.

Different crystallization conditions of LbADH were accessible from several publications (Niefind et al., 2000; Müller 2000; Schlieben 2001).

- v. **Simple validation of protein functionality:** For the purpose of technical use of protein crystallization, one of the most important parameters is the preservation of the protein's functionality upon mutagenesis. The functionality of all generated variants was supposed to be assessed by a simple and reliable assay.

In case of the biocatalyst LbADH, the enzymatic activities were the second most relevant screening parameter after crystallization behavior. It was measured by an UV/Vis spectrophotometric activity assay adapted from Müller 2000, Schlieben 2001, and Kulishova 2010.

- vi. **Industrial applicability:** A protein candidate should be chosen that is industrially applicable, because that is what the presented USP approach is.

LbADH is a biocatalyst for highly enantioselective reactions with a broad substrate range, demonstrated in various studies (see 3.1.4).

5.2 Production and Crystallization of *Lb*ADH WT

5.2.1 Linker Modifications

DNA plasmid pET28a was chosen as expression vector to start preliminary experiments with, due to existing N- and C-terminal His₆ tags. Since the C-terminus is crucial for the coordination of Mg²⁺-ions and therefore essential for the enzymatic activity (Niefind *et al.*, 2003) the incorporation of a C-terminal His₆ tag was excluded. An N-terminal His₆ tag in the initial variant *Lb*ADH_NHis led to a linker sequence of 11 amino acid sequences between tag and the protein (see Appendix, C). Therefore, the intention was to generate genetic variants of *Lb*ADH that exhibit no linker (*Lb*ADH_nL) or a shortened linker (*Lb*ADH_sL). Moreover, a redundant methionine at the N-terminus of the *Lb*ADH was eliminated in *Lb*ADH_nL and *Lb*ADH_sL ('AUG' codon is only coding for the transcription start in the WT enzyme as revealed by mass spectrometry, Müller, 2000). Additionally, three amino acids N-terminal of the His₆ tag, were intended to be substituted in both linker alternatives, by a single glycine (owed to the NcoI restriction site which introduces the start codon ATG followed by a triplet 'GNN').

The cloning approach led to the three desired genetic versions encoded on the plasmids pET28a_ *LbADH*_NH_{is}, pET28a_ *LbADH*_NH_{is}_nL and pET28a_ *LbADH*_NH_{is}_sL.

The basis for all experiments and presented results is the linker version *LbADH*_sL (unless explicitly stated otherwise). The decision based on the result that *LbADH*_nL revealed a significantly reduced enzymatic activity compared to *LbADH*_NH_{is} and *LbADH*_sL, and therefore was not taken into consideration. A slightly increased specific enzymatic activity of *LbADH*_sL could be explained by the reduction of ten non-catalytic linker amino acids. The *LbADH*_nL variant reveals a significant decrease in activity assuming a negative impact of the linker design on the protein conformation. *LbADH*_sL showed a slightly shifted nucleation zone towards lower concentrations (data not shown) and resulted in the best X-ray diffraction resolutions in preliminary X-ray diffraction experiments.

In the following, the used terms '*LbADH* WT' and 'WT' always refer to the selected short linker version *LbADH*_sL.

5.2.2 Recombinant Production

100-mL-Scale (Shaking Flasks)

The recombinant production workflow of *LbADH* was developed and optimized regarding highest possible reproducibility, and thus lowest possible influence on crystallization results. The following aspects resulted from theoretical considerations and experimental test runs:

- i. Productions always started with *E. coli* transformations which resulted in higher reproducibility compared to cultivations from glycerol stocks.
- ii. Proteins for one set of crystallization experiments (generally 4–6 mutants + WT for reference) were produced (and further processed) in parallel to avoid day-dependent environmental or handling variations.
- iii. Main cultures in non-baffled shaking flasks were inoculated by adjusting a start OD₆₀₀ of 0.05. Temperature was set to 30 °C throughout the whole process (initial temperatures of 37 °C and subsequent cooling to 30 °C during IPTG induction had shown to result in higher process-related deviations).
- iv. IPTG induction at OD₆₀₀ = 0.7–0.8 and 14 h induction time overnight resulted reproducibly in a biomass concentration of approx. 3.5 g L⁻¹ (OD₆₀₀ = 7) reached before the stationary phase.

After pellet washing, cell disruption, and purification, the yield was approximately 300 mg *LbADH* per L culture volume.

50-L-Scale (Bioreactor)

The protein production on a 50-L-scale was successfully performed once, therefore no optimization was carried out (process details see 4.3.3). After IMAC purification, buffer exchange, protein concentration and sterile filtration, 3.0 g *Lb*ADH per L reactor volume were achieved (50 L reactor volume resulted in 5 L sterile *Lb*ADH solution with a concentration of 30 g L⁻¹). The protein solution was used for neutron crystal screenings and for initial crystallization test on the stirred-mL scale. Furthermore, samples were provided for cooperation partners to support their research projects: Prof. Kind (KIT, Karlsruhe, Germany; Vacuum crystallization (1-L scale) of *Lb*ADH published in Barros Groß and Kind, 2018), Prof. Nirschl (KIT, Karlsruhe, Germany), and Prof. Kwade (TUB, Braunschweig, Germany).

5.2.3 1-Step Chromatographic Purification

It was aimed to crystallize all *Lb*ADH variants in highly purified form, and thus at well-defined conditions. There was a simultaneous attempt to minimize processing steps for the purposes of saving process time and optimizing reproducibility.

Purification via 1-step affinity chromatography took only approximately 30 min per mutant and enabled high *Lb*ADH purities of >99% (measured by HCP-ELISA). Overlaid chromatograms were highly similar (mono peak elution) indicating that the binding and elution behavior was not influenced by introduced mutations (exemplarily shown for WT and mutant T102E, see **Figure 5.1**). These results additionally confirmed the consistent production among *Lb*ADH variants, demonstrating that both biomass and *Lb*ADH concentrations were similar (column loading was proved to be below maximum binding capacity). It is conceivable that alternative chromatography methods (e.g. ion exchange or hydrophobic interaction chromatography) would have resulted in different binding and elution behavior of different variants, due to varying surface charges.

Analytical size exclusion chromatography (SEC) of IMAC-purified samples did not reveal any impurities (data not shown), and thus confirmed the HCP-ELISA results. *Lb*ADH samples, which were subsequently purified by IMAC and SEC did not yield significantly different crystallization results compared to a single IMAC purification step. Summarized, an optimal 1-step purification with purities >99% was achieved by a single IMAC step, which was applied throughout the following course this work.

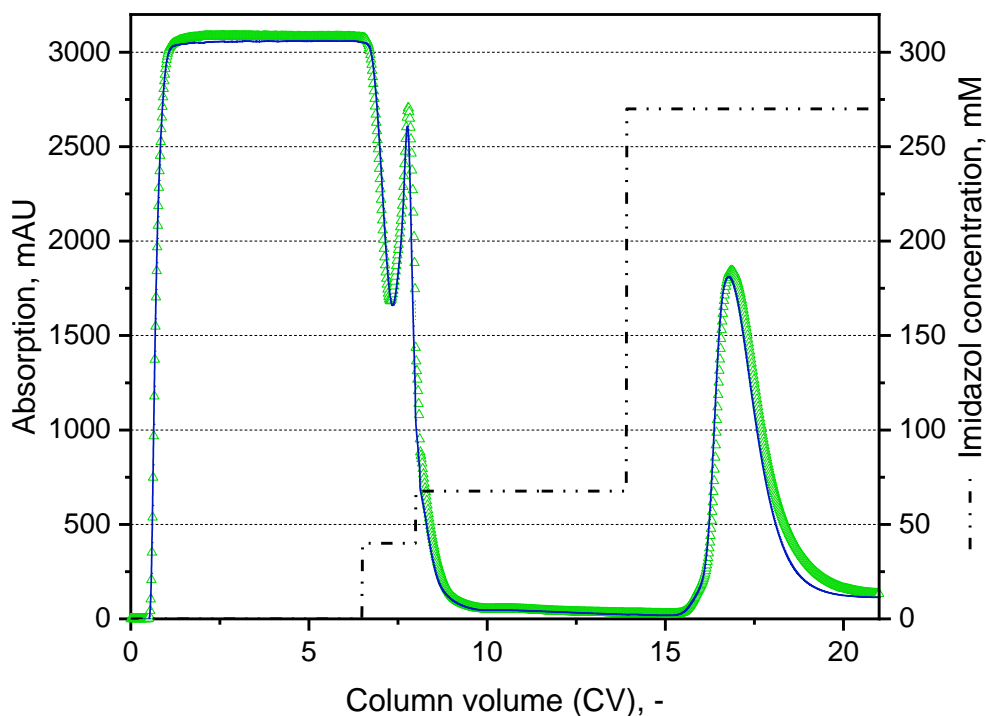


Figure 5.1: Overlaid IMAC chromatograms of *Lb*ADH WT (blue solid line) and mutant T102E (green triangles). The chromatogram can be divided into three phases: Sample application (0–6.5 CV), Washing #1 (6.5–8 CV), Washing #2 (8–14 CV), Elution (14–21 CV). 1 CV corresponds to 1 mL.

5.2.4 Initial Crystallization

Crystallization of *Lb*ADH for crystallographic purposes was already described in the literature, as discussed above. In the present work, it had to be verified whether the His₆-tagged variant is also crystallizable or whether the large, flexible His₆ hinders crystallization.

The first crystallization experiments with self-produced His₆-tagged *Lb*ADH (1-step purification) applying crystallization conditions from literature resulted in crystals shown in **Figure 5.2**, similar to experiments of un-tagged *Lb*ADH after 4-step purification (Schlieben, 2001). This initial result demonstrated that there is no significant influence of the His₆ tag on crystallization of *Lb*ADH.

Finally, these findings validated the successful in-house process implementation from gene to crystal of *Lb*ADH. Consequently, *Lb*ADH was defined as the exemplary protein of choice for all studies, presented in this work.

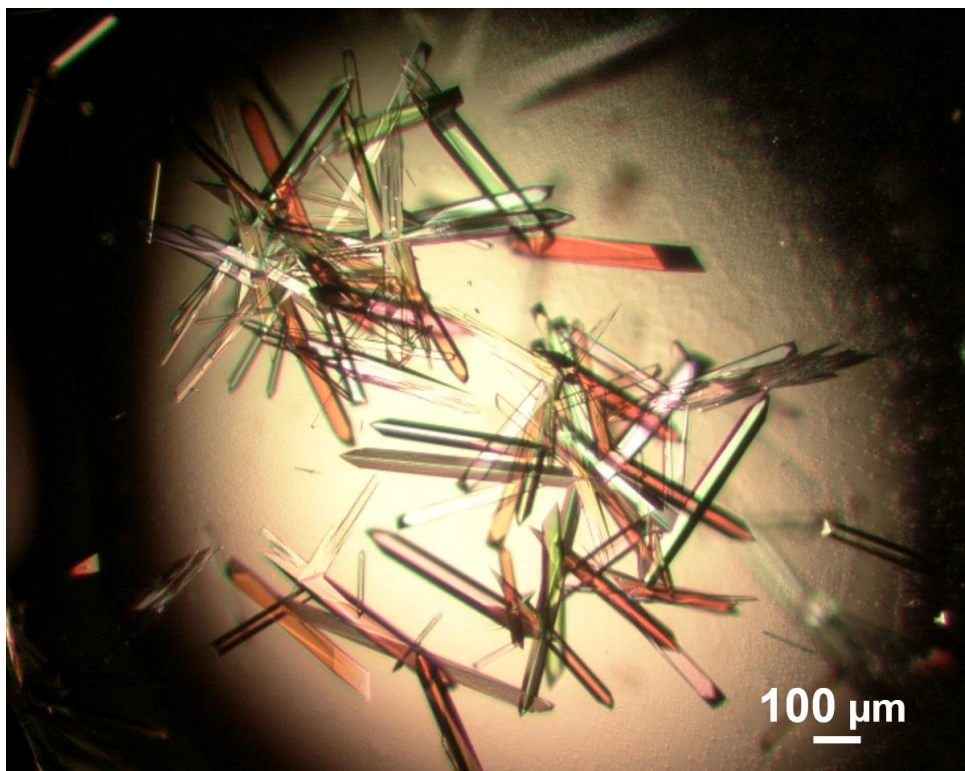


Figure 5.2: Microphotograph of the first protein crystals of His₆-tagged *LbADH* obtained after 1-step IMAC purification in hanging drop vapor diffusion crystallization experiments. Crystallization conditions were adapted from Schlieben, 2001. Protein solution: 10–20 g L⁻¹ *LbADH*; 20 mM triethanolamine (TEA) pH = 7.0, 5 mM MgCl₂, 150 mM NaCl. Crystallization buffer: 300 g L⁻¹ PEG MME 550, 0.1 M Tris-HCl pH 8.5, 50 mM MgCl₂, Reservoir solution: 1 mL of crystallization buffer. Temperature 20 °C. The microphotograph was taken after 24 h.

5.3 Crystallization Screenings

Based on these initial crystallization results, which confirmed the general crystallizability of His₆-tagged *LbADH*, two different crystallization screenings were performed that pursued two different goals:

- i. **Neutron crystallography screening** of *LbADH* WT aiming for large, well diffracting, singular crystals for neutron diffraction analysis
- ii. **Mutant screening** of rational engineered *LbADH* variants aiming for improved crystallizability for the purposes of technical crystallization.

5.3.1 Setup for The Neutron Crystallography Screening

Neutron crystallographic measurements were targeted to detect the orientation of regularly bound water molecules and networks of hydrogen bonding at the crystal contacts. Furthermore, protonation states of amino acids, interacting at the crystal contacts should be elucidated. A major requirement for neutron diffraction analysis at the BIODIFF instrument (Heinz Maier-Leibnitz Centre, MLZ, Garching, Germany), however, were large

protein crystals with a volume of $\sim 0.5 \text{ mm}^3$. In an empiric crystallization screening, multiple crystallization parameters were varied, including the protein concentration ($10\text{--}30 \text{ g L}^{-1}$), buffering agents (TEA [triethanolamine] and HEPES [4-(2-hydroxyethyl)-1-piperazine-ethanesulfonic acid]), pH of the protein and the crystallization buffer, concentration of crystallization agent (PEG 550 MME [polyethylene glycol monomethyl ether, 550 kDa]) and ionic strength (MgCl_2 concentrations), temperature, and crystallization method (hanging/sitting drop vapor diffusion, microbatch crystallization). The aim was to find conditions where the nucleation rate is low and thus, only few crystals are formed, before the solution reaches the metastable phase where only crystal growth can take place but no further nucleation. Hence, conditions needed to be found in which supersaturation occurs slowly during the vapor diffusion process – and not already at the mixing of protein and crystallization buffer. In practice, the first crystallization experiments proved to be hardly reproducible, especially when using the most widely used hanging drop vapor diffusion method. Since the sole aim of this approach was to generate a single large crystal, a time-consuming, systematic procedure was dispensed and instead a random screening was chosen, in which several parameters were changed simultaneously.

The largest crystals were obtained when protein solution (30 g L^{-1} *Lb*ADH, 20 mM HEPES-NaOH pH 7.0, 1 mM MgCl_2) and crystallization buffer (100 mM Tris-HCl pH 7.5, 50 mM MgCl_2 , 150 g L^{-1} PEG MME 550) were mixed in equal amounts of 10 μl each and crystallized as sitting-drop vapor diffusion in 24-well ComboPlates (Greiner Bio-One, Frickenhausen, Germany) at 20 °C. These conditions are similar to conditions published in Müller, 2001, in which a lower protein concentration (15 g L^{-1}), a crystallization solution with a higher pH (pH 8.9), hanging-drop instead of sitting drop vapor diffusion and a smaller drop volume (4 μl) were used (Müller, 2000). Single crystals became visible after 24 h, demonstrating the low nucleation rate at the applied conditions. In some experiments only one crystal per well had formed. Crystallization equilibrium was reached after approximately one week. Particular large crystals with crystal volumes of up to 1 mm^3 were obtained, suitable for neutron diffraction experiments (see **Figure 5.3**). Compared to all published data, these were the by far largest *Lb*ADH crystals ever reported.

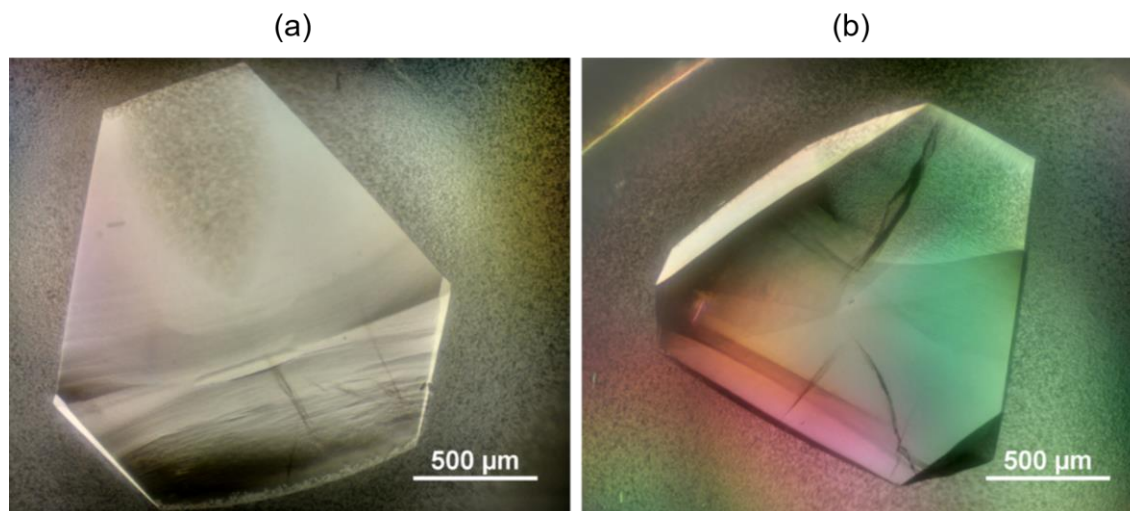


Figure 5.3: Microphotographs of (a) the largest (1.0 mm^3) and (b) the best neutron-diffracting *LbADH* crystal (0.7 mm^3). Microphotographs were taken after 7 days.

5.3.2 Setup for the Mutant Screening

For the purposes of technical crystallization, which was the focus of this work, the aforementioned conditions, leading to long nucleation induction times and long times until crystallization equilibrium, are not favorable. Instead, conditions would be suitable, which lead to increased nucleation rates and a shorter time until crystallization equilibrium. In this work, the impact of protein engineering on technical protein crystallization was investigated. The aim was not so much to find conditions where the WT crystallizes fastest, but to find crystallization conditions, which lead to crystallization equilibrium within an experimental time of 24 h, so that mutants with either faster or slower kinetics than the WT can be identified and microscopically monitored within a reasonable timeframe.

In addition, the crystallization method was changed from 24-well vapor diffusion to 96-well microbatch crystallization, which improved the reproducibility significantly and enabled higher sample throughput. The result of an empiric screening of different conditions in microbatch crystallization plates was similar to the conditions applied for crystallization for neutron crystallography. The crystallization buffer was composed of 100 mM Tris-HCl at pH 7.0, 50 mM MgCl_2 , and 150 g L^{-1} PEG 550 MME. The protein buffer contained 10 g L^{-1} *LbADH*, 20 mM HEPES-NaOH pH 7.0, 1 mM MgCl_2 . Presumably, already a small shift in pH from pH 7.5 to pH 7.0 had an enhancing effect on the nucleation rate. This could be due to the reduced solubility of *LbADH* at pH 7.0, which is closer to the theoretically determined isoelectric point (pI) of 6.1 (calculated with Protparam, Gasteiger *et al.*, 2005). The applied crystallization conditions and the applied microbatch crystallization method was defined as the final standard crystallization condition and was applied for all crystallization experiments on the μL -scale.

5.4 Crystallography of *Lb*ADH WT

5.4.1 Neutron Crystallographic Structure

The neutron diffraction experiment with the aforementioned *Lb*ADH crystal was performed after deuteration in cooperation with Dr. Tobias Schrader (Jülich Centre for Neutron Science (JCNS) at Heinz Maier-Leibnitz Centre (MLZ), Research Centre Jülich, Garching, Germany) and Johannes Hermann (Institute of Biochemical Engineering, TUM, Garching, Germany). Johannes Hermann refined the neutron structure to 2.2 Å (PDB ID 6H1M, space group *I*222, one monomer in the asymmetric unit; Hermann *et al.*, 2018). Initially, the neutron structure of *Lb*ADH was intended to deliver insights into hydrogen bonding networks at the crystal contacts of *Lb*ADH. Due to the relatively low resolution of 2.2 Å and higher residue flexibility at the protein surface, no hydrogen atoms of residues or water atoms were detectable at the crystal contacts. The generated neutron structure was analyzed by Hermann to elucidate the more fixed hydrogen bonding network, which connects the metal-binding N-terminus of *Lb*ADH with the catalytic center (Hermann *et al.*, 2018). It was the 64th published protein neutron structure in the Protein Data Bank (PDB).

5.4.2 X-Ray Crystallographic Structure

X-ray diffraction analysis of the identical protein crystal was performed by Sabine Schneider (Chair of Biochemistry, Technical University of Munich, Garching, Germany) on beamline ID30-A at the European Synchrotron Radiation Facility (ESRF, Grenoble, France). Johannes Hermann refined the high-resolution structure to 1.5 Å (PDB ID 6H07, space group *P*2₁2₂1, Hermann *et al.*, 2018) and compared the C^α-atoms to those of untagged *Lb*ADH (PDB ID 1NXQ, Niefind *et al.*, 2003). A calculated C^α root-mean-square deviation (r.m.s.d.) of 0.24 Å indicated a negligible impact of the His₆ tag on the overall *Lb*ADH structure (Hermann *et al.*, 2018). The His₆ tag did not result in detectable electron density, demonstrating the flexibility in the crystal and underlying the previous experimental finding, that the His₆ tag does not influence crystallization of *Lb*ADH significantly. A similar conclusion was drawn by Carson and co-workers, who reported that some purification tags can have no influence on protein crystallization (Carson *et al.*, 2007). The different space groups of the neutron structure (*I*222), and the X-ray structure (*P*2₁2₂1) were demonstrated to result in a highly similar crystal packing in the case of *Lb*ADH, with one monomer in the asymmetric unit in *I*222 and two monomers in the asymmetric unit in *P*2₁2₂1 (Hermann *et al.*, 2018). To date it is not known why *Lb*ADH crystallizes in these different space groups or why the evaluation of the data sets leads to different results.

The high-resolution X-ray structure of *Lb*ADH (PDB ID 6H07) was the three-dimensional structural foundation of all subsequent site-directed engineering approaches.

6 Crystal Contact Engineering of *LbADH*¹

6.1 Engineering Strategies

To the best of the author's knowledge, no crystal engineering towards improved technical crystallizability has been published in the literature before. Nevertheless, several crystallographic studies exist, which show that amino acid exchanges can enable or improve crystallization of proteins. In other cases, it was reported that protein engineering led to improved diffraction qualities during X-ray measurements (see 3.2.4). While most of those successful cases seem to be the result of random screening (since no rationale was described), the group of Derewenda developed the first and so far, only semi-rational *SER* strategy.

Nevertheless, literature gives distinct evidence that entropy reduction is not the only mechanism for improved crystallizability (see 3.2.4). Although many crystallization experts assume the enthalpic part, that is, attractive electrostatic interactions, to have a minor influence on protein crystallization, it was part of this work to investigate whether newly introduced electrostatic interactions at existing crystal contacts would also lead to improved crystallizability. A further basic motivation was that the crystal lattice can also be seen as a kind of quaternary structure, in which electrostatic interactions have been proven to play an important role (see 3.1.1).

Two main engineering approaches have been applied in the present work:

- i. The substitution of **entropically unfavored amino acids** at crystal contacts – the *SER* strategy developed by the Derewenda group (improving the entropic part of the Gibbs free energy towards crystallization)
Lysine to alanine (K→A); and glutamic acid to alanine (E→A) exchanges.
- ii. The generation of **salt bridges** (strongest electrostatic interactions) at crystal contacts (aiming for improving the enthalpic part of the Gibbs free energy).
Negatively charged amino acids glutamic (E) and aspartic acid (D) opposite of an existing positively charged (basic/cationic) amino acid, such as lysine (K), arginine (R), or histidine (H) and vice versa.

¹Results of this chapter are published in Nowotny *et al.*, 2019.

Furthermore, two weaker forms of electrostatic interactions at the crystal contacts were explored:

- iii. The generation of aromatic **π - π interactions** (involved in stabilization of quarterly structures, discussed in 3.1.1).

Aromatic amino acids F (phenylalanine), Y (tyrosine), or W (tryptophan) opposite of another aromatic residue.

- iv. The generation of **cation- π interactions** (stronger than π - π interactions, involved in stabilization of mainly tertiary structures, discussed in 3.1.1).

Cationic amino acids (K, R) opposite of aromatic amino acids (F, Y, W).

6.2 Crystal Contacts of *LbADH*

LbADH WT crystallizes in the space groups $I222$ or $P2_122_1$, both resulting in highly similar crystal lattices, as described above. Both crystal lattices of *LbADH* reveal three repetitive crystal contacts. These can be illustrated by four tetramers in the crystal lattice (see **Figure 6.1**). Crystal contact #1 at the tetramer's 'edges' comprises the largest amount of interacting amino acids (>10). Crystal contact #2 consists of only two interacting amino acids and it reveals a special point symmetry, since both amino acids are aspartic acids located at position 54 (D54). Crystal contact #3 exhibits a similar point symmetry with six interacting amino acids. All amino acid exchanges were conducted at these crystal contacts.

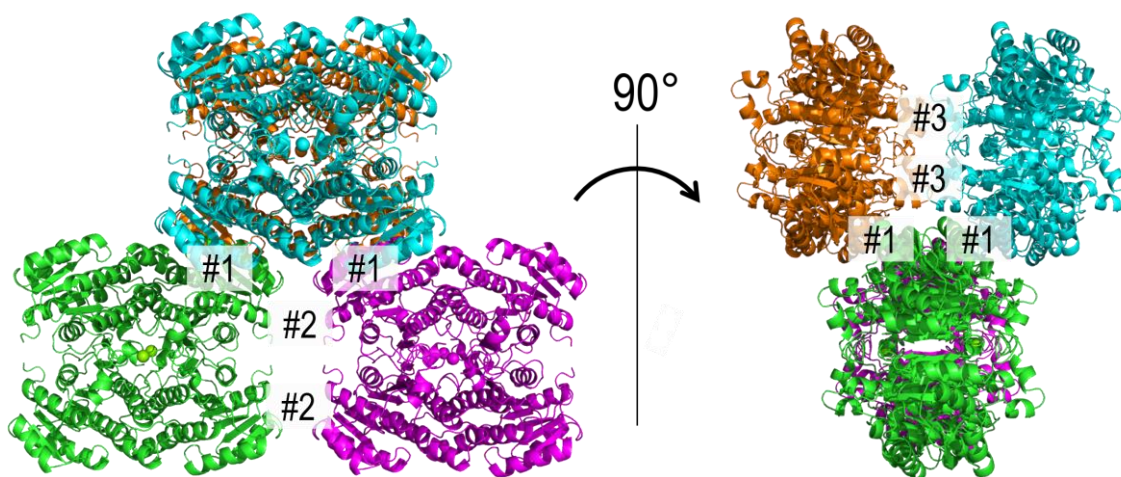


Figure 6.1: Arrangement of four *LbADH* tetramers in the crystal lattice and the three highlighted crystal contacts #1, #2, and #3. The figure was generated with the PDB ID 6H07 (WT) using PyMOL (v.2.1; Schrödinger).

6.3 Crystallization of *LbADH* Variants on the μL -Scale

6.3.1 Significance and Reproducibility of Varying Crystallization Results

Protein crystallization is described as poorly reproducible, since even small environmental variations can influence the crystallization process significantly. In other words, already small variations in crystallization conditions lead to different crystallizability. The initial question was: How much influence do single mutations have? Can environmental conditions be kept constant to not draw false conclusions? The aim and prerequisite of this study was to be able to trace different crystallization results back to individual amino acid exchanges. Although previous studies on engineering crystallizability for crystallography concluded that altered crystallizability is the result of amino acid exchanges, it is questionable if screening conditions were in fact identical. In none of the publications it is shown, for instance, that the purity levels of the mutants were the same (this can even be doubted because it was ion exchange chromatography, which was often used and which might have led to different binding and elution behavior in the case of surface mutations). It also appears that protein concentrations were not always consistent as only ranges were given in the methods section, indicating the applied protein concentration.

In initial crystallization approaches, the experiments were conducted in biological triplicates, meaning three experimental workflows at different time points each from *E. coli* transformation to protein crystal. The WT served as a reference in all experiments, which indicated whether crystallization conditions deviated from previous experiments (e.g. due to slight environmental changes). These initial experiments demonstrated that indeed there can be occasional variations in crystallization behavior of the same *LbADH* variant between different experiments conducted at different time points. However, these changes from one experiment to another each applied for all parallel investigated variants, meaning that crystallization of all parallel processed variants of one experiment was influenced into the same direction. In other words, all variants of one experiment crystallize with higher nucleation rate (more crystals) or all variants crystallize with lower crystallization rate (less crystals) compared to another experiment. An example is given in **Figure 6.2** on the basis of crystallization of WT and the first presented mutant Q126H.

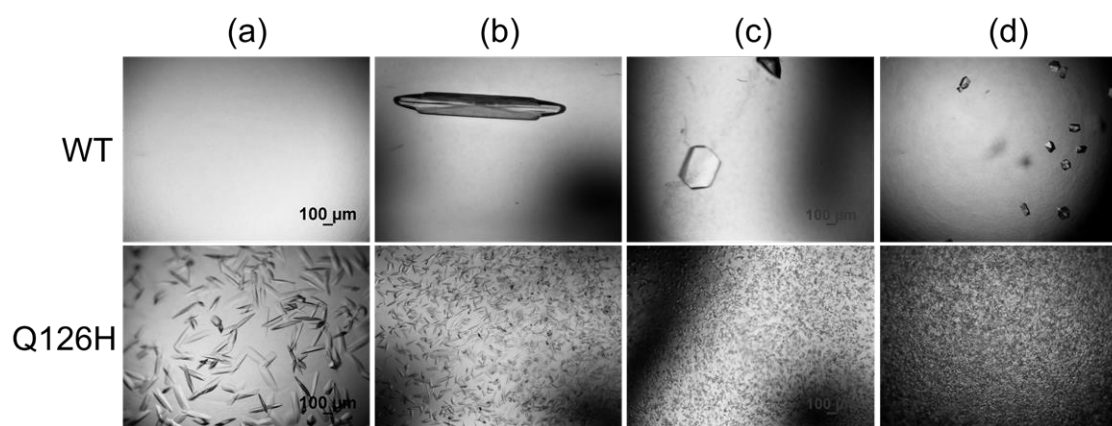


Figure 6.2: Crystallization microphotographs of *LbADH* WT and mutant Q126H from four individual experiments (columns a–d). The experiments are ranked according to the amount of crystals. Crystallization conditions were identical (5 g L^{-1} *LbADH* and 75 g L^{-1} PEG, $T = 20 \text{ }^\circ\text{C}$). Microphotographs were taken after 24 h.

A further experimental study should investigate the environmental or handling variations within one and the same experimental workflow. Therefore, not only the crystallization was conducted in multiple approaches, but also the production, the purification, and the crystallization were conducted in duplicates. In detail, the workflow started with two bacterial transformations per variant (WT and three mutants K32A, Q126H, and Q126K) and ended with 2×4 crystallization approaches. The result was very clear as the duplicates of all four variants WT, K32A, Q126H, and Q126K crystallized in a very similar manner (see **Figure 6.3**).

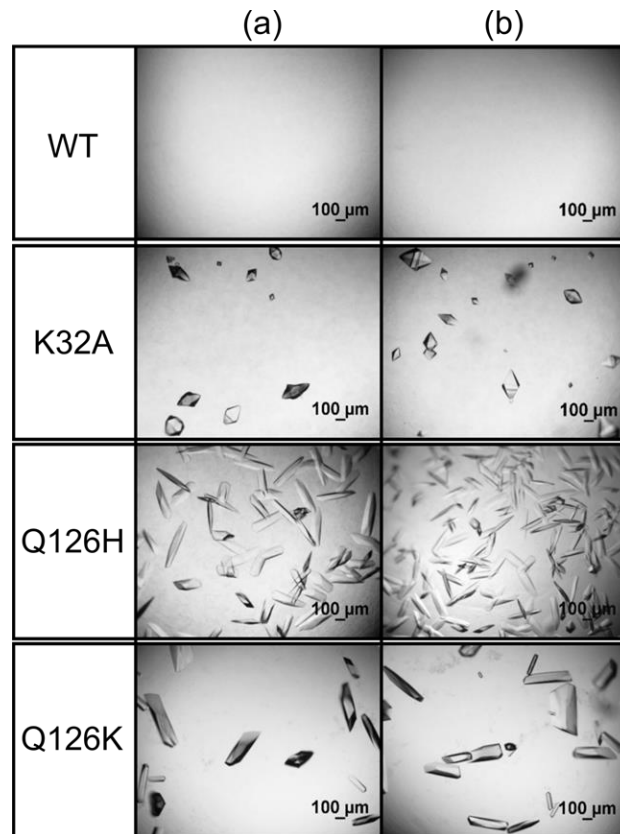


Figure 6.3: Crystallization microphotographs of *LbADH* WT and the mutants K32A, Q126H, and Q126K under standard conditions (5 g L^{-1} *LbADH* and 75 g L^{-1} PEG). (a) and (b) correspond to separate crystallization results from gene to crystal. Microphotographs were taken after 24 h.

The WT did only crystallize in a single event due to heterogeneous nucleation, which showed that the WT was able to crystallize but was not able to form nuclei at the respective condition (see **Figure 6.4**). In contrast, all three mutants K32A, Q126H, and Q126K crystallized reproducibly with more than 10 crystals per well. Between these mutants, the number of crystals, the crystal size, and the crystal morphology was consistently different. All *LbADH* variants revealed the same purity and concentration (see **Figure 6.5**). Consequently, the distinct crystallization behavior could clearly be traced back to individual single amino acid exchanges.

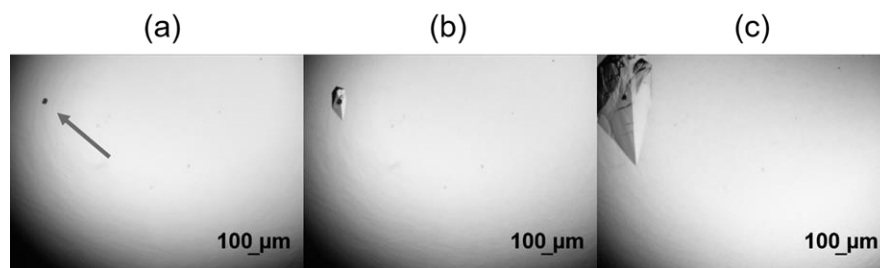


Figure 6.4: Heterogeneous crystallization of *LbADH* WT under standard conditions due to the presence of a foreign nucleating agent (indicated by the arrow) after (a) 0 h, (b) 24 h and (c) 48 h

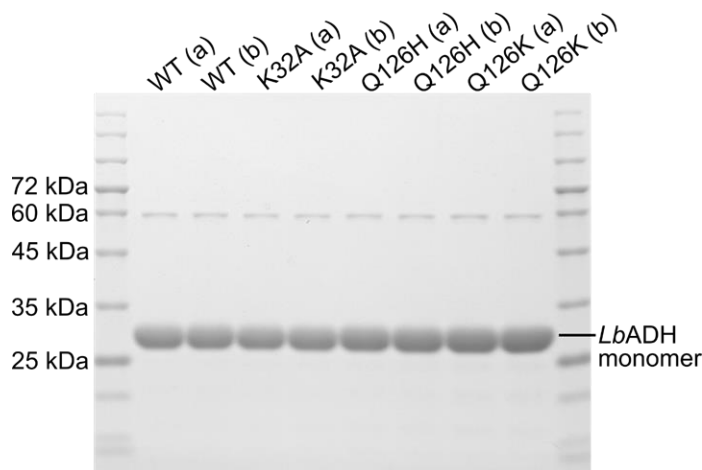


Figure 6.5: SDS-PAGE of *LbADH* WT and the mutants K32A, Q126H, and Q126K. (a) and (b) correspond to duplicative protein production starting from an individual *E. coli* transformation for each protein variant. Bands with a size of ~56kDa correspond to dimerized *LbADH* monomers; reduced concentrations of reducing agent β -mercaptoethanol in the Laemmli SDS buffer had shown to directly cause more intense ‘dimer’ bands (not shown).

Summarized, these first findings demonstrated, that variations in the crystallization conditions exist between experiments on the μ L-scale, conducted at different time points. Therefore, absolute results (e.g. the amount of crystals) cannot be compared between two different variants crystallized in two individual experiments. However, relative results are valid (e.g. Q126H crystallizes with a larger number of crystals compared to the WT) if the reference (in this case the WT) was produced, processed and crystallized in parallel and thus, was subject to identical production, processing, and crystallization conditions. Therefore, these results fundamentally proved that even single amino acid exchanges do have a significant influence on crystallization.

6.3.2 Characterization of Crystallizability

Characterization parameters needed to be defined to qualify or quantify altered crystallization behavior of *LbADH* mutants. These parameters should also describe the improved properties for technical crystallizability. At first, the crystallization success rate was assessed to validate improved crystallizability, analogous to the ‘crystallization score’ introduced in McElroy *et al.*, 1992. A higher crystallization success rate was defined as the percentage of wells where crystallization occurred in multiple crystallization experiments at a single tested crystallization buffer condition. However, this parameter was not optimal since it required a high experimental throughput for reliable data. Mutants, which had crystallized with a higher crystallization success rate, crystallized earlier and with a higher amount of crystals. Since more crystals were present during crystal growth phase, this period was shorter and hence, the crystallization equilibrium was reached earlier. Among

these parameters, the amount of crystals was the easiest one to assess microscopically, which was realized after 24 h.

The above-mentioned parameters reflect the crystallization kinetics at the standard crystallization condition (5 g L^{-1} *LbADH* and 75 g L^{-1} PEG, $20 \text{ }^\circ\text{C}$). Looking at the significantly increased nucleation rate of some mutants, it was assumed that the nucleation zone was shifted towards lower concentrations of protein and/or crystallization agent PEG. Therefore, crystallization experiments of the WT and the three mutants K32A, Q126H, and Q126K were conducted at reduced protein concentrations and reduced PEG concentrations (see **Figure 6.6**). No WT crystals were observed at reduced concentrations. In addition, mutant Q126K did not form any crystals at either reduced protein or PEG concentrations, although it crystallized reproducibly at standard protein and PEG concentrations. Mutant K32A did not crystallize at reduced PEG concentrations but crystallized at reduced protein concentration. Mutants Q126K and K32A therefore showed a high dependency on PEG for crystal nucleation. Mutant Q126H revealed the most significant shift of the nucleation zone towards lower PEG and protein concentrations.

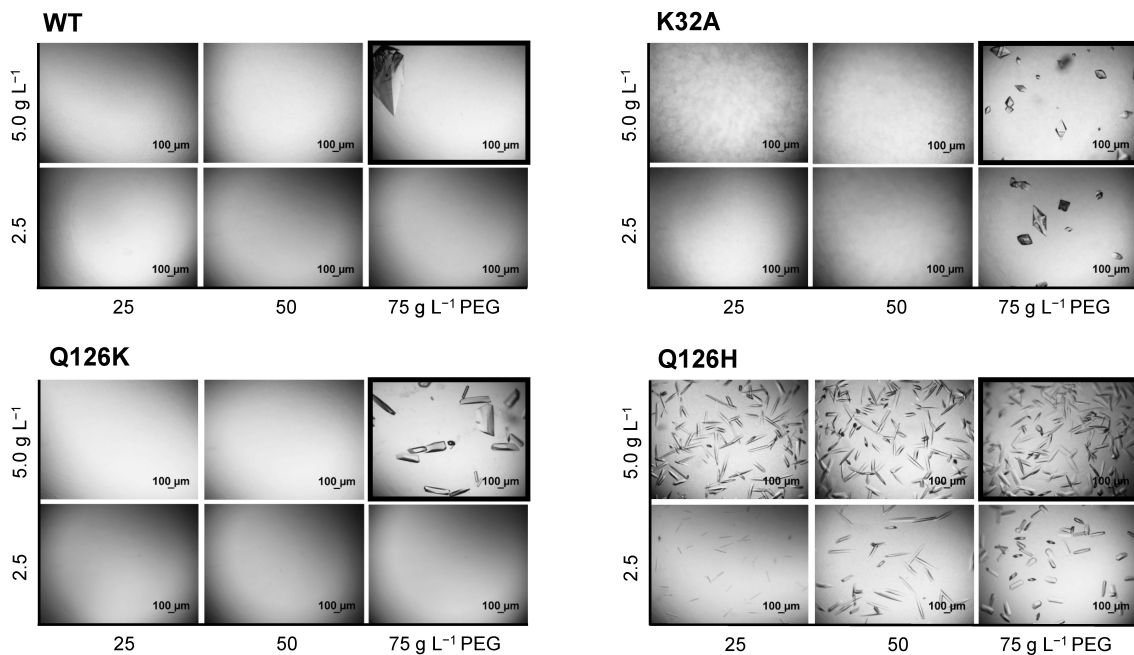


Figure 6.6: Crystallization microphotographs of *LbADH* WT and the mutants K32A, Q126K, and Q126H at standard conditions (top-right, framed images) and at reduced protein and PEG concentrations at $20 \text{ }^\circ\text{C}$. WT crystallization at the standard condition only took place in one out of eight experiments where heterogeneous crystallization took place (see Figure 6.4). Microphotographs were taken after 24 h.

This parameter also fulfilled a technical aspect of improved crystallization behavior, as it could be shown that for selected mutants a reduced use of crystallization agent was required, and less concentrated protein solutions could be used for the crystallization step.

Summarized, the following observable parameters correlate and define **enhanced crystallizability** on the μL -scale:

- i. A **higher crystallization success rate** per well (percentage of wells where crystallization occurred in multiple parallel crystallization experiments at identical conditions)
- ii. A higher **amount** of crystals per well in crystallization equilibrium (corresponding to a higher nucleation rate)
- iii. A shorter **nucleation** induction time (= until first crystals are visible)
- iv. A shorter period of **crystal growth** (shorter time between nucleation and crystallization equilibrium)
- v. A shorter time until crystallization **equilibrium**
- vi. A shifted **nucleation zone** (nucleation occurs at reduced PEG and protein concentrations)

The most applicable parameter to evaluate was the number of crystals after a defined crystallization time (e.g. 24 h), after which most crystallization approaches were already in crystallization equilibrium. For more precise differentiation between two similarly crystallizing variants, the start of crystallization was assessed based on automated imaging.

6.3.3 Mutant Screening on the μL -Scale

Crystal Contact #1

At this contact it was investigated whether *LbADH* variants with enhanced crystallizability can be generated. Mutants were divided into two subgroups:

- i. **SER variants:** Since there are only four lysines (K) and two glutamic acids (E) located at the crystal contact patches, we extended the *SER* strategy by with histidine (H) and arginine (R) (both reveal large, positively charged side chains similar to lysine) and aspartic acid (D) (large, negatively charged side chains similar to glutamic acid): K/E/H/R/D \rightarrow A
- ii. **Electrostatic interactions variants:** Investigations on whether new interactions (salt bridges, hydrogen bonding, cation- π - and π - π interactions) can be generated. In addition, biochemically similar residues were introduced.

All mutants are listed in **Table 6.1**. In this screening, one crystallization condition was tested. Selected mutants with significantly improved crystallizability (labelled in green) were investigated in detail in the further course of this work.

Table 6.1: List of all mutations at crystal contact #1. The mutations are divided into two groups: *SER* and Electrostatic interactions. Electrostatic interactions are divided into three groups: salt bridges, cation- π and π - π interactions. For all electrostatic interactions, possible interaction partners of the opposite monomer at the crystal contact are given (interaction partners, which would result in the respective interaction, are underlined). Mutants, which crystallized at the standard conditions (5 g L⁻¹ *LbADH* and 75 g L⁻¹ PEG, 20 °C) within 24 h are displayed in **blue**, mutants with significantly enhanced crystallizability compared to the WT (at least 2-fold number of crystals in the equilibrium) are displayed in **green** and non-crystallizable in **red**.

<i>SER</i>	Electrostatic interactions					
	Salt bridges		Cation- π		π - π	
Mutation	Mutation	Partner	Mutation	Partner	Mutation	Partner
E28A	H39D	D74/E77/ <u>R127</u>	H39F	D74/E77/ <u>R127</u>	L16W_T70F	<u>mutually</u> + V42
K32A*	H39E	D74/E77/ <u>R127</u>	H39W	D74/E77/ <u>R127</u>	D41F_Q126F	<u>mutually</u> + K45
R38A	K45R	<u>E66/T103/R122/Q126</u>	D41F	<u>Q126/R127</u>	K45Y_R122F	<u>mutually</u> + E66/T103/R122/Q126
H39A	K48R	<u>T102</u>	E66F	<u>K45</u>	K45W_T103F	<u>mutually</u> + E66/R122/Q126
D41A	E66D	<u>K45</u>	E66W	<u>K45</u>	K45W_R122F	<u>mutually</u> + E66/T103/R122/Q126
E44A	K71H	P193/ <u>D197</u>	T70F*	<u>K45/D41/V42</u>	T103F_R122F	<u>mutually</u> + E66/Q126/K45
K45A	K71R	P193/ <u>D197</u>	T103F	<u>K45</u>		
K48A	D74E	<u>R38/H39/V42</u>	R122F	<u>K45/E66</u>		
D67A	T102E*	<u>K48</u>	R122W	<u>K45/E67</u>		
K71A	T103D	<u>K45</u>	Q126F	D41/ <u>K45</u>		
E100A	Q126H*	S40/ <u>D41/E44</u>	D197F	<u>K71</u>		
D197A	Q126K*	S40/D41/ <u>E44</u>	D197W	<u>K71</u>		
	D197E	<u>K71</u>				

*crystallization behavior of selected mutants was analyzed in more detail in the following

Several more mutants were investigated but were not successfully recombinantly produced or purified: L16W, K45Y, K71F, R127A, D197Y, H39F_R127F, K45F_T103F, K45F_R122F, K45W_R122W, K45Y_T103F, and T103F_D197Y. The reason for this (e.g. handling errors or insoluble protein) was not further explored, however, it is noticeable that in 10 out of 11 cases, these are variants where aromatic amino acids were introduced.

The screening revealed that crystallization can be improved by introducing charged amino acids in order to generate electrostatic interactions. The ‘salt bridge’ approach even led to the highest rate of crystallizable variants (10 out of 13) and the highest rate of variants with significantly improved crystallizability (3 out of 13). The exchange of biochemically similar amino acids led to similar crystallization results (e.g. 3 out of 3 K→R exchanges and 2 out

of 3 E→D or D→E exchanges). The *SER* strategy led to one variant with significantly improved crystallizability (1 out of 12). The introduction of aromatic amino acids (cation- π and π - π interactions) led to mostly non-crystallizable variants and no variant with improved crystallizability was identified. The detailed crystallization behavior of the best-crystallizing mutants K32A, Q126H, and Q126K on the μ L-scale was shown above (see 6.3.1 and 6.3.2), except for T102E, which is shown in the following work. The crystallization behavior of all four mutants on the stirred-mL scale is shown in the following.

Mutant T70F is one representative of *Lb*ADH mutants, which did not crystallize in the screening. This variant was crystallized exemplarily at higher PEG concentrations. It could be shown that in this case the nucleation zone is shifted in the direction of higher PEG concentrations (see **Figure D.1**).

Crystal Contact #2

This contact is a special case as it comprises only one interaction of two identical, facing residues. Both residues have the same position (D54), hence it is a symmetric crystal contact. Therefore, this crystal contact was suitable for the investigation of pairwise interactions of identical residues. A saturation mutagenesis was conducted, which covered all 20 amino acids. Mutants, which crystallized within 24 h, are displayed in blue, mutants with significantly enhanced crystallizability compared to the WT (at least 2-fold number of crystals in the equilibrium) are displayed in green, and non-crystallizable in red:

D54A, D54C, D54E, D54F*, **D54G, D54H, D54I, D54K, D54L, D54M, D54N, D54P, D54Q, D54R, D54S, D54T, D54V, D54W**, and **D54Y***.

(*Crystallization behavior of selected mutants was analyzed in more detail in the following.)

Again, the observation of crystal contact #1 is confirmed that the exchange of biochemically similar amino acids leads to similar crystallization behavior (D54E). In contrast to previous findings, it is highly significant that all aromatic residues lead to enhanced crystallizability, which suggested that the contact was intensified via π - π stacking. This assumption was explored by X-ray diffraction, presented in the following. The detailed crystallization behavior of the best-crystallizing mutants D54F is shown in the following work (D54Y see **Figure D.2**).

Crystal Contact #3

Selected amino acid exchanges, which led to improved crystallizability in crystal contacts #1 and #2, were transferred to the investigation of crystal contact #3. At this crystal contact the WT amino acid at position 207 interacts presumably with the facing counterpart at the same position. It was investigated whether facing (ion mediated) acidic amino acids or facing aromatic amino acids would enhance crystallizability. Mutants, which crystallized within 24 h (however, not better than the WT), are displayed in blue, and non-crystallizable in red.

Q207D, Q207E, Q207F, Q207W, Q207Y.

The detailed crystallization behavior on the μL -scale is illustrated in **Figure 6.7**. It is shown that only WT and mutant Q207D crystallize at the standard condition within 24 h. By increasing the PEG and the protein concentration, crystallization of mutant Q207E was triggered. Q207E and Q207D crystallized in a similar way, further confirming that the exchange of biochemically similar amino acids leads to similar crystallization behavior. Both mutants crystallized significantly slower than the WT, demonstrating a decrease in crystallizability of engineered mutants. After approximately 7 days, all aromatic variants (Q207F/Y/W) also started to crystallize.

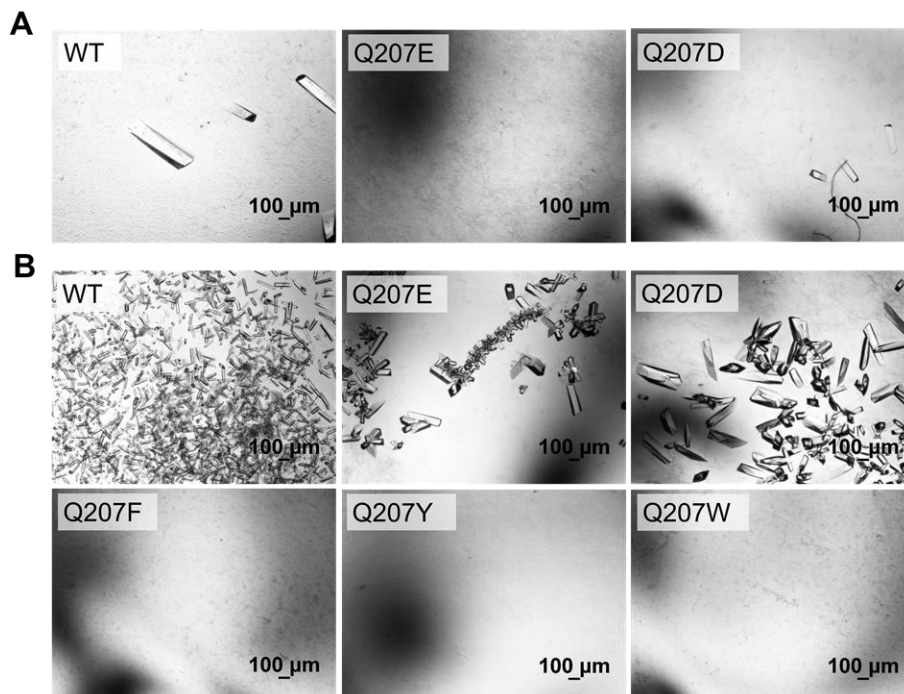


Figure 6.7: Crystallization microphotographs of *LbADH* WT and the mutants Q207D, Q207E, Q207F, Q207Y, and Q207W at (A) standard condition (5 g L^{-1} *LbADH* and 75 g L^{-1} PEG) and (B) at increased protein and PEG concentrations (10 g L^{-1} *LbADH* and 100 g L^{-1} PEG). At the standard condition, only the WT and mutant Q207D crystallized within 24 h. Microphotographs were taken after 24 h.

Summarized, the crystallization results of the mutant screening showed a complex picture:

- i. The introduction of charged residues, aiming for salt bridges, resulted in more positive hits than the *SER* strategy.
- ii. The introduction of aromatic amino acids, aiming for cation- π and π - π interactions, did not result in improved crystallizability (except for crystal contact #2, where π - π interactions were assumed).
- iii. Similar residues (e.g. E and D) led to similar crystallizability.
- iv. The variants **K32A**, **D54F**, **D54Y**, **D54W**, **T102E**, **Q126H**, and **Q126K** crystallized significantly better than the WT.

One needs to keep in mind that the main part of the screening was conducted based on a single crystallization condition. This means that there might be false negative results (e.g. precipitated variants, which would have crystallized at reduced protein and PEG concentrations). In contrast, the positive hits were shown to be better crystallizable in a very reproducibly manner. The subsequent studies concentrated on the detailed exploration of the crystallization and protein properties of the best-crystallizing mutants.

6.3.4 Phase Diagrams of Selected Mutants

Microbatch crystallization experiments were conducted to generate a phase diagram for *LbADH* variants in equilibrium state. WT and the best-crystallizing mutants at the time of conducting these experiments were selected, that is Q126K, Q126H, K32A, and D54F. After 10 days, in none of the plates a further phase change was visible. This time point was defined as the equilibrium state, and thus the begin of evaluation of the phase diagram.

LbADH WT consistently crystallized at high PEG and low to intermediate protein concentrations (nucleation zone, see **Figure 6.8** green diamonds), and co-precipitated at higher protein concentrations (precipitation zone, bright blue triangles). Crystallization or precipitation occurred after liquid-liquid phase separation (LLPS, yellow diamonds) at intermediate PEG and protein concentrations. Low concentrations of PEG and protein did not affect the soluble state until day 10 (grey spheres). *LbADH* sporadically crystallized also at low PEG concentrations. The phase diagram of mutant Q126H illustrates a clear shift of the nucleation window towards lower PEG concentrations, which reflects the above presented observations (compare **Figure 6.6**), where Q126H was the best-crystallizing mutant among the variants WT, K32A, and Q126K. The phase diagram of mutant Q126K is similar to the WT, the phase diagram of K32A shows a shift of the precipitation zone towards lower protein concentrations. However, the data do not enable a statement to be made as to whether the nucleation zone has also been shifted towards lower protein concentration since measuring points below the lowest measured protein concentration

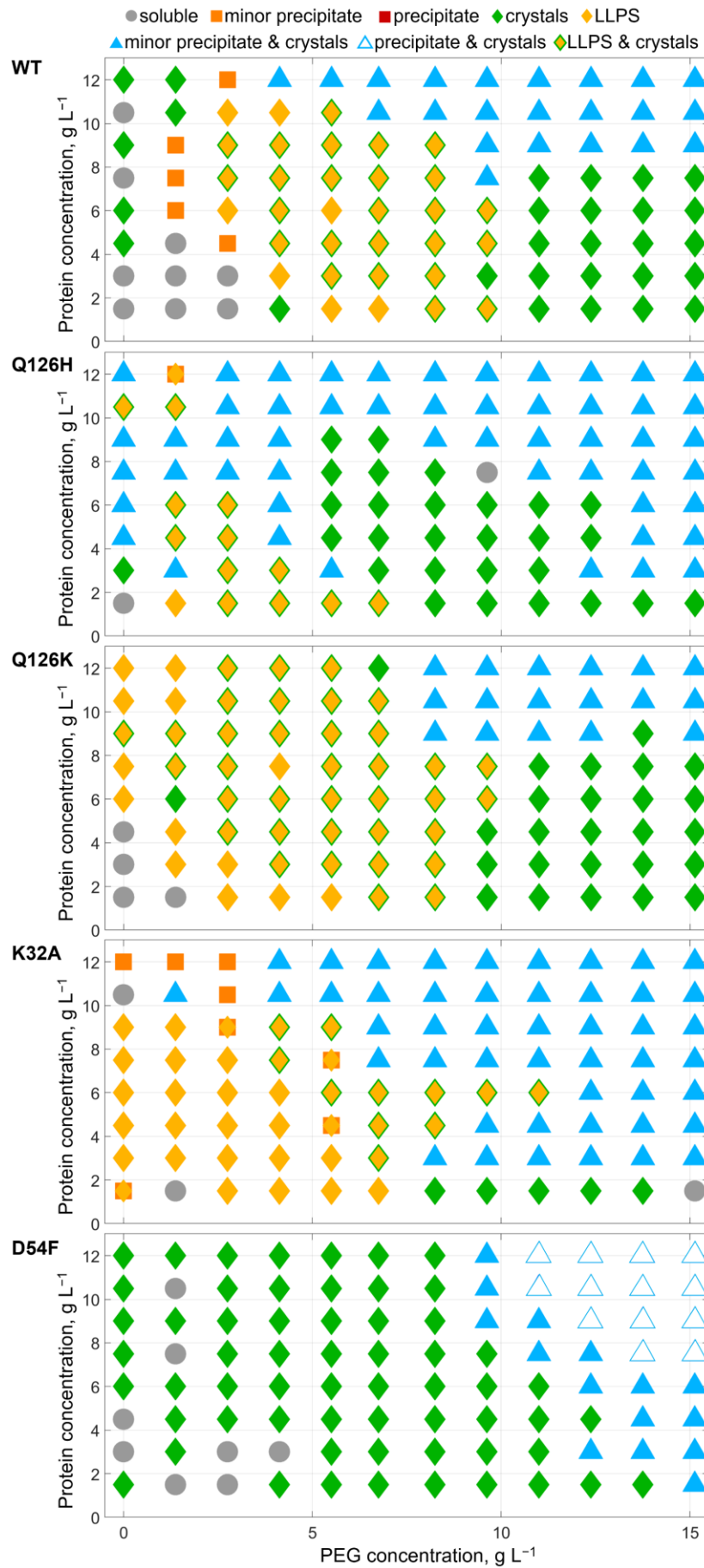


Figure 6.8: Phase diagrams of *LbADH* WT and the mutants Q126H, Q126K, K32A, and D54F. Microphotographs were evaluated after 10 days. (LLPS = liquid-liquid phase separation).

(1.5 g L⁻¹) are missing. The crystallization results of mutant D54F were even more significant than those of mutant Q126H. The nucleation zone is clearly extended towards lower protein concentrations. The change in the precipitation window is shifted towards higher PEG but lower protein concentrations.

6.4 Structural Analysis of *LbADH* Mutants

The three-dimensional structures of *LbADH* mutants were analyzed by X-ray diffraction with the following intentions:

- i. To validate whether the crystal packing, and thus the crystal contacts are preserved after mutagenesis
- ii. To find explanations of improved crystallizability on an atomistic level.

6.4.1 Crystal Packing

In **Table 6.2** all mutants are listed, which were analyzed by X-ray diffraction, together with their corresponding space groups, resolution and PDB IDs. All mutants crystallized in the space groups $P2_122_1$ and $I222$, meaning that there was no random reorientation of crystal contacts (explanation see 5.4.2).

Table 6.2: List of WT and all single mutants, which were analyzed by X-ray diffraction together with the corresponding space groups, resolution and PDB IDs.

Variant	Space group	Resolution, Å	PDB ID
WT	$P2_122_1$	1.5	6H07
K32A	$I222$	1.6	6HLF
K48A	$P2_122_1$	1.3	n.p.
D54F	$P2_122_1$	1.4	6Y1C
E100A	$I222$	1.2	n.p.
T102E	$P2_122_1$	1.4	6Y0S
Q126H	$I222$	1.2	6Y10
Q126K	$I222$	1.2	6Y0Z
Q207D	$I222$	1.2	n.p.
Q207Y	$P2_122_1$	1.4	n.p.

n.p. = structure not published and not refined in all cases. In these cases, the main purpose was to identify the space group (statement on preserved crystal packing).

This result confirms the general approach followed in this work: Amino acid exchanges were generated based on the WT's crystal contacts (= structure template) and as expected, these changes were observed at the crystal contacts for all mutants.

6.4.2 Altered Crystal Contact Interactions

X-ray structures of *Lb*ADH variants were mainly used to visualize the redesigned crystal contacts, and thus to validate the effect of the applied engineering strategy. In the following, the altered crystal contact interactions of the six best-crystallizing mutants K32A, D54F, D54Y, T102E, Q126H, and Q126K are presented, each in comparison to the WT crystal contact. For better illustration, the colors of the tetramers depicted in the following images are identical to the overview **Figure 6.1**.

K32A

The mutation K32A was introduced according to the *SER* strategy. It took place at a crystal contact comprised of two single aspartic acids (D54) facing each other (see **Figure 6.9**). Water or ion-mediated interactions may occur. Lysine (K32) has a positively charged, large flexible sidechain that is located next to D54. Both amino acids might form temporary mutual ionic intramolecular interactions. In mutant K32A, this intramolecular interaction is eliminated. An indicator for an enforced crystal contact of mutant K32A is the shorter distance that would allow for hydrogen bonding. Furthermore, the incorporation of a fixed Mg^{2+} -ion between both facing D54 residues, hence, an ion-mediated electrostatic interaction can be assumed according to MD simulations conducted by Johannes Hermann (data not shown). This fixed Mg^{2+} -ion is missing at the indicated position of the WT crystal. Although this mutation is also proposed by the *SERp* server (Goldschmidt *et al.*, 2007), the crystallographic results reveal that this K→A mutation has – if any – not only a positive entropic effect, but an indirect effect on an enhanced ion-mediated electrostatic interaction.

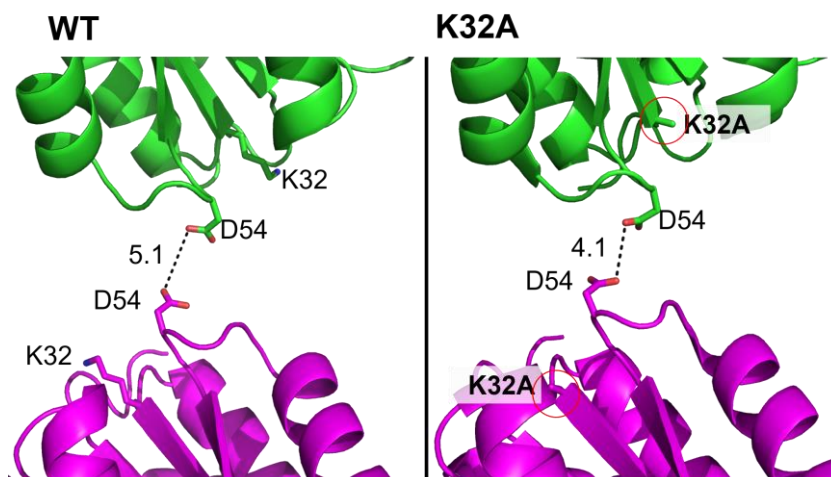


Figure 6.9: Crystallographic image illustrating the crystal contact #2 of *Lb*ADH WT and K32A. Green and magenta colored cartoon structures are sections of two *Lb*ADH tetramers interacting in the protein crystal. Mutation Alanine Distances (in Å) are depicted by the dashed lines. The figure was generated with the PDB IDs 6H07 (WT) and 6HLF (K32A) using PyMOL (v.2.1; Schrödinger).

D54F and D54Y

The initial rationale behind these two mutants was the generation of an aromatic π - π stacking between the two facing phenylalanines or tyrosines. X-ray structural analysis, however, did not confirm this assumption. Instead, both in D54F and in D54Y, the aromatics might rather electrostatically interact, possibly ion-mediated, with facing threonine at position 52 (T52) (see **Figure 6.10**). The almost identical orientation and the high electron density (data not shown) of F/Y54 and T52 support this assumption. According to the distance and the ring coordination, the aromatics do certainly not interact with each other.

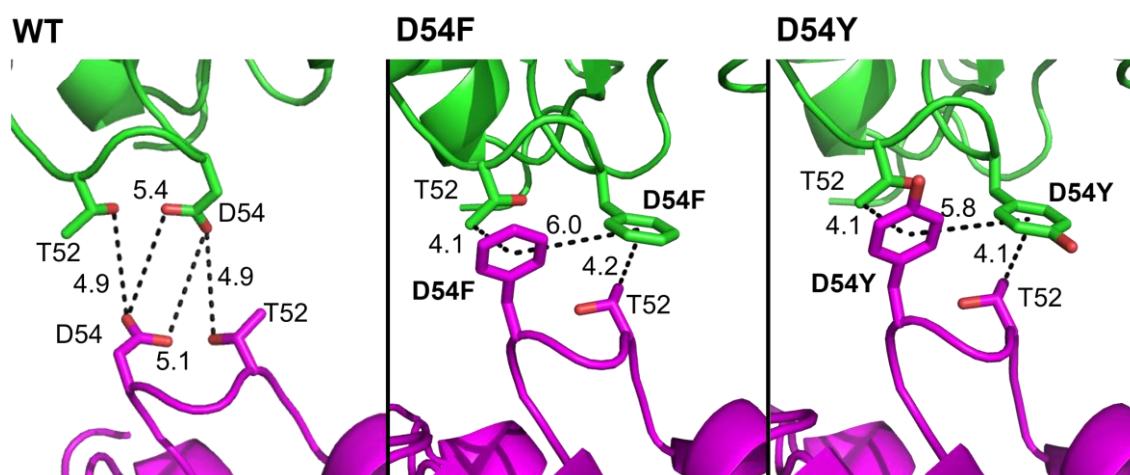


Figure 6.10: Crystallographic image illustrating the crystal contact #2 of *LbADH* WT, D54F, and D54Y. Green and magenta colored cartoon structures are sections of two *LbADH* tetramers interacting in the protein crystal. Distances (in Å) are depicted by the dashed lines. The figure was generated with the PDB IDs 6H07 (WT), 6Y1C (D54F), and a non-published PDB file of D54Y_Q126K (listed in **Table 6.3**; no dataset available for the single mutant D54Y) using PyMOL (v.2.1; Schrödinger).

T102E

The mutation T102E was introduced to investigate whether a salt bridge with the facing lysine (K48) can be generated. WT threonine at position 102 (T102) seems not to play an important role in the crystal contact due to the distance to the opposite monomer (see **Figure 6.11**). In contrast, large glutamic acid residue in the mutant is in proximity (~ 3 Å) to a basic K48 residue, and thus in fact seems that a salt bridge was formed by this engineering approach. Dasgupta *et al.* concluded from a large study on crystal contacts, that the K-E pairing is one of the most favored pairwise contacts – both in oligomer and crystal contacts (Dasgupta *et al.*, 1997). The results of this mutant demonstrate that improved crystallizability is not just about reduction of a protein's solubility (e.g. by introducing hydrophobic amino acids or by shifting the pI), which would be a macroscopic effect. Instead, structural analysis revealed direct enhancement of the attractive interaction at the specific crystal contact.

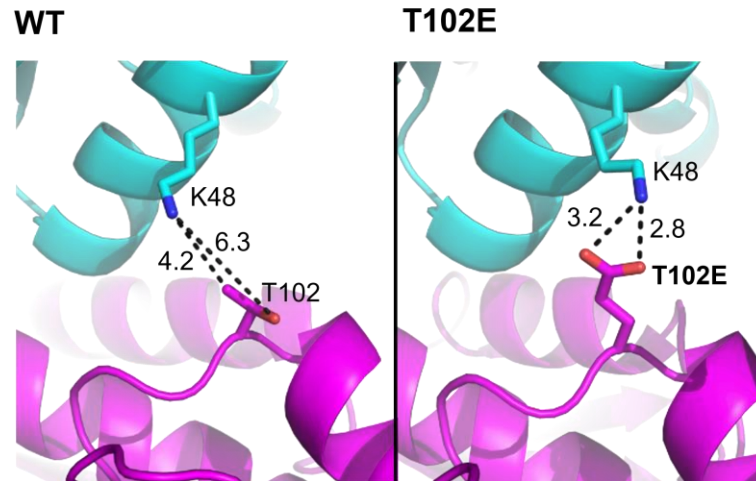


Figure 6.11: Crystallographic image illustrating the crystal contact #1 of *LbADH* WT and T102E. Cyan and magenta colored cartoon structures are sections of two *LbADH* tetramers interacting in the protein crystal. Distances (in Å) are depicted by the dashed lines. The figure was generated with the PDB IDs 6H07 (WT) and 6Y0S (T102E) using PyMOL (v.2.1; Schrödinger).

Q126H and Q126K

For mutants Q126H and Q126K, the rationale also was the formation of a salt bridge between the positively charged, stabilized histidine or lysine at position 126 and the negatively charged aspartic acid (D41) or glutamic acid (E44). In case of Q126H the side chain of E44 indeed has reordered towards H126, possibly forming a long-distance salt bridge. The major interaction, however, is most likely hydrogen bonding between H126 and serine (S40).

Due to the large lysine, introduced in Q126K, E44 gets in proximity (<3 Å), indicating an intermittent salt bridge with E44, which reveals two conformations.

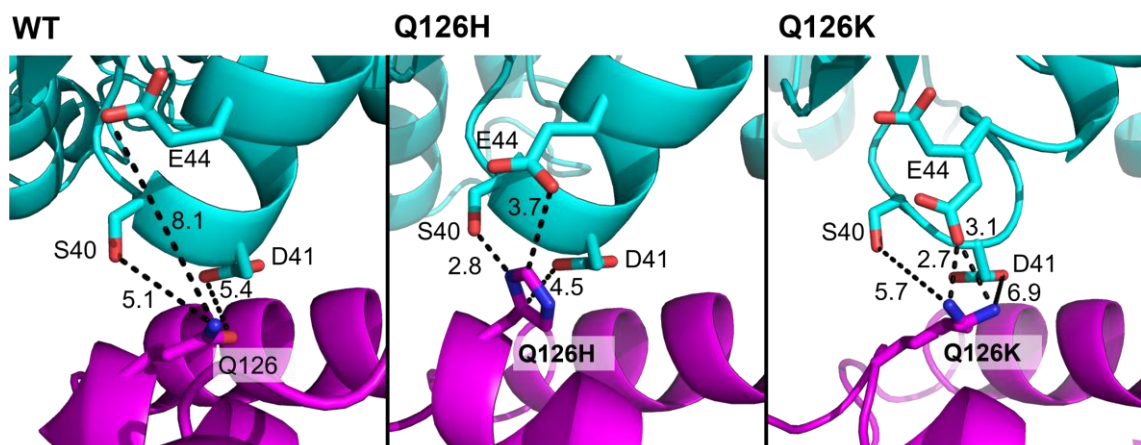


Figure 6.12: Crystallographic image illustrating the crystal contact #1 of *LbADH* WT, Q126H, and Q126K. Cyan and magenta colored cartoon structures are sections of two *LbADH* tetramers interacting in the protein crystal. In Figure Q126K two different conformations of E44 and K126 are illustrated as superposition. Distances (in Å) are depicted by the dashed lines. The figure was generated with the PDB IDs 6H07 (WT), 6Y10 (Q126H), and 6Y0Z (Q126K) using PyMOL (v.2.1; Schrödinger).

Q207Y

Analogous to crystal contact #2 (amino acid position 54), crystal contact #3 is symmetric in a similar way with identical amino acids facing at position 207 (see **Figure 6.13**). In the WT crystal, facing glutamines (Q207) are relatively distant from each other, which suggests only weak, temporary hydrogen bonding. In mutant Q207Y, two conformations of the aromatic residues are present. It can be assumed that the (almost exact) parallel conformations occur simultaneously, which would lead to weak attractive interactions by parallel displaced π - π stacking. Mutation Q207Y did not lead to enhanced crystallizability, nevertheless this is an indication that aromatic π - π stacking can occur at crystal contacts.

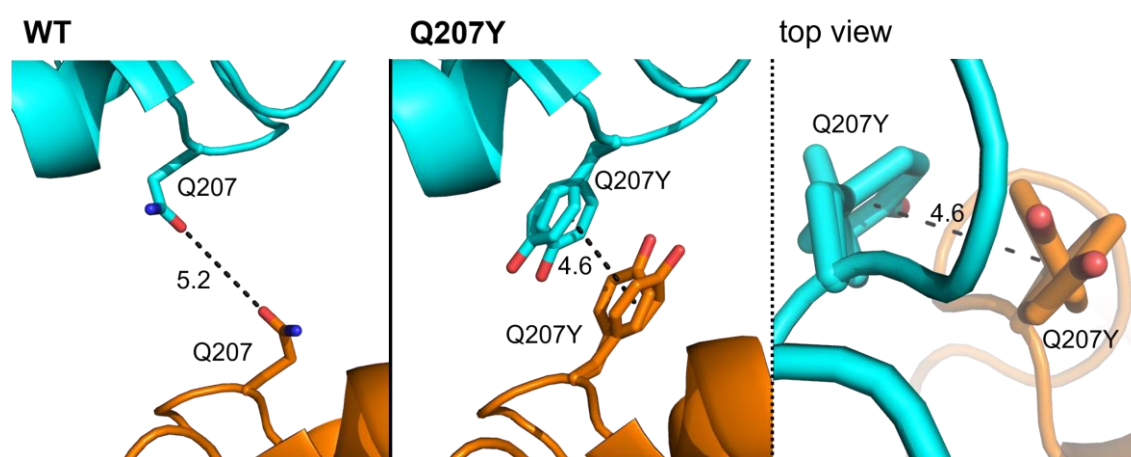


Figure 6.13: Crystallographic image illustrating the crystal contact #3 of *LbADH* WT and Q207Y. Cyan and orange colored cartoon structures are sections of two *LbADH* tetramers interacting in the protein crystal. In the images of mutant Q207Y two different conformations are illustrated at position 207 as superposition. Distances (in Å) are depicted by the dashed lines. The figure was generated with the PDB IDs 6H07 (WT), and an unpublished structure of Q207Y using PyMOL (v.2.1; Schrödinger).

Summarized, these findings demonstrate that newly introduced intermolecular interactions are complex to predict, since in some cases, enhanced attractive forces are not solely the result of the introduction of two but a larger number of interacting residues (e.g. in mutant Q126H). Nevertheless, crystallographic analyses allow assumptions to be made, especially if the crystal contact enhancement can be restricted to two single opposing amino acids (e.g. in mutant T102E). Although entropic effects are generally known to promote protein crystallization more strongly than enthalpic effects, the examples shown here provide evidence for electrostatic enhancement of crystal contacts.

In these exemplary studies with *LbADH*, the greatest effect on protein crystallization was achieved when the amino acid exchange was realized in a loop region (positions 54 and T102). While residues in a α -helix or β -sheet mostly participate within this structure, less interaction takes place within the crystal contact (possibly at position 126 and its possible interaction partners).

6.5 *LbADH* Double Mutants – Investigation of Synergetic Effects

It was investigated whether combinations of two mutations would result in double mutants with enhanced crystallizability compared to the respective single mutants. This was done based on the four best-crystallizing *LbADH* mutants K32A, D54F, T102E, and Q126H. Five double mutants were generated: K32A_T102E, K32A_Q126H, D54F_T102E, D54F_Q126H, and T102E_Q126H. The sixth possible combination K32A_D54F was not considered due to the close proximity and the direct interaction of the amino acids at position 32 and 54, as it was shown above (see **Figure 6.9**). All investigated double mutants revealed enhanced crystallizability compared to the WT. The two double mutants D54F_T102E and T102E_Q126H exhibited enhanced crystallizability compared to both of the respective single mutants, indicating a synergetic effect in these cases (see **Figure 6.14**).

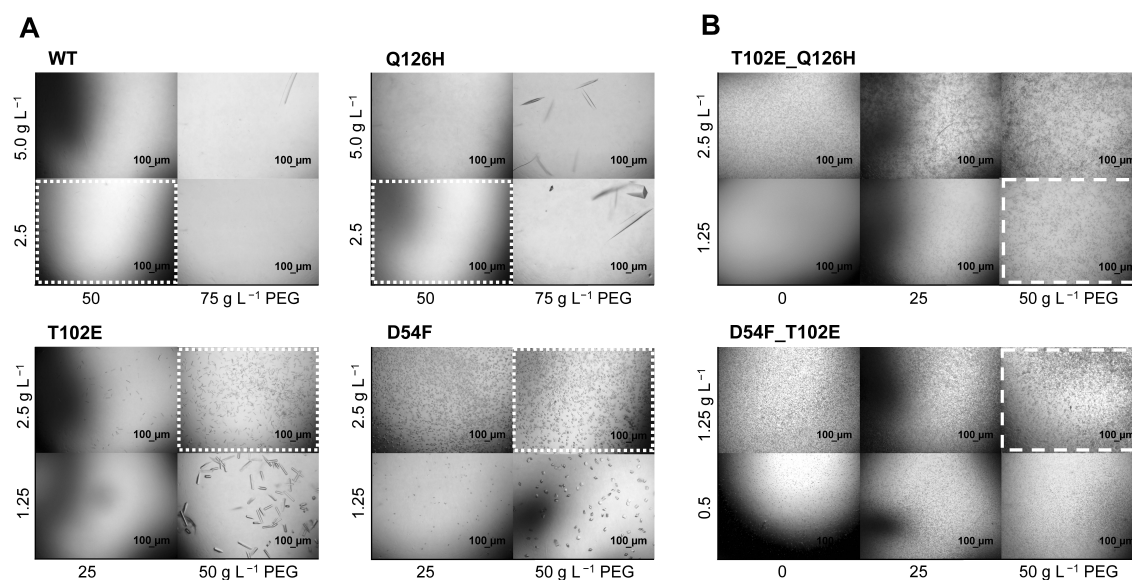


Figure 6.14: Crystallization microphotographs of purified *LbADH* WT together with the three best-crystallizing single mutants (A) and the two best-crystallizing double mutants (B) on the μL -scale. (A) Identical crystallization conditions are illustrated by the dotted white frame. Different protein (vertical axis) and PEG concentrations (horizontal axis) were used to illustrate the minimum concentrations where crystallization occurs. (B) Identical crystallization conditions are illustrated by the dashed white frame. Both double mutants crystallized in absence of crystallization agent PEG. Microphotographs were taken after 24 h.

To validate these first findings, the experimental scope was expanded by generating further double mutants. Additionally, Q126K and D54Y were combined with the single mutants, mentioned above, to generate five additional double mutants: K32A_Q126K, D54F_Q126K, D54Y_Q126H, D54Y_Q126K, and T102E_Q126K. All these five double mutants also exhibited enhanced crystallizability compared to the WT. Three double mutants, D54Y_Q126H, D54Y_Q126K, and T102E_Q126K, revealed enhanced crystallizability compared to both respective single mutants (data not shown).

In summary, synergetic effects were obtained in five out of ten cases, suggesting a general engineering approach, which allows to generate highly crystallizable mutants with a small experimental design space. All single and double mutants which were analyzed by X-ray diffraction, crystallized in the same space group $P2_122_1$ or $I222$, indicating the same crystal packings (see **Table 6.3**). However, the data does not allow for an interpretation of why half of the double mutants did not exhibit a synergetic effect.

Table 6.3: List of all investigated double mutants with and without synergetic effects, which were partly analyzed by X-ray diffraction together with the corresponding space groups, resolutions and PDB IDs.

Variant	Synergetic effect	Space group	Resolution, Å	PDB ID
K32A_T102E	✗	no dataset	–	–
K32A_Q126H	✗	$I222$	1.7	n.p.
D54F_T102E	✓	no dataset	–	–
D54F_Q126H	✗	$P2_122_1$	1.3	n.p.
T102E_Q126H	✓	no dataset	–	–
K32A_Q126K	✗	$P2_122_1$	1.4	6Y1B
D54F_Q126K	✗	no dataset	–	–
D54Y_Q126H	✓	no dataset	–	–
D54Y_Q126K	✓	$P2_122_1$	1.6	n.p.
T102E_Q126K	✓	$I222$	1.8	6Y15

n.p. = not published

6.6 Protein Analysis

6.6.1 Enzymatic Activities

The maximum enzymatic activity of all *LbADH* variants was measured to examine the general influence of single and double surface mutations on it. The maximum enzymatic activities of the mutants were always given in relation to that of the WT, which had been produced, purified, and measured in parallel to maximize comparability. The applied assay conditions enabled fast and reproducible measurements and there was no need for rebuffering (the selected conditions did not aim for the highest achievable enzymatic activities). The maximum relative activity (V_{max}) of *LbADH* WT was 24.9 ± 3.0 U mg^{-1} using 10 mM acetophenone and 0.5 mM NADPH at 25 °C and pH = 7.0 (n = 6 biological replicates; triplicate measurements).

The enzyme activity screening revealed that 19.4% of the mutants presented in the first mutant screening (see 6.3.3), had no or little enzymatic activity (0–10% of the WT's activity). However, most of these enzymatically inactive mutants belong to the 'non-crystallizable' category (meaning no visible crystallization after 24 h at the standard conditions [5 g L^{-1} *LbADH* and 75 g L^{-1} PEG, $20 \text{ }^\circ\text{C}$]) as illustrated in **Figure 6.15**. Hence, enzyme inactivity is a strong indicator for significantly decreased crystallizability of *LbADH* mutants, which is further discussed in the following. The average activity was 56.6% for the non-crystallizable and 75.1% for the crystallizable variants.

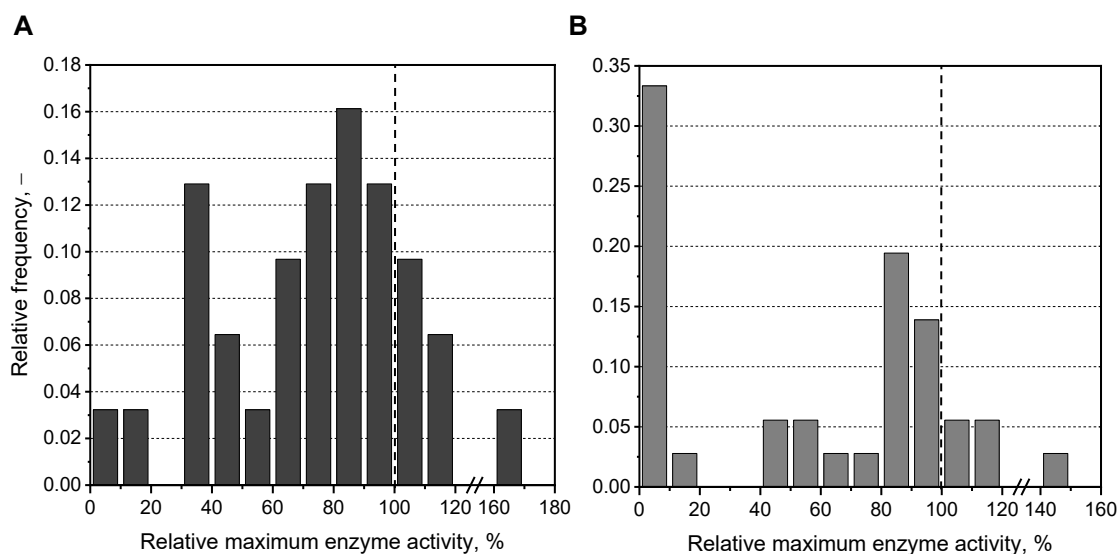


Figure 6.15: Histograms of the relative maximum enzymatic activities of (A) crystallizable and (B) non-crystallizable *LbADH* mutants. Categorization between 'crystallizable' and 'non-crystallizable' was conducted according to the crystallization result after 24 h at the standard conditions (5 g L^{-1} *LbADH* and 75 g L^{-1} PEG, $20 \text{ }^\circ\text{C}$). Enzymatic activities were measured with 10 mM acetophenone, 0.5 mM NADPH, pH 7.0 at $25 \text{ }^\circ\text{C}$. (A) 31 mutants (mean = 75.1%); (B) 36 mutants (mean = 56.6%). Values are listed in Appendix, Table E.1.

Five out of the six best-crystallizing mutants exhibited relative maximum enzymatic activities of $>80\%$ compared to the WT (see Figure 6.16). Reduced concentrations of cofactor NADPH and substrate acetophenone also resulted in catalytic activities comparable to those of WT, indicating no significant effect of the respective amino acid exchanges on the affinity of both molecules.

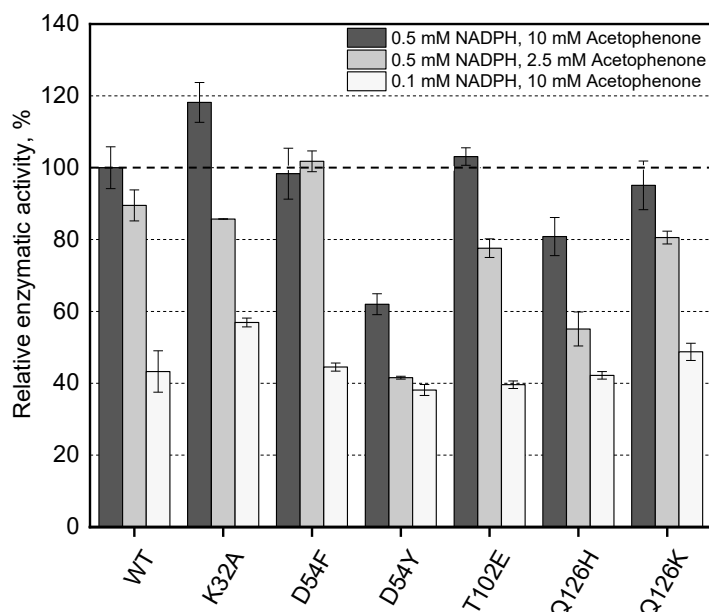


Figure 6.16: Enzymatic activities of *LbADH* WT and six mutants at V_{\max} conditions (left) and reduced acetophenone (center) and NADPH (right) concentrations. All values are depicted in relation to V_{\max} of the WT. Error bars correspond to standard deviations of three biological replicates (each triplicate measurements) except for the measurements with reduced acetophenone concentrations (no biological replicates). V_{\max} of *LbADH* WT is $24.9 \pm 3.0 \text{ U mg}^{-1}$ (10 mM acetophenone, 0.5 mM NADPH; $T = 25 \text{ }^{\circ}\text{C}$; $\text{pH} = 7.0$).

The double mutants revealed maximum enzymatic activities between 70 and 104%, except the two double mutants, which include mutation D54Y (see **Figure 6.17**). Mutation D54Y significantly reduces the maximum enzymatic activities of the single mutant and both double mutants.

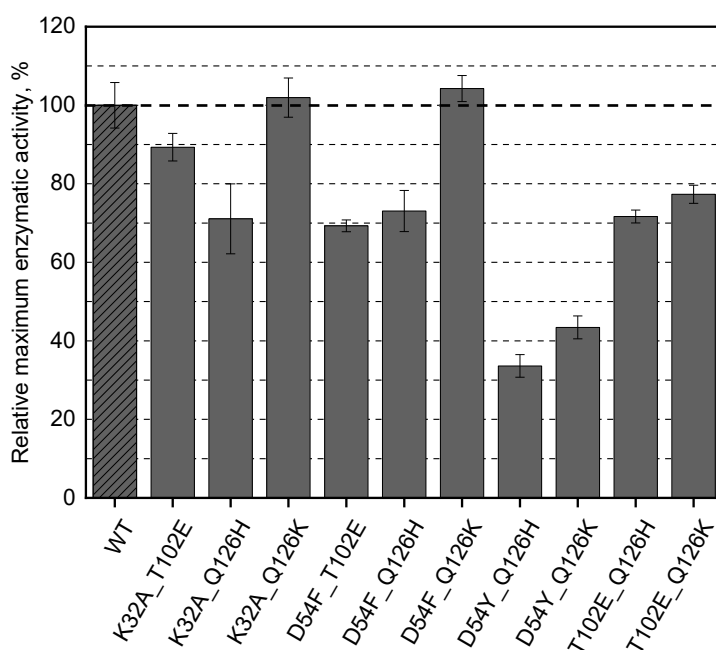


Figure 6.17: Enzymatic activities of *LbADH* WT and ten double mutants at V_{\max} conditions. Error bars correspond to standard deviations of triplicate spectrophotometric measurements. V_{\max} of *LbADH* WT is $24.9 \pm 3.0 \text{ U mg}^{-1}$ (10 mM acetophenone, 0.5 mM NADPH; $T = 25 \text{ }^{\circ}\text{C}$; $\text{pH} = 7.0$).

It could be shown that even single amino acid exchanges at the surface influence the enzymatic activity of *Lb*ADH. Even if interaction chains from the surface to the active center are conceivable, a further explanation for partly strongly reduced activities could be the influence of mutations on the tetrameric structure of *Lb*ADH, which is the only active form of the enzyme. Therefore, *Lb*ADH can be inactivated by altering the active site or by altering oligomerization domains. This assumption is supported by the fact that mainly active mutants crystallized, whereas less active mutants crystallized hardly. An unstable tetrameric structure therefore might negatively influence both enzymatic activity and the crystallizability (if *Lb*ADH monomers do not crystallize, which can be assumed).

6.6.2 Thermal Stability

Thermal Shift Assay (TSA)

Thermal stabilities of *Lb*ADH WT and selected mutants were determined to estimate the influence of surface mutations and to investigate possible correlations to crystallizability of proteins as previously suggested by Dupeux *et al.*, 2011. TSA measurements proved to work reproducibly for *Lb*ADH samples (see **Figure F.1**). The melting temperatures (T_m) of the six best-crystallizing single mutants revealed no correlation to crystallizability: D54F, D54Y, Q126H, and Q126K exhibited a slightly lowered T_m , whereas K32A and T102E exhibited a slightly increased T_m (see **Figure 6.18**). The measurements of randomly selected double mutants (all with enhanced crystallizability compared to the WT) led to similar results.

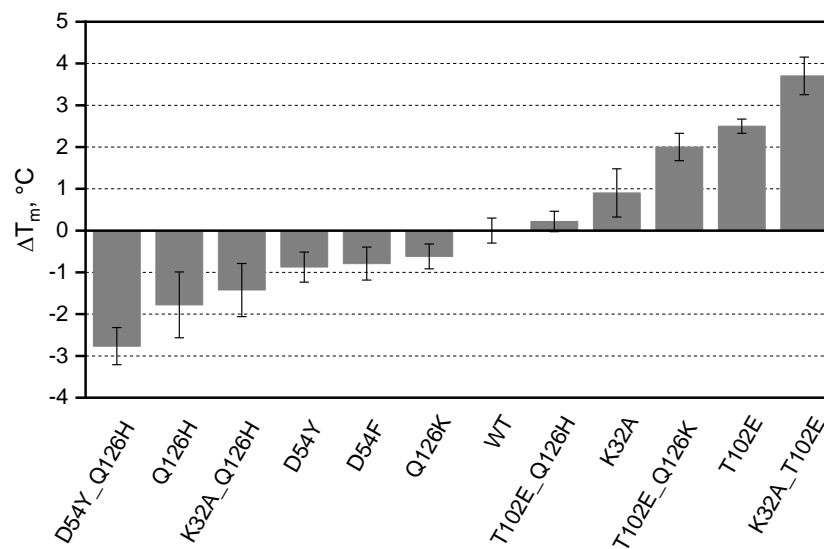


Figure 6.18: Ranked ΔT_m of selected *Lb*ADH mutants compared to the WT (T_m WT = 48.6 ± 0.4 °C). A thermal gradient was applied from 25–95 °C (1 K min^{-1}). SYPRO Orange was used as fluorescent dye ($\lambda_{\text{ex}} 492 \text{ nm} / \lambda_{\text{em}} 568 \text{ nm}$). Triplicate measurements were conducted (biological replicates only for WT ($n = 8$) and T102E [$n = 3$]).

Circular Dichroism (CD) – Thermal Transition Measurements

CD thermal transition measurements verified the effect of amino acid exchanges on T_m . The absolute numbers were considerably lower, but the differences in T_m (ΔT_m) between the WT and the selected mutants K32A and T102E were in a similar range as resulted from TSA measurement. CD and TSA resulted in the same ranking T_m WT < T_m K32A < T_m T102E (see **Figure 6.19 A**). While the WT and T102E only show a small partial unfolding at low temperatures, this is slightly increased in K32A, but especially in the double mutant (see **Figure 6.19 B–D**).

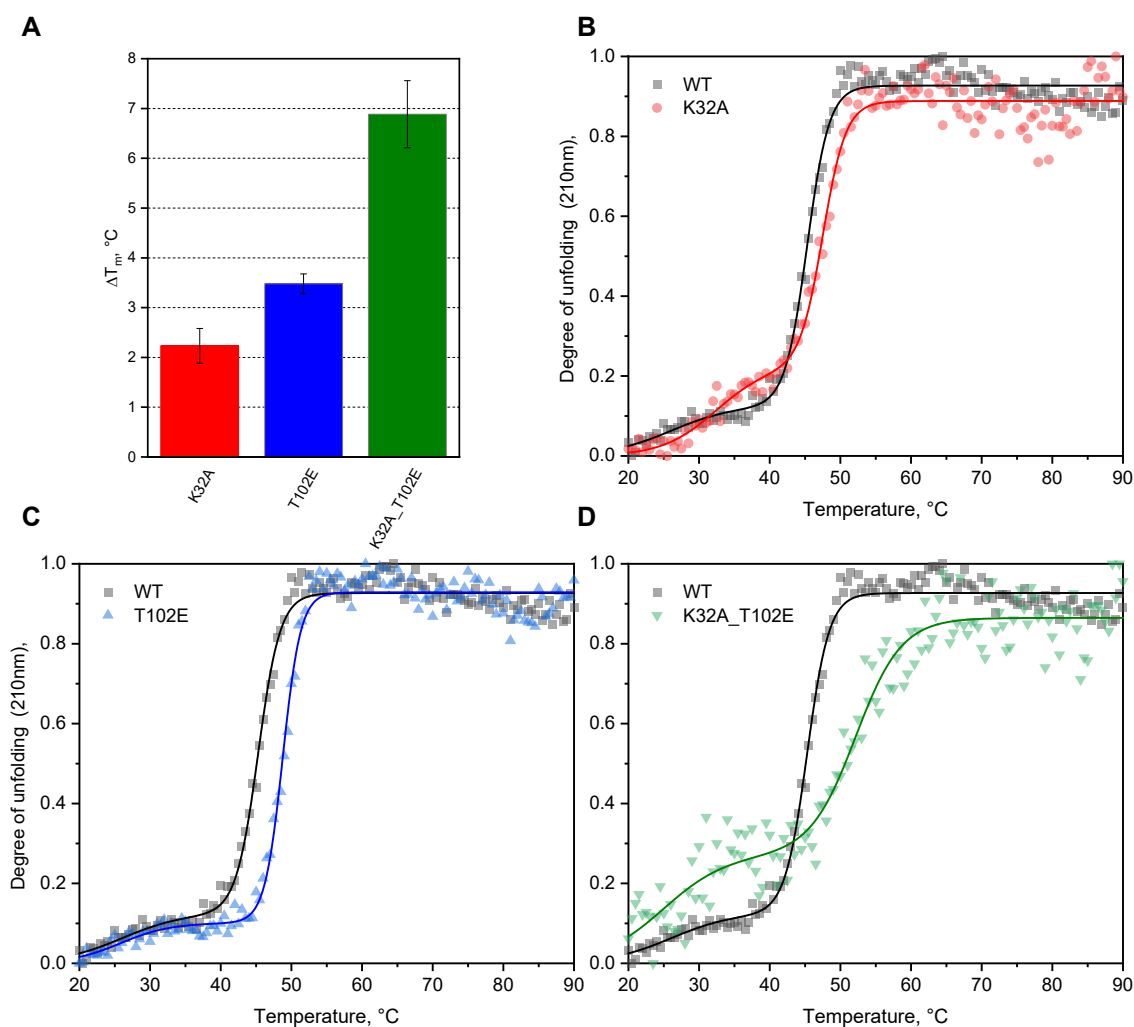


Figure 6.19: Ranked ΔT_m of selected *LbADH* mutants compared to the WT (**A**) and the respective thermal transition graphs of WT in comparison to mutants K32A (**B**), T102E (**C**), and K32A_T102E (**D**) as validated by monitoring the change in ellipticity at a set wavelength of 210 nm. (A) T_m WT: 45.3 °C ± 0.1 °C; T_m K32A: 47.5 °C ± 0.2 °C (ΔT_m : 2.2 °C); T_m T102E: 48.8 °C ± 0.1 °C (ΔT_m : 3.5 °C); T_m K32A_T102E: 52.2 °C ± 0.6 °C (ΔT_m : 6.9 °C); depicted error bars are the sum from the respective mutants' standard deviation plus the WT's standard deviation (B-D) The respective Double Boltzmann fits are indicated by the solid line.

6.6.3 CD Spectra – Secondary Structure Analysis

Exemplary for T102E, K32A, and the double mutant K32A_T102E, the CD spectra of remaining soluble protein fractions after storage at 20 °C for one month were investigated to detect possible differences in the secondary structure composition. The resulting CD spectra revealed no significant differences between the WT and the mutants T102E and K32A, assuming no significant impact of mutation T102E on stability of secondary structures (see Appendix, **Figure F.2**). However, a reduction in secondary structures can be observed for the double mutant K32A_T102E, assuming a decreased conformational stability compared to the tested single mutants.

6.7 Crystallization Across Different Agents and Buffer Systems

In an empiric approach it was investigated whether improved crystallizability of *LbADH* mutants is restricted to the investigated standard crystallization buffer, which contains crystallization agent PEG 550 MME and which is adjusted to pH 7.0. *LbADH* WT and mutant T102E were crystallized in two commercial crystallization screens (MPD and JCSG+ suites, Qiagen, Venlo, Netherlands) to empirically examine crystallizability at randomly chosen buffer conditions. In total, 192 different crystallization buffers were tested with various pH, salts, other crystallization agents, such as 2-Methyl-2,4-pentanediol (MPD), and large PEG molecules up to a molecule size of 8000 kDa. In the MPD-based screen, the amount of WT crystals was higher than that of mutant T102E in only three cases. *LbADH* T102E crystallized with higher amount of crystals in 17 cases, while *LbADH* WT did not crystallize in five cases (see Appendix, **Table G.1**). An even more significant result was obtained applying the JCSG+ screen. The amount of WT crystals was higher than that of mutant T102E in four cases. In contrast, T102E crystallized with higher amount of crystals in 32 cases while WT did not crystallize in 24 cases (see Appendix, **Table G.2**). These findings demonstrated improved crystallizability of *LbADH* T102E across crystallization conditions using buffers with PEG sizes from 300 to 8000 kDa, MPD as PEG substitute and pH ranges from pH 4.0 to pH 8.5. Thus, results of the engineering approach are not limited to the applied standard crystallization buffer.

7 Stirred mL-Crystallization of *Lb*ADH Variants²

Crystallization of selected *Lb*ADH variants was transferred from the static μL -scale (chapter 6) to the stirred mL-scale for the following purposes:

- i. Investigation of the **transferability** of crystallization results from previous static μL -scale to the stirred mL-scale (scale-up approach).
- ii. More detailed characterization of **crystallization kinetics** of the variants by concentration measurements in the supernatant, enabled by larger sample volumes.
- iii. More precise representation of **technical protein crystallization** including the investigation of recrystallization and the effect of impurities on crystallization.

The *Lb*ADH variants applied in these experiments were selected according to the screening results of the μL -scale, which was ongoing simultaneously. Therefore, the set of examined variants was not consistent but changed slightly throughout all experiments.

7.1 Crystallization of Purified Proteins

7.1.1 Reproducibility of Stirred-mL Scale Crystallization

First, the WT was produced and crystallized in purified form at three different days to examine the crystallization kinetics and the reproducibility in the mL-scale. The crystallization kinetics were determined by measuring the residual protein concentration in the soluble phase, assuming that the remaining protein fraction is incorporated into the solid crystal phase. Most crystallization variables, that is, temperature, buffer composition, and protein purity grade, were identical to the μL -scale experiments. The initial protein concentration was raised from 5 to 10 g L^{-1} (20 g L^{-1} in the protein buffer) to increase the difference between the concentration at start and equilibrium of crystallization, and thus to optimize the analytical resolution (assuming that crystallization equilibrium is independent of the initial protein concentration when crystallizing highly purified proteins). Process related differences were a larger working volume (increased from 10 μL to 5 mL) and continuous mixing ($n_{\text{stirrer}} = 150 \text{ min}^{-1}$).

²Results of this chapter are published in Grob et al., 2020.

The crystallization kinetics of the biological WT triplicates were highly similar (see **Figure 7.1**):

- i. Nucleation occurred between 0.75 and 1.25 h. In none of the experiments did nucleation start immediately.
- ii. After 2.5 h a turnover of approximately 80% was observable for all experiments ($79.6\% \pm 1.5\%$).
- iii. After 9 h a turnover of approximately 90% was observable for all experiments ($91.1\% \pm 1.0\%$), indicating a similar crystallization equilibrium.

These findings demonstrate a significantly enhanced reproducibility of crystallization on the stirred mL-scale compared to the static μL -scale, and thus it allows for kinetics comparisons based on absolute instead of relative values.

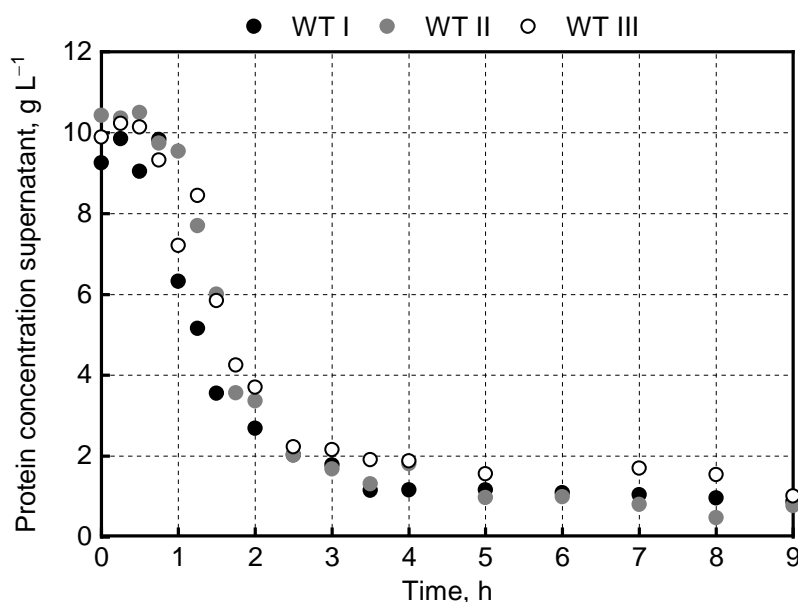


Figure 7.1: Crystallization kinetics of three independently produced and purified *LbADH* WT batches on the stirred mL-scale. Crystallization was conducted in a stirred crystallizer ($V = 5 \text{ mL}$, $n_{\text{stirrer}} = 150 \text{ min}^{-1}$, 10 g L^{-1} *LbADH*, 75 g L^{-1} PEG 550 MME, $T = 20 \text{ }^\circ\text{C}$). The protein concentration in the supernatant was measured by BCA assay (depicted is the mean of triplicate measurements; standard deviations not shown [<0.05]).

7.1.2 Impact of PEG and Protein Concentration on WT Crystallization

Concentrations of purified protein and crystallization agent PEG were varied to study their impact on crystallization kinetics. As already expected from experiments on the μL -scale, a lower PEG concentration led to a delayed nucleation induction phase and a prolonged crystal growth phase (see **Figure 7.2**). Additional information was received on the crystallization equilibrium: the higher the PEG concentration, the lower the protein concentration in the soluble phase in the crystallization equilibrium (compare **Figure 3.8**).

Analogous to previous results on the μL -scale, a high PEG concentration led to a larger number of crystals with smaller crystal sizes.

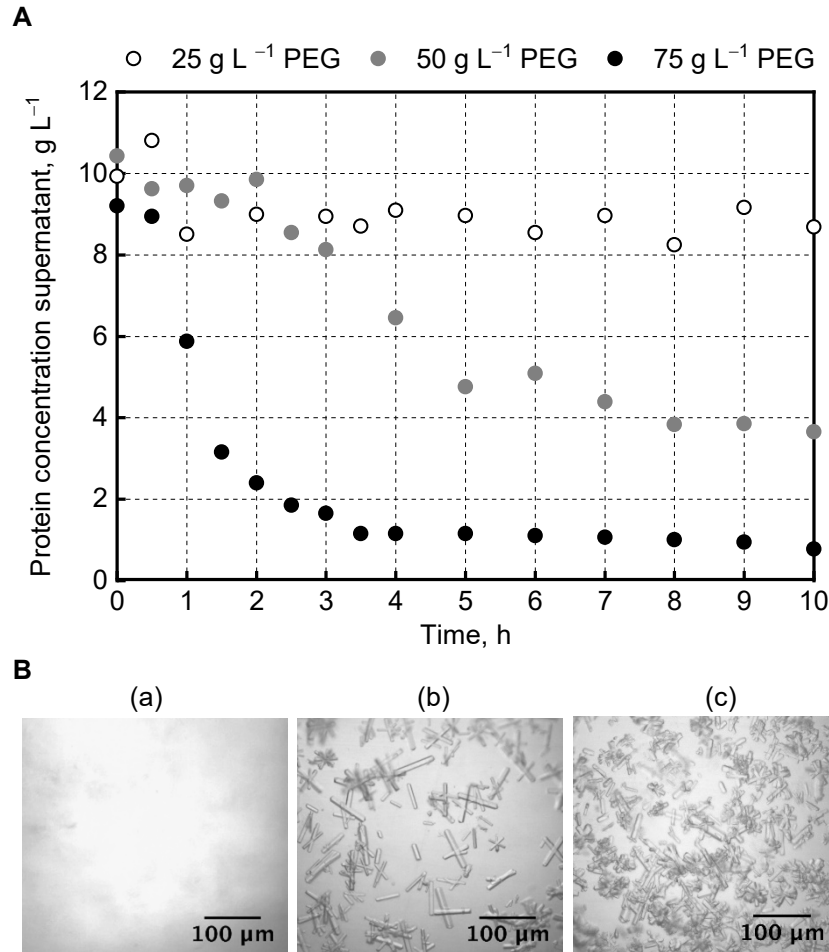


Figure 7.2: (A) Crystallization kinetics and (B) crystal microphotographs of purified *LbADH* WT on the stirred mL-scale applying different protein concentrations. Crystallization was conducted in three stirred crystallizers ($V = 5 \text{ mL}$, $n_{\text{stirrer}} = 150 \text{ min}^{-1}$, 10 g L^{-1} *LbADH* 25–75 g L^{-1} PEG 550 MME, $T = 20 \text{ }^\circ\text{C}$). The protein concentration in the supernatant was measured by BCA assay (depicted is the mean of triplicate measurements; standard deviations not shown [<0.05]). Microphotographs were taken after 10 h from (a) 25 g L^{-1} , (b) 50 g L^{-1} , and (c) 75 g L^{-1} PEG experiments.

The initial protein concentration had a similar effect on crystallization kinetics. A low initial protein concentration led to a delay in nucleation, whereas a higher initial concentration resulted in fast crystallization just from the experimental start (see **Figure 7.3**). This experiment was conducted with a large-scale produced protein batch, which was stored for one year at $4 \text{ }^\circ\text{C}$ before it was applied for this experiment. The ageing of the sample was shown by the increased PEG concentration (125 g L^{-1}) necessary to obtain similarly fast crystallization kinetics as with newly produced protein (75 g L^{-1}). The comparison of these different protein batches is shown in **Figure 7.4**. The use of the old protein batch led to delayed nucleation, slower crystal growth phase and significantly increased crystallization equilibrium. These large deviations between both experiments, and the variations in

equilibrium concentrations in **Figure 7.3** lead to the assumption, that the old protein batch may have contained a significant percentage of soluble, partly unfolded or monomerized *LbADH* molecules, which cannot be incorporated into the protein crystal, and thus remain in the soluble phase. Since this effect leads to false conclusions on crystallization kinetics, all further experiments in this work were conducted with novel produced protein.

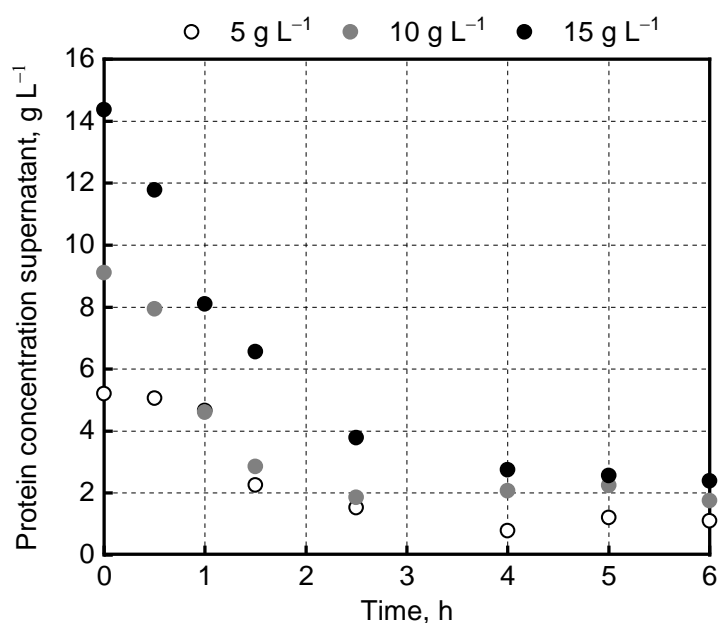


Figure 7.3: Crystallization kinetics of purified *LbADH* WT (different protein batch than used in previous experiments) on the stirred mL-scale applying different protein concentrations. Crystallization was conducted in three stirred crystallizers ($V = 5 \text{ mL}$, $n_{\text{stirrer}} = 150 \text{ min}^{-1}$, $5\text{--}10 \text{ g L}^{-1}$ *LbADH* 125 g L^{-1} PEG 550 MME, $T = 20 \text{ }^\circ\text{C}$). The protein concentration in the supernatant was measured by BCA assay (depicted is the mean of triplicate measurements; standard deviations not shown [<0.05]).

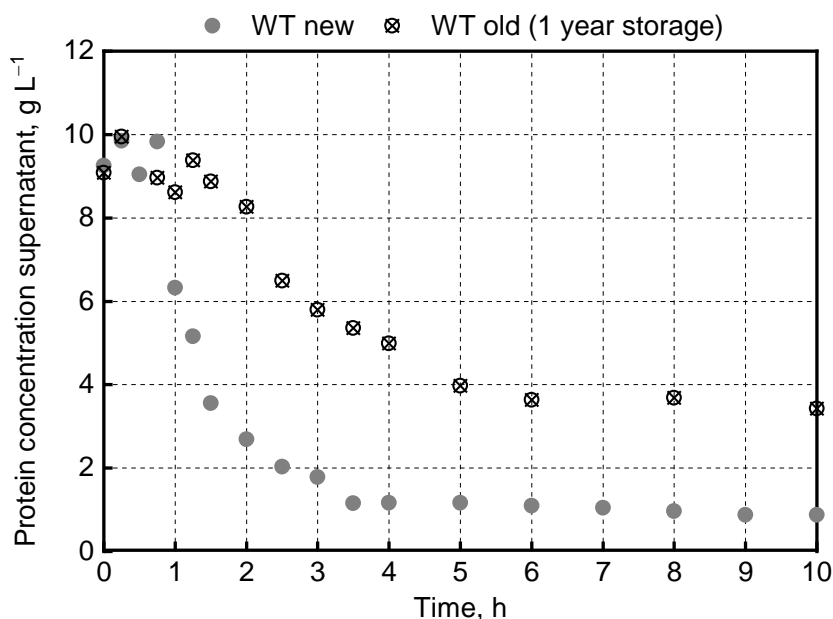


Figure 7.4: Crystallization kinetics of two purified *LbADH* WT samples, stored for two different lengths, on the stirred mL-scale. Protein that was produced and purified immediately before crystallization ('WT new') and protein that was stored 12 months in soluble form at 4 °C before crystallization ('WT old'). Crystallization was conducted in two stirred crystallizers ($V = 5$ mL, $n_{\text{stirrer}} = 150$ min⁻¹, 10 g L⁻¹ *LbADH* 75 g L⁻¹ PEG 550 MME, $T = 20$ °C). The protein concentration in the supernatant was measured by BCA assay (depicted is the mean of triplicate measurements; standard deviations not shown [<0.05]).

7.1.3 Crystallization of *LbADH* Single Mutants

Next, stirred mL-scale crystallization experiments were conducted with the first identified *LbADH* single mutants K32A and Q126K. Also in these experiments, both mutants crystallized with enhanced kinetics compared to the WT, meaning a shorter time until start of nucleation, shorter crystal growth period, and consequently a shorter time until crystallization equilibrium (see **Figure 7.5 A**). While mutant Q126K revealed a short lag phase, K32A started to crystallize immediately. Highly similar crystallization equilibria were reached after 2 h with crystallization yields of >90%, whereas the WT yielded less than 70% after the same period. Similar to results shown in **Figure 7.2**, enhanced crystallization led to smaller crystals (see **Figure 7.5 B**) and a larger amount of crystals (this cannot be deduced from the microphotographs, because they were not uniformly diluted).

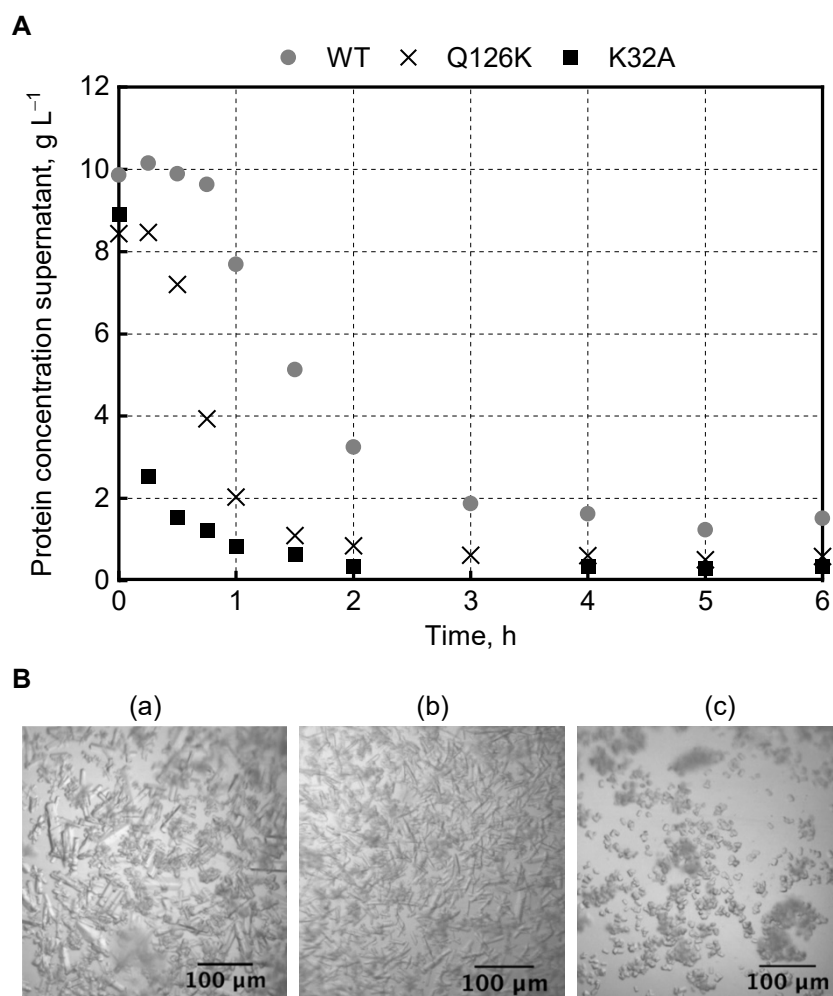


Figure 7.5: (A) Crystallization kinetics and (B) crystal microphotographs of *LbADH* WT and the first two identified mutants with improved crystallization properties on the stirred mL-scale. Crystallization was conducted in two stirred crystallizers ($V = 5 \text{ mL}$, $n_{\text{stirrer}} = 150 \text{ min}^{-1}$, 10 g L^{-1} *LbADH*, 75 g L^{-1} PEG 550 MME, $T = 20 \text{ }^\circ\text{C}$). The protein concentration in the supernatant was measured by BCA assay. Depicted is the mean of biological replicates for WT ($n = 3$), Q126K ($n = 2$), and the mean of triplicate measurements for K32A (no biological replicates). Microphotographs were taken after 24 h. Dark blurred objects are agglomerates of protein crystals, which are located in different focus levels. The amount of crystals is not representative due to different dilution of crystal slurries.

It was confirmed that enhanced crystallization of *LbADH* mutants was scalable from static μL -scale to stirred mL-scale. Crystallization in the stirred mL-scale enabled to analyze crystallization kinetics more accurately and more reproducible than in the static μL -scale. Findings further demonstrate that the influence of a single amino acid exchange can be as positive as the increase of crystallization agent concentration.

7.2 Crystallization from Microbial Cell Lysate

7.2.1 Crystallization Kinetics of Single Mutants

LbADH WT and the four single mutants K32A, Q126H, T102E, and D54F were produced according to the protocol for the crystallization of purified proteins on the μL -scale. No deviations in the recombinant production and in the *LbADH*/HCP ratio were detected, which could have biased crystallization (see **Figure 7.6**).

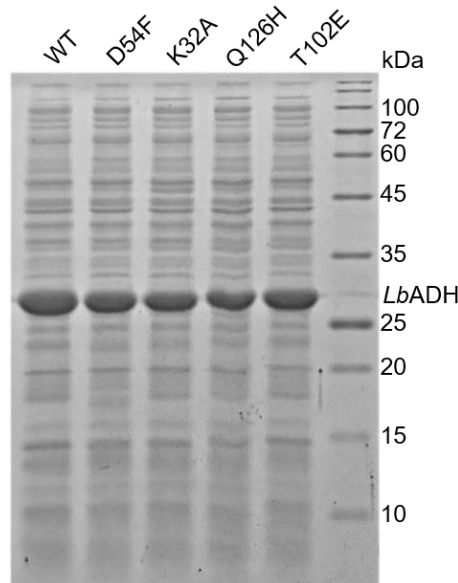


Figure 7.6: SDS-PAGE gel of cell lysates of *E. coli* BL21(DE3) containing *LbADH* WT and the four single mutants K32A, Q126H, T102E, and D54F.

Cell disruption in phosphate-buffered saline (PBS) and subsequent dialysis against protein buffer were also conducted according to all previous experiments with purified proteins on the μL -scale. Affinity chromatography was the only omitted process step to enhance the comparability to previous crystallization results on the μL -scale. The HCP concentration was approximately 50% of the total protein concentration (estimated by SDS-PAGE densitometry; residual part: 50% *LbADH*).

In the stirred crystallizers, all mutants started to crystallize earlier and reached crystallization equilibrium significantly earlier than the WT (meaning faster crystallization kinetics, see **Figure 7.7 A,B**). Crystal morphologies differed significantly from each other (see **Figure 7.7 C**).

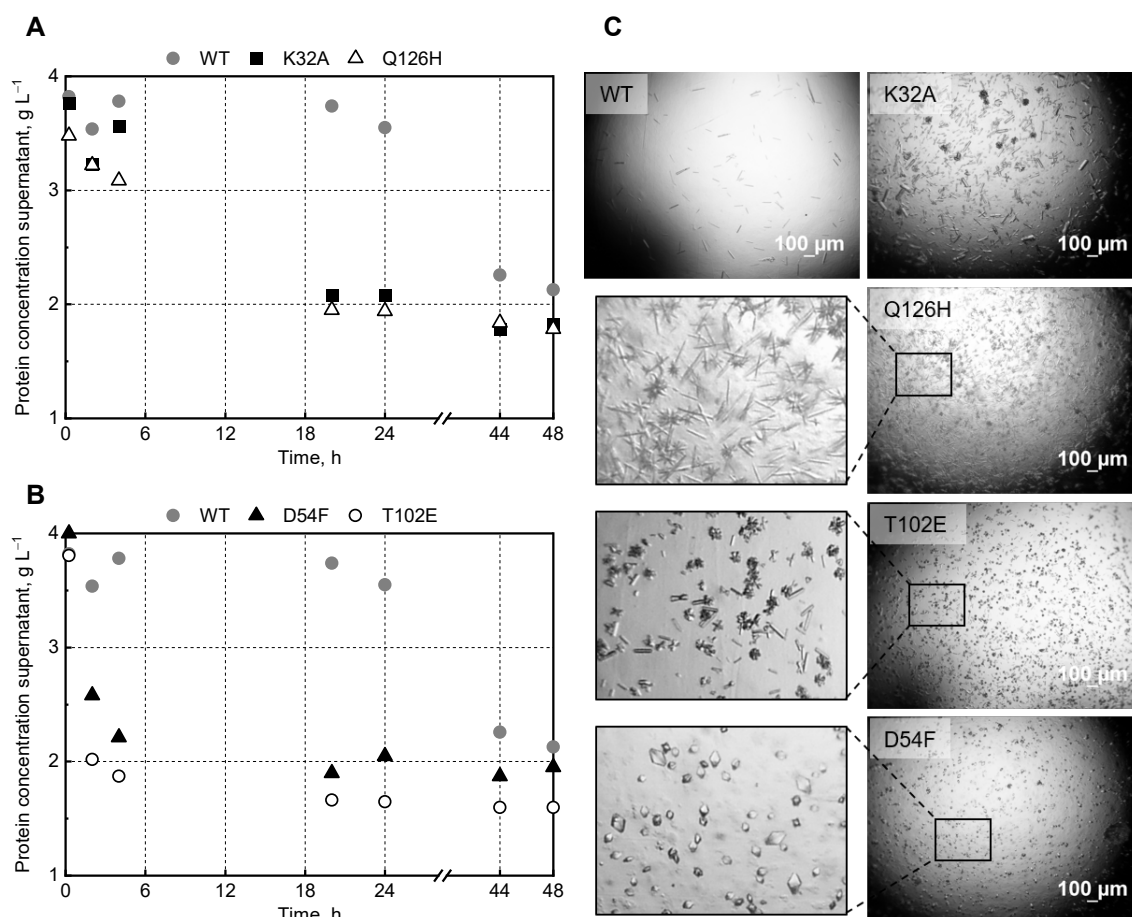


Figure 7.7: (A,B) Crystallization kinetics and (C) crystal microphotographs of *LbADH* WT and four single mutants from dialyzed *E. coli* cell lysate. Crystallization was conducted in five stirred crystallizers ($V = 5$ mL, $n_{\text{stirrer}} = 150$ min⁻¹, 100 g L⁻¹ PEG 550 MME, $T = 20$ °C). The protein concentration in the supernatant was measured by BCA assay. Microphotographs were taken after 24 h. The framed image sections of Q126K, T102E, and D54F are 5-fold magnified.

The crystallization kinetics of the mutants D54F and T102E were significantly faster than those of Q126H and K32A ($T102E \cong D54F > Q126H > K32A > WT$). These results match those of the μL -scale experiments using purified protein, and thus demonstrate the scalability from the static μL - to the stirred mL-scale irrespective of the HCP concentration in the cell lysate.

By reduction of the PEG and total protein concentration by 25% each, WT crystallization was prevented while the single mutants still crystallized. However, the crystallization of single mutants occurred with slower kinetics compared to previous conditions (see **Figure 7.8**, exemplary shown for WT, Q126H, and T102E).

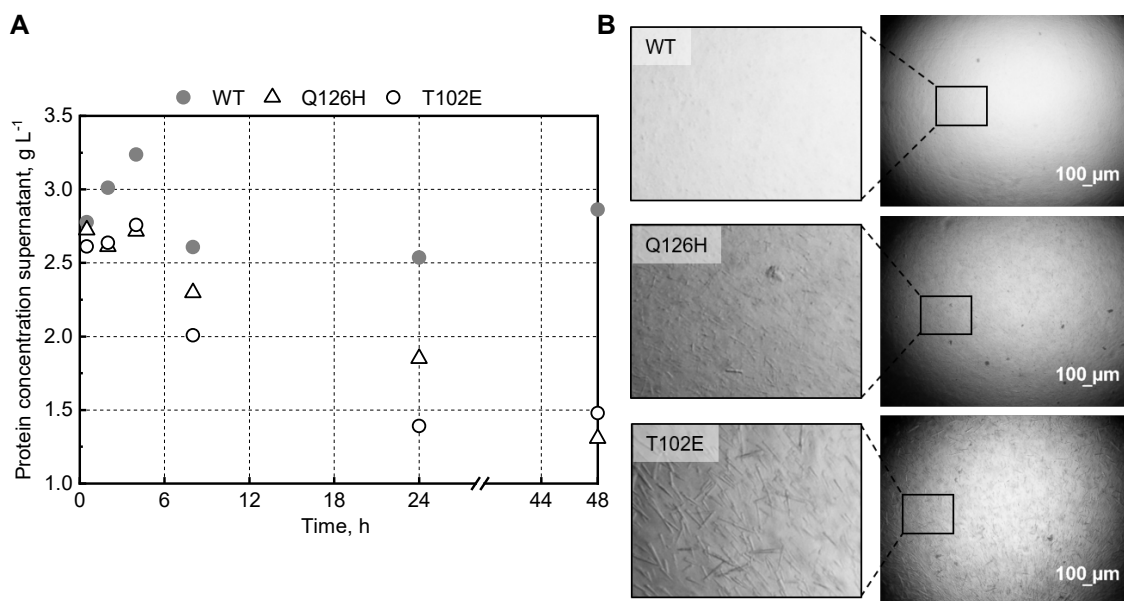


Figure 7.8: (A) Crystallization kinetics and (B) crystal microphotographs of *LbADH* WT and the mutants Q126H and T102E at reduced PEG and total protein concentration. Crystallization was conducted in stirred crystallizers ($V = 5 \text{ mL}$, $n_{\text{stirrer}} = 150 \text{ min}^{-1}$, 75 g L^{-1} PEG 550 MME, $T = 20 \text{ }^{\circ}\text{C}$). The protein concentration in the supernatant was measured by BCA assay. Microphotographs were taken after 48 h. Image sections are 5-fold magnified. Dark roundish objects are agglomerates of protein crystals.

7.2.2 Crystallization Kinetics of Double Mutants

The best-crystallizing *LbADH* double mutants D54F_T102E and T102E_Q126H, identified in the μL -scale screening, were directly crystallized from clarified cell lysate without performing a preceding dialysis step. This represents the most simplified process flow investigated in this work. *LbADH* WT and T102E were crystallized in parallel as references. The WT did not crystallize at this condition. T102E crystallized after a long induction phase of approximately 40 h, which was significantly longer than what was observed in the experiments using the dialyzed lysate, although concentrations of *LbADH* T102E were identical in both experiments (see **Figure 7.9 A**). This observation indicates that a dialysis step has a positive effect on the crystallization kinetics. Most likely, this is due to a decrease in the concentration of small host cell components (e.g. peptides, oligonucleotides), which was not detectable by SDS-PAGE. In contrast to *LbADH* WT and T102E, both double mutants crystallized immediately, which represents the results from the static μL -scale, and thus further demonstrates the scalability from this scale to the stirred mL-scale. The double mutants crystallized in distinct crystal morphologies, similarly to the crystals of the single mutants. *LbADH* D54F_T102E crystallized in a cubic or spherical form similar to single mutant D54F. *LbADH* T102E_Q126H crystallized rod-like with a high aspect ratio, similar to Q126H (see **Figure 7.9 B**).

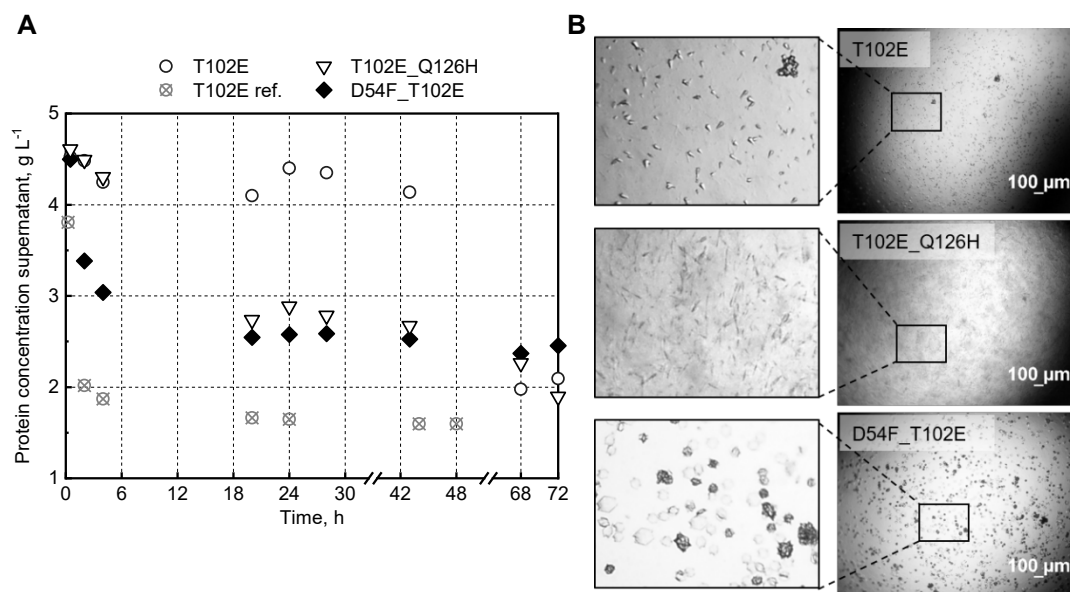


Figure 7.9: (A) Crystallization kinetics from clarified cell lysate and (B) crystal microphotographs of *LbADH* double mutants T102E_Q126H and D54F_T102E, and single mutant T102E as reference. *LbADH* WT did not crystallize under these conditions (data not shown). Crystallization was conducted in stirred crystallizers ($V = 5 \text{ mL}$, $n_{\text{stirrer}} = 150 \text{ min}^{-1}$, 100 g L^{-1} PEG 550 MME, $T = 20 \text{ }^{\circ}\text{C}$). The protein concentration in the supernatant was measured by BCA assay. Microphotographs were taken after 43 h. Image sections are 5-fold magnified. Dark roundish objects are agglomerates of protein crystals. Data of “T102E ref” correspond to *LbADH* T102E crystallization from dialyzed lysate (compare **Figure 7.7**).

7.2.3 Reproducibility of Stirred-mL Crystallization from Lysate

Experiments were repeated exemplary with single mutant T102E and double mutant D54F_T102E from *E. coli* transformation to crystallization to validate reproducibility of the crystallization results from clarified and dialyzed lysate.

The results were highly comparable to previous crystallization results (see **Figure 7.10**, compare to **Figure 7.7** and **Figure 7.9**). Even the long nucleation induction phase of clarified T102E before reaching the same crystallization equilibrium was reproducible. Crystallization start of dialyzed T102E was slightly delayed compared to the previous run, but crystallization equilibrium was reached within 20 h, which was again significantly faster than crystallization from clarified lysate. Crystallization kinetics of D54F_T102E from clarified cell lysate were highly similar to the previous run. The additional crystallization of D54F_T102E from clarified lysate underlined the accelerated kinetics caused by the dialysis step.

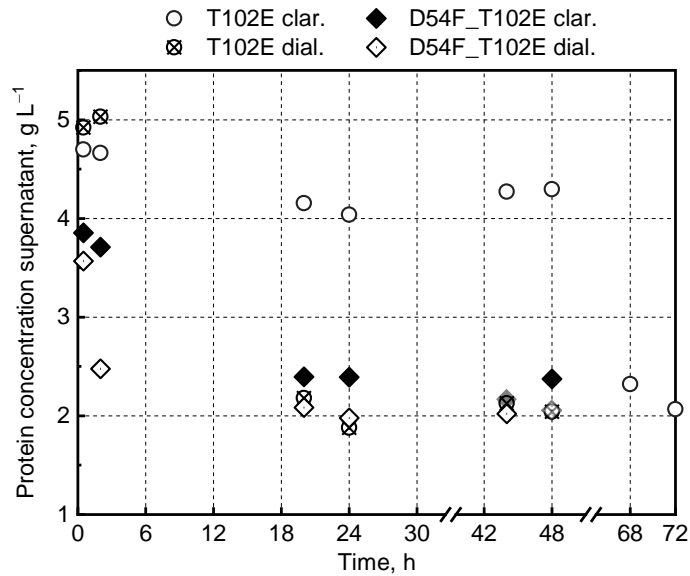


Figure 7.10: Reproduced crystallization kinetics of *Lb*ADH T102E and D54F_T102E from clarified (clar.) and dialyzed (dial.) cell lysate. Crystallization was conducted in stirred crystallizers ($V = 5$ mL, $n_{\text{stirrer}} = 150$ min⁻¹, 100 g L⁻¹ PEG 550 MME, $T = 20$ °C). The protein concentration in the supernatant was measured by BCA assay.

Besides the crystallization kinetics, the crystal morphologies were also comparable to previous runs (see **Figure 7.11**). Compared to previous standard microscopic equipment, these microphotographs were taken using a camera enabling higher image quality (Nikon DS-Fi3 microscope camera). These microphotographs illustrate that uniform crystal morphologies were achieved even in the presence of high concentrations of host cell components.

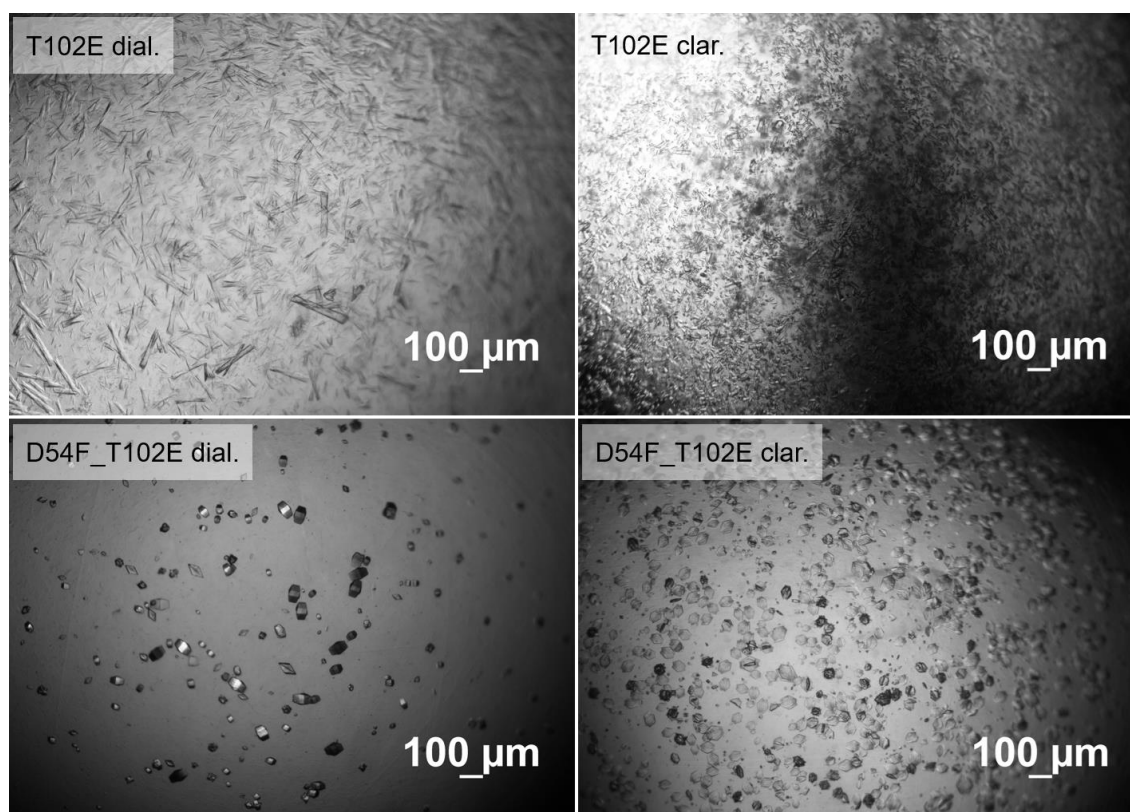


Figure 7.11: Crystal microphotographs of *LbADH* T102E and D54F_T102E from clarified (clar.) and dialyzed (dial.) cell lysate. Microphotographs were taken after 48 h, except for T102E from clarified lysate (72 h). Images were exclusively taken with a high-resolution DS-Fi3 microscope camera.

7.2.4 Crystal Dissolution and Recrystallization

To obtain purified protein in soluble form, protein crystals needed to be separated from the supernatant, washed, and dissolved. Aiming for a further purification step, a subsequent, second crystallization step – the recrystallization – was examined.

In a buffer screening (see 4.5.3), protein buffer supplemented with 1 M MgCl_2 was found to be suitable for quick crystal dissolution without the generation of protein aggregation.

The experiments were conducted with crystals of *LbADH* WT and the four single mutants K32A, D54F, Q126H, and T102E. Crystal slurries were centrifuged to separate the crystals from the soluble phase. Subsequently, the crystals were resuspended in protein buffer for crystal washing. Enzymatic activity assays confirmed that there was no crystal dissolution during this process. *LbADH* WT, K32A, Q126H, and T102E crystals dissolved within a few seconds, using protein buffer with a high MgCl_2 concentration (20 mM HEPES-NaOH pH 7.0, 1 M MgCl_2). Lower MgCl_2 concentrations dissolved the crystals much slower. D54F crystals were only partially dissolving in this buffer. After dialysis and concentration of the samples, recrystallization was successfully conducted in the stirred mL-crystallizers. The ranking of crystallization kinetics of *LbADH* variants were identical to those of the stirred mL-scale experiments ($\text{T102E} \cong [\text{D54F}] > \text{Q126H} > \text{K32A} > \text{WT}$) despite varying initial

conditions (lower *LbADH* and HCP concentrations). D54F must be regarded separately due to its significantly lower initial concentration of below 1 g L^{-1} because of its aforementioned partial crystal dissolution; however, it was shown that crystallization of this mutant occurred (see **Figure 7.12 B**). Specific enzymatic activities were not affected by crystallization and crystal dissolution (data not shown).

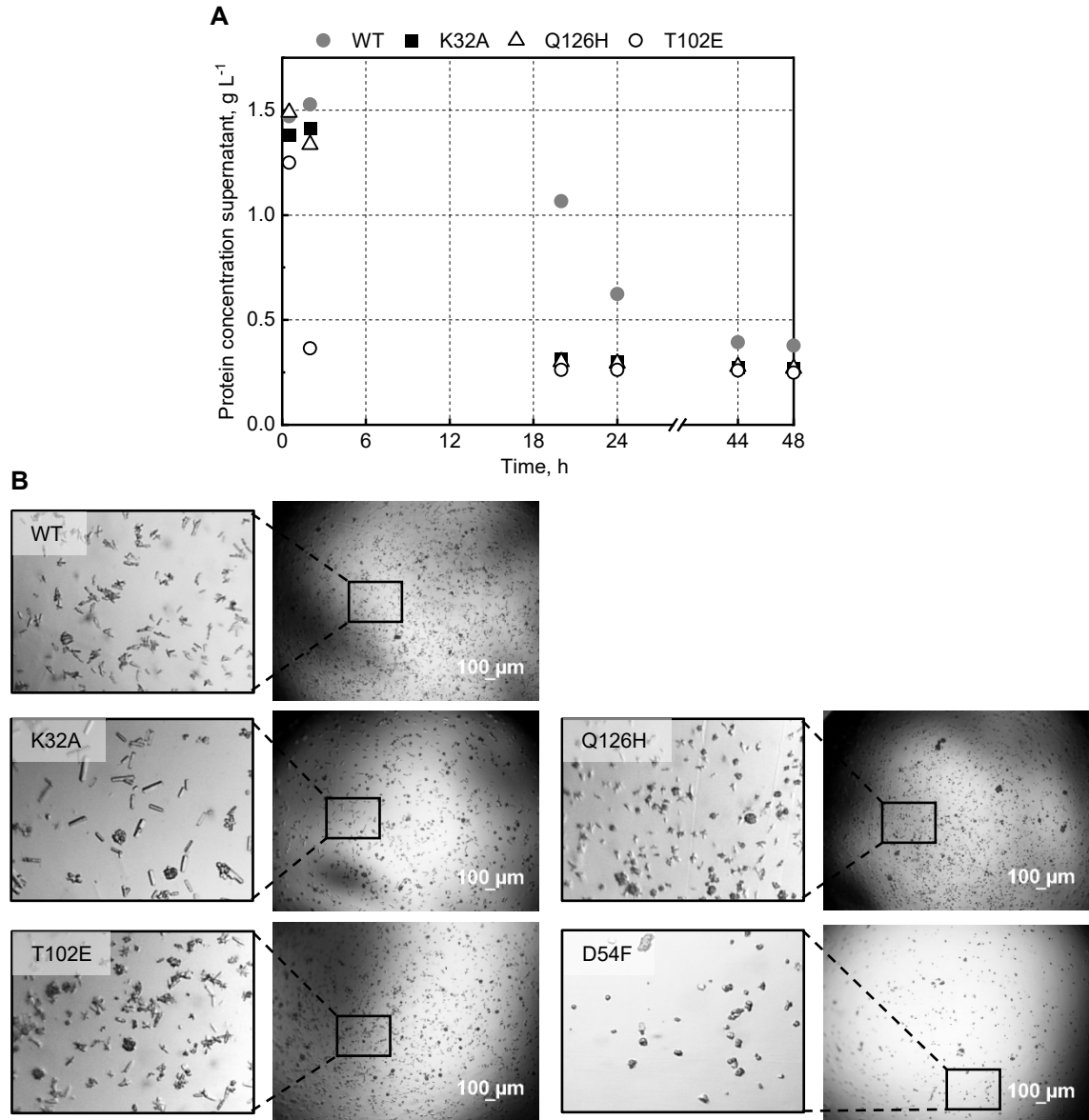


Figure 7.12: (A) Recrystallization kinetics and (B) crystal microphotographs of *LbADH* WT and the single mutants K32A, Q126H, and T102E after crystal washing and dissolution. No kinetics are shown for mutant D54F due to its significantly lower ability to dissolve in the dissolution buffer, leading to a lower initial concentration. Crystallization was conducted in five stirred crystallizers ($V = 5 \text{ mL}$, $n_{\text{stirrer}} = 150 \text{ min}^{-1}$, 100 g L^{-1} PEG 550 MME, $T = 20 \text{ }^{\circ}\text{C}$). The protein concentration in the supernatant was measured by BCA assay.

7.2.5 Purification Effect and Yield of Crystallization and Recrystallization

The general purification effect of protein crystallization has been described in several studies, as discussed before. However, only very few successfully demonstrated the chromatography-free purification by crystallization from impure solutions, such as microbial lysate. Most experiments were conducted with prepurified cell harvest. The following investigations were undertaken to demonstrate the purification effect by crystallization of *LbADH* variant T102E, and thus to prove the overall application success of this work.

Both dialyzed and clarified cell lysate contained approximately 50% HCP (estimated by SDS-PAGE densitometry). Washed and dissolved *LbADH* crystals from experiments with dialyzed lysate contained $3.0\% \pm 0.1\%$ HCP (analyzed by HCP-ELISA), which corresponds to a more than 10-fold HCP reduction compared to the initial dialyzed lysate. Washed and dissolved crystals after recrystallization contained only $0.3\% \pm 0.1\%$ HCP, corresponding to an additional 10-fold reduction of HCP compared to the first crystallization step (in total, a 100-fold HCP reduction). Experiments with clarified lysate showed a similar reduction in HCP. Washed and dissolved crystals contained $8.1\% \pm 0.6\%$ HCP after the first crystallization and $0.2\% \pm 0.1\%$ after the recrystallization. The high purity of dissolved crystals was illustrated by SDS-PAGE analysis (see **Figure 7.13**). The bands with a size of ~56 kDa correspond to dimerization bands that had been detected at the same intensity in all IMAC-purified samples (compare **Figure 6.5**).

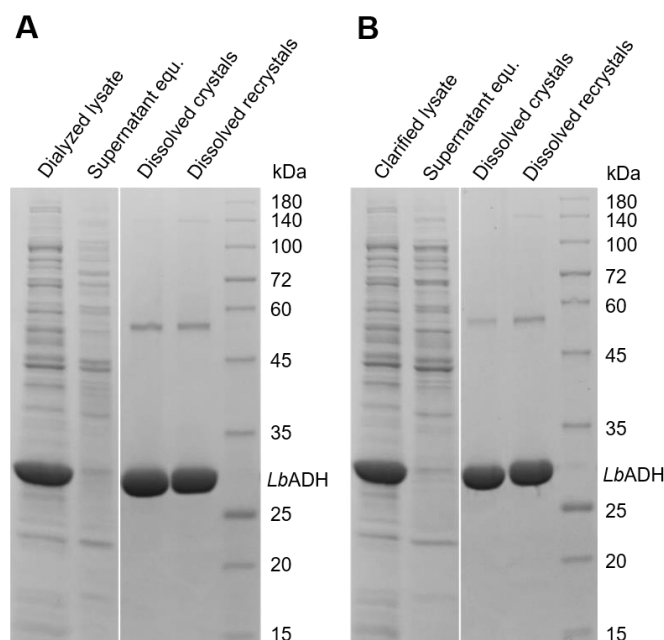


Figure 7.13: SDS-PAGE visualizing the crystallization yield and the purity effect of crystallization and recrystallization. **(A)** Crystallization of *LbADH* T102E from dialyzed lysate. **(B)** Crystallization of *LbADH* T102E from clarified lysate. Samples ‘Supernatant equ.’ correspond to the supernatant in crystallization equilibrium. Bands with a size of ~56 kDa in the purified samples correspond to dimerized *LbADH* monomers.

At crystallization equilibrium, almost a complete depletion of *Lb*ADH in the soluble phase was observed resulting in a high crystallization yield of >95%, both from dialyzed and clarified lysate (measured by enzymatic activity assay; visualized by SDS-PAGE, see **Figure 7.13**). No significant changes in crystallization yield were observed among the *Lb*ADH variants and recrystallization yields were >97%. The total yield was >90% assuming that there are no losses during washing (verified by detecting no enzymatic activity of the washing supernatant), no losses during dissolving (complete dissolution was observed; no aggregated/insoluble protein remains; no loss in specific enzymatic activity, verified by activity assays before crystallization and after crystallization + crystal dissolution), and no losses during buffer exchange and concentration. These results highlight the application advantages of technical protein crystallization, enabled by crystal contact engineering: high product purities, high product yields, and minimal need for process technology.

8 Conclusion

Technical protein crystallization may become a cheap, selective, and efficient downstream processing (DSP) method for the purification and formulation of recombinant proteins. It is developing towards an alternative to conventional preparative chromatography in distinct cases, since it addresses its bottlenecks (e.g. complex scale-up, expensive consumables). Moreover, crystalline formulations are advantageous over soluble or precipitated proteins as the densely packed crystal structure prolongs shelf-life and allows for high-concentration subcutaneous drug delivery in therapeutic applications. Nevertheless, the major limitation of technical crystallization is insufficient crystallizability of many proteins, despite huge screening efforts for suitable crystallization conditions. This drawback has been tackled in rare cases by changing the amino acid sequence of a protein to improve its crystallizability for crystallographic purposes. All these semi-rational studies focused on the production of a single large protein crystal exhibiting high X-ray diffraction quality. In the present work, rational protein engineering was approached to improve crystallization of the industrial biocatalyst *Lactobacillus brevis* alcohol dehydrogenase (*LbADH*) more prone to technical crystallization. The aim was to enable faster crystallization while preserving the enzyme's catalytic functionality. Based on the three-dimensional protein structure, *LbADH* mutants with enhanced crystal contact interactions should be generated by site-directed amino acid exchanges at the crystal contact patches. On the μL -scale, a suitable screening should be implemented that allows to identify *LbADH* mutants with improved crystallization ability for technical crystallization purposes. Screening parameters had to be defined which describe such an improved crystallization behavior of *LbADH* mutants in comparison to the non-modified wild-type (WT) protein. An application-oriented focus should be on the investigation of process-related crystallization characteristics, such as the investigation of enhanced crystallization on a larger scale and from solutions with differing degrees of *LbADH* purity. On the atomistic scale, the focus should be on the mutant's engineered crystal contacts to elucidate new enhanced crystal contact interactions by crystallographic methods, and to derive rational engineering strategies thereof. To the best of the author's knowledge, no engineering approach towards enhanced crystallization kinetics for DSP purposes had ever been reported in the literature.

First, it was verified that observed changes in crystallization characteristics (e.g. in kinetics or morphology) of *LbADH* mutants on the static μL -scale can be traced back to single amino acid exchanges. This demonstration was fundamental for the mutant screening since

crystallization is influenced by a high number of handling-, environmental-, and sample-dependent factors, and therefore often referred to as hardly reproducible. Handling related variations were limited by reducing process steps from gene to crystal. Parallel processing of mutants to compare ensured that the environmental conditions (e.g. temperature, humidity) had an equal effect on all mutants. Additionally, *LbADH* WT was produced, purified and crystallized in parallel for reference in each experimental setup. Sample-dependent crystallization factors of all *LbADH* variants were aligned and verified, such as protein concentration and protein purity (>99%). It was shown that the implemented workflow from gene to crystal allowed for the identification of single and double mutants with altered crystallization behavior.

The semi-rational surface entropy reduction (*SER*) strategy by Derewenda and co-workers, proposed for crystallographic purposes, is the only crystal engineering strategy that has been published (Derewenda *et al.*, 2004). The authors claim that protein crystallization is mainly driven by entropic effects and proposed a semi-rational engineering strategy, namely Lys/Glu→Ala exchanges at the protein surface. In the present work, all amino acid exchanges according to the *SER* strategy were focused on selected positions at the existing crystal contact patches of *LbADH* WT, which were localized based on an own high-resolution X-ray structure (PDB ID 6H07). It was not intended to generate new crystal contacts, and thus to randomly reorient them, but to enhance the existing ones. In addition to the *SER* strategy, charged amino acids were introduced at the crystal contact patches. It was intended to explore whether novel attractive electrostatic interactions (enthalpic part of the Gibbs free energy [ΔG]), such as salt bridges, hydrogen bonding, or aromatic π -stacking can also strengthen the crystal contacts, and thus enhance crystallizability. The term ‘enhanced crystallizability’ was defined by the following correlating observations, which were made during mutant screening on the μL -scale: shorter time until first crystals are visible (shorter nucleation induction time), higher number of crystals (higher nucleation rate), shorter crystallization time between nucleation and crystallization equilibrium, and nucleation at reduced concentrations of protein and crystallization agent.

Seven single mutants were identified, which revealed significantly enhanced crystallizability out of a screening of 78 single and double mutants. A higher number of mutants with enhanced crystallizability were generated by introducing charged amino acids at the crystal contact patches (e.g. T102E, Q126H) than by introducing alanine (only K32A). X-ray crystallographic measurements validated the rationality of the applied engineering approach. They revealed that the crystal packing of all mutants was identical to that of the WT in all tested cases, which means that crystal contacts of mutants did not reorient randomly upon mutagenesis. X-ray crystallography further confirmed the assumption that

newly created salt bridges (e.g. in T102E, see **Figure 8.1 A**) or hydrogen bonds (e.g. in Q126H) are the reason for enhanced crystallizability. From these findings, it can be claimed that protein crystallization is not just mainly entropy-driven but can also be controlled by modifying enthalpic effects. As a consequence, it can be strongly assumed that the introduction of charged amino acids opposite of oppositely charged amino acids can generally form attractive salt bridges at crystal contact, which consequently might be considered as a new rational crystal engineering strategy.

It was further investigated whether combinations of two amino acid exchanges, which have a positive effect on crystallization, would result in double mutants with enhanced crystallizability compared to the respective single mutants. All double mutants crystallized faster than the WT and with the same crystal packing. In fact, five out of ten double mutants crystallized faster than the respective single mutants, demonstrating synergetic effects in these cases. The best-crystallizing double mutants T102E_Q126H and D54F_T102E resulted from the three best-crystallizing single mutants (D54F, T102E, and Q126H). The combinatorial approach presented might represent a possible second rational engineering strategy.

The maximum activities of the four best-crystallizing single mutants averaged 100.1% of the WT's activity. Reduced concentrations of cofactor NADPH and substrate acetophenone also resulted in catalytic activities comparable to those of WT, demonstrating that the well-crystallizing variants were not significantly influenced by the single amino acids exchanges. Moreover, five of the six best-crystallizing single mutants did not reveal significant differences in secondary/tertiary structures and thermal stability, concluding that surface mutations did not lead to negative side-effects. The ten double mutants, however, revealed slightly lower average enzymatic activities than the respective single mutants. With mutant T102E, an *Lb*ADH variant was identified which did not reveal any negative effect on the tested parameters (enzyme activity see **Figure 8.1 B**).

It was exemplarily demonstrated that improved crystallizability, and thus the formation of enhanced, redesigned crystal contact interactions, is not limited to the applied crystallization agent PEG 550 MME (polyethylene glycol monomethyl ether, 550 kDa) and the applied pH of 7.0. In an empiric μ L-scale screening applying 192 different crystallization buffers, mutant T102E crystallizes significantly better than the WT, also by applying MPD (2-Methyl-2,4-pentanediol) as crystallization agent or by applying various pH. On the industrial scale, this could offer greater flexibility in changing process variables in integrated crystallization processes.

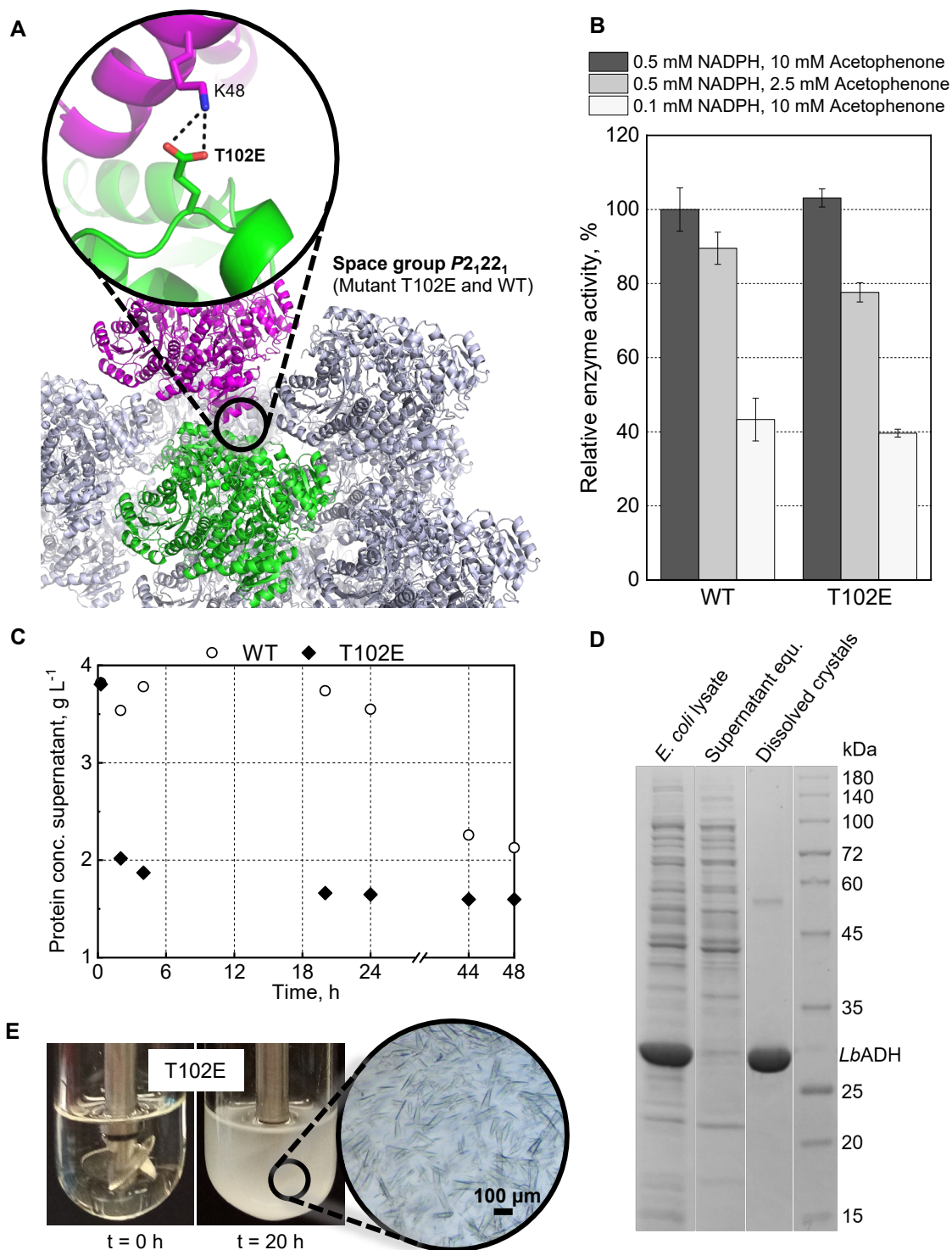


Figure 8.1: Summary of the results of crystal contact engineering of *LbADH* mutant T102E. **(A)** A site-directed single amino acid exchange (T102E) led to the formation of a new salt bridge at the crystal contact. The crystal packing was not influenced (both WT and mutant T102E crystallize in space group $P2_122_1$). **(B)** Enzyme activities of mutant T102E were preserved at non-limiting conditions (dark grey bars; maximum activity at highest concentrations of cofactor NADPH and substrate acetophenone) and at limiting conditions (reduced substrate and cofactor conditions; light grey and white bars, respectively). **(C)** Significantly enhanced crystallization kinetics of mutant T102E compared to the WT at equal conditions from dialyzed *E. coli* lysate in stirred 5-mL-crystallizers. **(D)** Images of crystallization of mutant T102E from dialyzed *E. coli* lysate in stirred 5-mL-crystallizers (inner diameter: 22 mm) and a microphotograph of the crystal slurry in crystallization equilibrium. **(E)** SDS-PAGE illustrating the high selectivity and yield (compare first and second line; crude *E. coli* lysate and supernatant in crystallization equilibrium respectively), and the high purity of dissolved crystals (bands with a size of ~56 kDa correspond to dimerized *LbADH* monomers).

To investigate crystallization kinetics in more detail, the best-crystallizing single and double mutants from the μL -scale screening were crystallized from impure *E. coli* lysate (50% host cell protein, HCP) on the stirred mL-scale (see **Figure 8.1 C,D**). While the WT did only crystallize slowly, all mutants crystallized significantly faster. The order of crystallization kinetics was identical to the experiments on the μL -scale applying purified protein, demonstrating the scalability from the static μL - to the stirred mL-scale, irrespective of the HCP concentration in the cell lysate. These results are an important step towards industrial-scale applicability since it had previously been shown that a further crystallization scale-up from the investigated stirred mL-scale to a stirred L-scale is feasible using the parameter of maximum local energy dissipation (Smejkal *et al.*, 2013a). These findings on crystallization scale-up additionally show that the applied high-throughput screening on the μL -scale is an adequate way to identify and select mutants with altered crystallizability (rather qualitatively; allows to validate if a mutant reveals enhanced or reduced crystallizability in relation to the WT, e.g. by the observation of the number of crystals after a defined crystallization time). Subsequent crystallization on the stirred mL-scale is an adequate way to examine reproducible data on crystallization kinetics (quantitatively; allows for comparing/ranking absolute values of a set of protein variants). Crystal morphologies differed significantly among *LbADH* variants, which would have a direct impact on separation processes on an industrial scale, e.g. during filtration of the crystal suspension (Radel *et al.*, 2019).

Continuing from these observations, crystal dissolution and recrystallization, were successfully conducted for selected mutants. After crystallization and recrystallization the final HCP concentration was below 0.5%, meaning a >100-fold reduction of HCP by two consecutive crystallization steps (measured by HCP-ELISA; illustrated by SDS-PAGE, see **Figure 8.1 E**). High yields were achieved of >95% per crystallization step, demonstrating the implementation of an efficient chromatography-free capture and purification process for the industrial biocatalyst *LbADH*, enabled by crystal contact engineering.

9 Outlook

These studies have laid a foundation for basic research on altered intermolecular interactions at the protein crystal contacts. X-ray datasets have given first hints on improved crystallizability of *LbADH* variants, yet, there are many datasets that do not allow for such an answer, among others due to the fact that many amino acid residues on the surface are not or only weakly dissolved and the orientation and interaction cannot be assessed. Molecular Dynamics (MD) simulations might be helpful to elucidate novel introduced interactions, which remain hidden by static crystallographic analyses. MD simulations could also be applied in the future to reduce the experimental design space by predicting mutations that lead to improved crystallizability. To generate such predicting engineering strategies, it will be essential to expand the experimental basis to other proteins.

From a technical perspective all requirements are met for a successful integration of technical protein crystallization into biotechnological downstream processes as it has been applied in the downstream process (DSP) of industrial insulin (Brange, 1987; Harrison, 2015). The results of this study demonstrate that the strategies of a) introduction of new electrostatic interactions at the crystal contacts and b) systematic combination of positive mutations, can be powerful tools to enhance technical crystallization for efficient capture, purification, and formulation of recombinant proteins. It can be assumed that the engineering approach presented here can be transferred to other proteins.

Further studies on the immobilization and eventual cross-linking of *LbADH* crystals could be of interest for biosensors or (continuous) biocatalysis approaches. In case of *LbADH* mutants, the DSP could be simplified enormously: crystallization from clarified cell harvest, crystal separation (e.g. by filtration or centrifugation), crystal washing, and immobilization.

The crystallization and recrystallization of selected *LbADH* mutants in this work demonstrated for the first time that engineered variants do not only allow for crystallization as a polishing step but also as an efficient capture step revealing high purities and high yields. To go one step further, it is now of interest to investigate the economic benefit of the engineering and crystallization concept, presented here. Since high product yields and purities can be achieved, and relatively inexpensive process equipment can be used, considerable cost savings can be expected for biotechnological DSP.

List of Figures

Figure 3.1: Two amino acids (alanine + leucine) forming a dipeptide (peptide bond via amide linkage) and a water molecule.....	7
Figure 3.2: Chemical structures of all 20 encoded proteinogenic amino acids, categorized according to their residue's biochemical characteristics.....	8
Figure 3.3: Illustration of attractive (a–c) and repulsive (d) π - π interactions of aromatic rings (represented by two facing benzenes).....	9
Figure 3.4: Schematic DSP illustration from crude fermentation broth to purified and formulated recombinant proteins.....	14
Figure 3.5: Three-dimensional structure of the <i>Lb</i> ADH homotetramer in cartoon view.	17
Figure 3.6: Reversible reaction from acetophenone to (<i>R</i>)-1-phenylethanol catalyzed by <i>Lb</i> ADH and cofactor NADP(H).	18
Figure 3.7: Crystals of different proteins.....	18
Figure 3.8: Protein crystallization phase diagram illustrated on the basis of varied concentration of crystallization agent and target protein.....	20
Figure 3.9: Chemical structures of crystallization agents from the most widely used groups (a) salts, (b) organic solvents, (c) low-molecular-weight polymers and nonvolatile organic compounds, and (d) long-chain polymers.....	25
Figure 4.1: Front (A) and side view (B) of the 50 L bioreactor used for the production of <i>Lb</i> ADH WT.....	40
Figure 4.2: Crystallization well of a 24-well vapor diffusion crystallization plate.....	42
Figure 4.3: Mosquito nanodrop dispenser applied for empiric crystallization screenings.....	43
Figure 4.4: Experimental set-up for the stirred mL-experiments.	44
Figure 4.5: Applied automated light microscope for crystallization plates placed in an incubator (located in the crystal lab of the Institute of Biochemical Engineering, TUM, München, Germany).....	50
Figure 5.1: Overlaid IMAC chromatograms of <i>Lb</i> ADH WT (blue solid line) and mutant T102E (green triangles).....	57
Figure 5.2: Microphotograph of the first protein crystals of His ₆ -tagged <i>Lb</i> ADH obtained after 1-step IMAC purification in hanging drop vapor diffusion crystallization experiments.....	58
Figure 5.3: Microphotographs of (a) the largest (1.0 mm ³) and (b) the best neutron-diffracting <i>Lb</i> ADH crystal (0.7 mm ³).....	60

Figure 6.1: Arrangement of four <i>LbADH</i> tetramers in the crystal lattice and the three highlighted crystal contacts #1, #2, and #3.....	64
Figure 6.2: Crystallization microphotographs of <i>LbADH</i> WT and mutant Q126H from four individual experiments.....	66
Figure 6.3: Crystallization microphotographs of <i>LbADH</i> WT and the mutants K32A, Q126H, and Q126K under standard conditions.....	67
Figure 6.4: Heterogeneous crystallization of <i>LbADH</i> WT under standard conditions due to the presence of a foreign nucleating agent.....	67
Figure 6.5: SDS-PAGE of <i>LbADH</i> WT and the mutants K32A, Q126H, and Q126K.	68
Figure 6.6: Crystallization microphotographs of <i>LbADH</i> WT and the mutants K32A, Q126K, and Q126H at standard conditions (top-right, framed images) and at reduced protein and PEG concentrations at 20 °C.....	69
Figure 6.7: Crystallization microphotographs of <i>LbADH</i> WT and the mutants Q207D, Q207E, Q207F, Q207Y, and Q207W at (A) standard condition (5 g L ⁻¹ <i>LbADH</i> and 75 g L ⁻¹ PEG) and (B) at increased protein and PEG concentrations (10 g L ⁻¹ <i>LbADH</i> and 100 g L ⁻¹ PEG).	73
Figure 6.8: Phase diagrams of <i>LbADH</i> WT and the mutants Q126H, Q126K, K32A, and D54F.....	75
Figure 6.9: Crystallographic image illustrating the crystal contact #2 of <i>LbADH</i> WT and K32A.....	77
Figure 6.10: Crystallographic image illustrating the crystal contact #2 of <i>LbADH</i> WT, D54F, and D54Y.....	78
Figure 6.11: Crystallographic image illustrating the crystal contact #1 of <i>LbADH</i> WT and T102E.....	79
Figure 6.12: Crystallographic image illustrating the crystal contact #1 of <i>LbADH</i> WT, Q126H, and Q126K.....	79
Figure 6.13: Crystallographic image illustrating the crystal contact #3 of <i>LbADH</i> WT and Q207Y.....	80
Figure 6.14: Crystallization microphotographs of purified <i>LbADH</i> WT together with the three best-crystallizing single mutants (A) and the two best-crystallizing double mutants (B) on the μL-scale.	81
Figure 6.15: Histograms of the relative maximum enzymatic activities of (A) crystallizable and (B) non-crystallizable <i>LbADH</i> mutants.....	83
Figure 6.16: Enzymatic activities of <i>LbADH</i> WT and six mutants at V_{\max} conditions (left) and reduced acetophenone (center) and NADPH (right) concentrations.....	84
Figure 6.17: Enzymatic activities of <i>LbADH</i> WT and ten double mutants at V_{\max} conditions.....	84
Figure 6.18: Ranked ΔT_m of selected <i>LbADH</i> mutants compared to the WT (T_m WT = 48.6 ± 0.4 °C).....	85

Figure 6.19: Ranked ΔT_m of selected <i>LbADH</i> mutants compared to the WT (A) and the respective thermal transition graphs of WT in comparison to mutants K32A (B), T102E (C), and K32A_T102E (D) as validated by monitoring the change in ellipticity at a set wavelength of 210 nm.	86
Figure 7.1: Crystallization kinetics of three independently produced and purified <i>LbADH</i> WT batches on the stirred mL-scale.....	90
Figure 7.2: (A) Crystallization kinetics and (B) crystal microphotographs of purified <i>LbADH</i> WT on the stirred mL-scale applying different protein concentrations.....	91
Figure 7.3: Crystallization kinetics of purified <i>LbADH</i> WT (different protein batch than used in previous experiments) on the stirred mL-scale applying different protein concentrations.....	92
Figure 7.4: Crystallization kinetics of two purified <i>LbADH</i> WT samples, stored for two different lengths, on the stirred mL-scale.	93
Figure 7.5: (A) Crystallization kinetics and (B) crystal microphotographs of <i>LbADH</i> WT and the first two identified mutants with improved crystallization properties on the stirred mL-scale.	94
Figure 7.6: SDS-PAGE gel of cell lysates of <i>E. coli</i> BL21(DE3) containing <i>LbADH</i> WT and the four single mutants K32A, Q126H, T102E, and D54F.....	95
Figure 7.7: (A,B) Crystallization kinetics and (C) crystal microphotographs of <i>LbADH</i> WT and four single mutants from dialyzed <i>E. coli</i> cell lysate.	96
Figure 7.8: (A) Crystallization kinetics and (B) crystal microphotographs of <i>LbADH</i> WT and the mutants Q126H and T102E at reduced PEG and total protein concentration.....	97
Figure 7.9: (A) Crystallization kinetics from clarified cell lysate and (B) crystal microphotographs of <i>LbADH</i> double mutants T102E_Q126H and D54F_T102E, and single mutant T102E as reference.....	98
Figure 7.10: Reproduced crystallization kinetics of <i>LbADH</i> T102E and D54F_T102E from clarified (clar.) and dialyzed (dial.) cell lysate.	99
Figure 7.11: Crystal microphotographs of <i>LbADH</i> T102E and D54F_T102E from clarified (clar.) and dialyzed (dial.) cell lysate.	100
Figure 7.12: (A) Recrystallization kinetics and (B) crystal microphotographs of <i>LbADH</i> WT and the single mutants K32A, Q126H, and T102E after crystal washing and dissolution.....	101
Figure 7.13: SDS-PAGE visualizing the crystallization yield and the purity effect of crystallization and recrystallization.	102
Figure 8.1: Summary of the results of crystal contact engineering of <i>LbADH</i> mutant T102E.....	108
Figure D.1: Crystallization microphotographs of <i>LbADH</i> WT and mutant T70F at two different PEG concentrations (μ L-scale).....	146

Figure D.2: Crystallization microphotographs of *LbADH* single mutants D54Y and D54F illustrating comparable crystallization behavior (μL -scale). 146

Figure F.1: Melting temperatures (T_m) of three and eight biological replicates for *LbADH* mutant T102E and WT, respectively, demonstrating the high reproducibility of the TSA. 148

Figure F.2: CD spectra of *LbADH* WT and the single mutant K32A and T102E..... 148

List of Tables

Table 3.1: List of biochemical, physical and chemical variables influencing protein crystallization.....	22
Table 4.1: Applied PCR program for site-directed mutagenesis.	35
Table 4.2: Thermocycler protocol used for all QC-PCRs.	35
Table 4.3: Buffer applied in the screening with the aim to find suitable conditions for quick and non-denaturing crystal dissolution of <i>LbADH</i> variants.....	45
Table 6.1: List of all mutations at crystal contact #1.....	71
Table 6.2: List of WT and all single mutants, which were analyzed by X-ray diffraction together with the corresponding space groups, resolution and PDB IDs.....	76
Table 6.3: List of all investigated double mutants with and without synergetic effects, which were partly analyzed by X-ray diffraction together with the corresponding space groups, resolutions and PDB IDs.	82
Table A.1: List of chemicals.	134
Table A.2: List of consumables.....	136
Table A.3: List of Buffers, solutions, and gels.....	136
Table A.4: List of culture media.	138
Table A.5: List of bacterial strains.	139
Table A.6: List of proteins and DNA.....	139
Table A.7: List of primers.	140
Table A.8: List of crystallization equipment.	142
Table A.9: List of software	142
Table A.10: List of commercial kits.....	143
Table E.1: Relative maximum enzymatic activities (in %) of <i>LbADH</i> mutants compared to the WT activity.....	147
Table G.1: Evaluation of the MPD crystallization screening.	149
Table G.2: Evaluation of the JCSG+ crystallization screening.	151

List of Abbreviations

A, Ala	Alanine
ATPE	Aqueous two-phase extraction
BCA (assay)	Bicinchoninic acid (assay)
BIODIFF	Monochromatic single crystal diffractometer at MLZ, Garching
C, Cys	Cysteine
CD	Circular dichroism
CLEC	Cross-linked enzyme crystal
D, Asp	Aspartic acid
DSC	Differential scanning calorimetry
DSP	Downstream process
E, Glu	Glutamic acid
<i>E. coli</i>	<i>Escherichia coli</i>
eGFP	Engineered green fluorescent protein
F, Phe	Phenylalanine
G, Gly	Glycine
HCP	Host cell protein
HEPES	4-(2-hydroxyethyl)-1-piperazineethanesulfonic acid
I, Ile	Isoleucine
IMAC	Immobilized-metal affinity chromatography
K, His	Histidine
K, Lys	Lysine
L, Leu	Leucine
<i>LbADH</i>	Alcohol dehydrogenase from <i>Lactobacillus brevis</i>
<i>LbADH_NHis</i>	<i>LbADH</i> with 13 amino acid linker between protein and tag
<i>LbADH_nL</i>	<i>LbADH</i> without linker between protein and tag
<i>LbADH_sL</i>	<i>LbADH</i> with 3 amino acid linker between protein and tag
M, Met	Methionine
MD	Molecular dynamics
MWCO	Molecular weight cut-off
N, Asn	Asparagine
NMR	Nuclear magnetic resonance spectroscopy
P, Pro	Proline
PBS	phosphate-buffered saline
PCR	Polymerase chain reaction
PEG 550 MME	Polyethylene glycol monomethyl ether (550 kDa)
pI	Isoelectric point
PTM	Post-translational modification
Q, Gln	Glutamine

List of Abbreviations

R, Arg	Arginine
S, Ser	Serine
SAXS	Small-angle X-ray scattering
SDS-PAGE	Sodium dodecyl sulfate polyacrylamide gel electrophoresis
SEC	Size-exclusion chromatography
SER	Surface entropy reduction
T, Thr	Threonine
TEA	Triethanolamine
TSA	Thermal shift assay
V, Val	Valine
W, Trp	Tryptophan
WT	Wild-type protein
Y, Tyr	Tyrosine

List of Bibliography

Abdallah, Bahige G.; Roy-Chowdhury, Shatabdi; Fromme, Raimund; Fromme, Petra; Ros, Alexandra (2016): Protein Crystallization in an Actuated Microfluidic Nanowell Device. In *Crystal Growth & Design* 16 (4), pp. 2074–2082. DOI: 10.1021/acs.cgd.5b01748.

Abdelraheem, Eman M. M.; Busch, Hanna; Hanefeld, Ulf; Tonin, Fabio (2019): Biocatalysis explained: from pharmaceutical to bulk chemical production. In *Reaction Chemistry & Engineering* 4 (11), pp. 1878–1894. DOI: 10.1039/C9RE00301K.

Abel, J. J. (1926): Crystalline Insulin. In *Proceedings of the National Academy of Sciences of the United States of America* 12 (2), pp. 132–136. DOI: 10.1073/pnas.12.2.132.

Alderton, G.; Fevold, H. L. (1946): Direct crystallization of lysozyme from egg white and some crystalline salts of lysozyme. In *The Journal of Biological Chemistry* 164, pp. 1–5.

Arnold, Frances H. (1998): Design by Directed Evolution. In *Accounts of Chemical Research*. 31, pp. 125–131. DOI: 10.1021/ar960017f.

Asenjo, Juan A.; Andrews, Barbara A. (2011): Aqueous two-phase systems for protein separation: a perspective. In *Journal of Chromatography. A* 1218 (49), pp. 8826–8835. DOI: 10.1016/j.chroma.2011.06.051.

Asensio, Juan Luis; Ardá, Ana; Cañada, Francisco Javier; Jiménez-Barbero, Jesús (2013): Carbohydrate-aromatic interactions. In *Accounts of Chemical Research* 46 (4), pp. 946–954. DOI: 10.1021/ar300024d.

Banatao, D. Rey; Cascio, Duilio; Crowley, Christopher S.; Fleissner, Mark R.; Tienson, Heather L.; Yeates, Todd O. (2006): An approach to crystallizing proteins by synthetic symmetrization. In *Proceedings of the National Academy of Sciences of the United States of America* 103 (44), pp. 16230–16235. DOI: 10.1073/pnas.0607674103.

Barros Groß, Michael; Kind, Matthias (2018): From microscale phase screening to bulk evaporative crystallization of proteins. In *Journal of Crystal Growth* 498, pp. 160–169. DOI: 10.1016/j.jcrysgro.2018.06.010.

Basu, Sujit K.; Govardhan, Chandrika P.; Jung, Chu W.; Margolin, Alexey L. (2004): Protein crystals for the delivery of biopharmaceuticals. In *Expert Opinion on Biological Therapy* 4 (3), pp. 301–317. DOI: 10.1517/14712598.4.3.301.

Baumgartner, Kai; Galm, Lara; Nötzold, Juliane; Sigloch, Heike; Morgenstern, Josefine; Schleining, Kristina et al. (2015): Determination of protein phase diagrams by microbatch experiments. Exploring the influence of precipitants and pH. In *International Journal of Pharmaceutics* 479 (1), pp. 28–40. DOI: 10.1016/j.ijpharm.2014.12.027.

Bhosale, S. H.; Rao, M. B.; Deshpande, V. V. (1996): Molecular and industrial aspects of glucose isomerase. In *Microbiological Reviews* 60 (2), pp. 280–300.

Blakeley, Matthew P.; Langan, Paul; Niimura, Nobuo; Podjarny, Alberto (2008): Neutron crystallography: opportunities, challenges, and limitations. In *Current Opinion in Structural Biology* 18 (5), pp. 593–600. DOI: 10.1016/j.sbi.2008.06.009.

- Botsaris, Gregory D. (1976): Secondary Nucleation — A Review. In J. W. Mullin (Ed.): *Industrial Crystallization*. Boston, MA: Springer US, pp. 3–22.
- Bräutigam, Stefan; Bringer-Meyer, Stephanie; Weuster-Botz, Dirk (2007): Asymmetric whole cell biotransformations in biphasic ionic liquid/water-systems by use of recombinant *Escherichia coli* with intracellular cofactor regeneration. In *Tetrahedron: Asymmetry* 18 (16), pp. 1883–1887. DOI: 10.1016/j.tetasy.2007.08.003.
- Bräutigam, Stefan; Dennewald, Danielle; Schürmann, Melanie; Lutje-Spelberg, Jeffrey; Pitner, William-Robert; Weuster-Botz, Dirk (2009): Whole-cell biocatalysis. Evaluation of new hydrophobic ionic liquids for efficient asymmetric reduction of prochiral ketones. In *Enzyme and Microbial Technology* 45 (4), pp. 310–316. DOI: 10.1016/j.enzmictec.2009.06.015.
- Brange, Jens (1987): *Galenics of Insulin. The Physico-chemical and Pharmaceutical Aspects of Insulin and Insulin Preparations*. Berlin, Heidelberg: Springer Berlin Heidelberg.
- Burgstaller, Daniel; Jungbauer, Alois; Satzer, Peter (2019): Continuous integrated antibody precipitation with two-stage tangential flow microfiltration enables constant mass flow. In *Biotechnology and Bioengineering* 116 (5), pp. 1053–1065. DOI: 10.1002/bit.26922.
- Burley, S. K.; Petsko, G. A. (1985): Aromatic-aromatic interaction. A mechanism of protein structure stabilization. In *Science (New York, N.Y.)* 229 (4708), pp. 23–28. DOI: 10.1126/science.3892686
- Campbell, Elliot; Meredith, Matthew; Minter, Shelley D.; Banta, Scott (2012): Enzymatic biofuel cells utilizing a biomimetic cofactor. In *Chemical Communications (Cambridge, England)* 48 (13), pp. 1898–1900. DOI: 10.1039/c2cc16156g.
- Carbone, Martina N.; Etzel, Mark R. (2006): Seeded isothermal batch crystallization of lysozyme. In *Biotechnology and Bioengineering* 93 (6), pp. 1221–1224. DOI: 10.1002/bit.20813.
- Carson, Mike; Johnson, David H.; McDonald, Heather; Brouillette, Christie; Delucas, Lawrence J. (2007): His-tag impact on structure. In *Acta Crystallographica. Section D, Biological Crystallography* 63 (Pt 3), pp. 295–301. DOI: 10.1107/S0907444906052024.
- Chayen, Naomi E.; Saridakis, Emmanuel (2008): Protein crystallization: from purified protein to diffraction-quality crystal. In *Nature Methods* 5 (2), pp. 147–153. DOI: 10.1038/nmeth.f.203.
- Chen, Rui-Qing; Lu, Qin-Qin; Cheng, Qing-Di; Ao, Liang-Bo; Zhang, Chen-Yan; Hou, Hai et al. (2015): An ignored variable: Solution preparation temperature in protein crystallization. In *Scientific Reports* 5, p. 7797. DOI: 10.1038/srep07797.
- Chernov, Alexander A. (2003): Protein crystals and their growth. In *Journal of Structural Biology* 142 (1), pp. 3–21. DOI: 10.1016/S1047-8477(03)00034-0.
- Cieřlik, Marcin; Derewenda, Zygmunt S. (2009): The role of entropy and polarity in intermolecular contacts in protein crystals. In *Acta Crystallographica. Section D, Biological Crystallography* 65 (Pt 5), pp. 500–509. DOI: 10.1107/S0907444909009500.
- Conejero-Muriel, Mayte; Rodríguez-Ruiz, Isaac; Verdugo-Escamilla, Cristóbal; Llobera, Andreu; Gavira, José A. (2016): Continuous Sensing Photonic Lab-on-a-Chip Platform Based on Cross-Linked Enzyme Crystals. In *Analytical Chemistry* 88 (23), pp. 11919–11923. DOI: 10.1021/acs.analchem.6b03793.

- Cooper, David R.; Boczek, Tomasz; Grelewska, Katarzyna; Pinkowska, Malgorzata; Sikorska, Malgorzata; Zawadzki, Michal; Derewenda, Zygmunt (2007): Protein crystallization by surface entropy reduction. Optimization of the SER strategy. In *Acta Crystallographica. Section D, Biological Crystallography* 63 (Pt 5), pp. 636–645. DOI: 10.1107/S0907444907010931.
- Costioli, M.D. & Guillemot-Potelle, C. & Mitchell-Logean, C. & Broly, Herve (23): Cost of goods modeling and quality by design for developing cost-effective processes. In *BioPharm International* 2010, pp. 26–35.
- Czepas, Jan; Devedjiev, Yancho; Krowarsch, Daniel; Derewenda, Urszula; Otlewski, Jacek; Derewenda, Zygmunt S. (2004): The impact of Lys→Arg surface mutations on the crystallization of the globular domain of RhoGDI. In *Acta Crystallographica. Section D, Biological Crystallography* 60 (Pt 2), pp. 275–280. DOI: 10.1107/S0907444903026271.
- Dale, Glenn E.; Oefner, Christian; D'Arcy, Allan (2003): The protein as a variable in protein crystallization. In *Journal of Structural Biology* 142 (1), pp. 88–97. DOI: 10.1016/S1047-8477(03)00041-8
- D'Arcy, A.; Stihle, M.; Kostrewa, D.; Dale, G. (1999): Crystal engineering: a case study using the 24 kDa fragment of the DNA gyrase B subunit from *Escherichia coli*. In *Acta Crystallographica. Section D, Biological Crystallography* 55 (Pt 9), pp. 1623–1625. DOI: 10.1107/s0907444999008136.
- Dasgupta, Swagata; Iyer, Ganesh H.; Bryant, Stephen H.; Lawrence, Charles E.; Bell, Jeffrey A. (1997): Extent and nature of contacts between protein molecules in crystal lattices and between subunits of protein oligomers. In *Proteins* 28 (4), pp. 494–514. DOI: 10.1002/(SICI)1097-0134(199708)28:4<494::AID-PROT4>3.0.CO;2-A.
- Davies, David R. (1964): A correlation between amino acid composition and protein structure. In *Journal of Molecular Biology* 9 (2), pp. 605–609. DOI: 10.1016/s0022-2836(64)80232-1.
- Dennewald, Danielle; Pitner, William-Robert; Weuster-Botz, Dirk (2011): Recycling of the ionic liquid phase in process integrated biphasic whole-cell biocatalysis. In *Process Biochemistry* 46 (5), pp. 1132–1137. DOI: 10.1016/j.procbio.2011.01.032.
- Derewenda, Zygmunt S. (2004): Rational protein crystallization by mutational surface engineering. In *Structure (London, England: 1993)* 12 (4), pp. 529–535. DOI: 10.1016/j.str.2004.03.008.
- Derewenda, Zygmunt S. (2004): The use of recombinant methods and molecular engineering in protein crystallization. In *Methods (San Diego, Calif.)* 34 (3), pp. 354–363. DOI: 10.1016/j.ymeth.2004.03.024.
- Derewenda, Zygmunt S. (2007): Protein crystallization in drug design: towards a rational approach. In *Expert Opinion on Drug Discovery* 2 (10), pp. 1329–1340. DOI: 10.1517/17460441.2.10.1329.
- Derewenda, Zygmunt S.; Godzik, Adam (2017): The "Sticky Patch" Model of Crystallization and Modification of Proteins for Enhanced Crystallizability. In *Methods in Molecular Biology (Clifton, N.J.)* 1607, pp. 77–115. DOI: 10.1007/978-1-4939-7000-1_4.
- Derewenda, Zygmunt S.; Vekilov, Peter G. (2006): Entropy and surface engineering in protein crystallization. In *Acta Crystallographica. Section D, Biological Crystallography* 62 (Pt 1), pp. 116–124. DOI: 10.1107/S0907444905035237.
- Donald, Jason E.; Kulp, Daniel W.; DeGrado, William F. (2011): Salt bridges: geometrically specific, designable interactions. In *Proteins* 79 (3), pp. 898–915. DOI: 10.1002/prot.22927.

Doran, Pauline M. (2013): Bioprocess engineering principles. 2nd ed. Waltham, MA: Academic Press. Available online at <http://www.sciencedirect.com/science/book/9780122208515>.

Dos Santos, Raquel; Carvalho, Ana Luísa; Roque, A. Cecília A. (2016): Renaissance of protein crystallization and precipitation in biopharmaceuticals purification. In *Biotechnology Advances* 35 (1), pp. 41–50. DOI: 10.1016/j.biotechadv.2016.11.005.

Dougherty, Dennis A. (2007): Cation- π interactions involving aromatic amino acids. In *The Journal of Nutrition* 137 (6 Suppl 1), 1504S-1508S; discussion 1516S-1517S.

Doye, Jonathan P. K.; Louis, Ard A.; Vendruscolo, Michele (2004): Inhibition of protein crystallization by evolutionary negative design. In *Physical Biology* 1 (1-2), P9-13. DOI: 10.1088/1478-3967/1/1/P02.

Duhamel, Raymond C.; Schur, Peter H.; Brendel, Klaus; Meezan, Elias (1979): pH gradient elution of human IgG1, IgG2 and IgG4 from protein A-Sepharose. In *Journal of Immunological Methods* 31 (3-4), pp. 211–217. DOI: 10.1016/0022-1759(79)90133-9.

Dupeux, Florine; Röwer, Martin; Seroul, Gael; Blot, Delphine; Márquez, José A. (2011): A thermal stability assay can help to estimate the crystallization likelihood of biological samples. In *Acta Crystallographica. Section D, Biological Crystallography* 67 (Pt 11), pp. 915–919. DOI: 10.1107/S0907444911036225.

Emsley, P.; Lohkamp, B.; Scott, W. G.; Cowtan, K. (2010): Features and development of Coot. In *Acta Crystallographica. Section D, Biological Crystallography* 66 (Pt 4), pp. 486–501. DOI: 10.1107/S0907444910007493.

Englard, Sasha; Seifter, Sam (1990): Precipitation techniques. In: Guide to Protein Purification, vol. 182: Elsevier (Methods in Enzymology), pp. 285–300.

Ereky, Karl. (1919): Biotechnologie der Fleisch-, Fett-, und Milcherzeugung im landwirtschaftlichen Grossbetriebe: für naturwissenschaftlich gebildete Landwirte verfasst. Berlin: P. Parey. Available online at [//catalog.hathitrust.org/Record/006798043](http://catalog.hathitrust.org/Record/006798043).

Ernst, Marianne; Kaup, Bjorn; Muller, Michael; Bringer-Meyer, Stephanie; Sahm, Hermann (2005): Enantioselective reduction of carbonyl compounds by whole-cell biotransformation, combining a formate dehydrogenase and a (*R*)-specific alcohol dehydrogenase. In *Applied Microbiology and Biotechnology* 66 (6), pp. 629–634. DOI: 10.1007/s00253-004-1765-5.

Evans, Philip R.; Murshudov, Garib N. (2013): How good are my data and what is the resolution? In *Acta Crystallographica. Section D, Biological Crystallography* 69 (Pt 7), pp. 1204–1214. DOI: 10.1107/S0907444913000061.

Ferreira-Faria, Diogo; Aires-Barros, M. Raquel; Azevedo, Ana M. (2020): Continuous aqueous two-phase extraction: From microfluidics to integrated biomanufacturing. In *Fluid Phase Equilibria* 508, p. 112438. DOI: 10.1016/j.fluid.2019.112438.

Fields, Peter A.; Dong, Yunwei; Meng, Xianliang; Somero, George N. (2015): Adaptations of protein structure and function to temperature: there is more than one way to 'skin a cat'. In *The Journal of Experimental Biology* 218 (Pt 12), pp. 1801–1811. DOI: 10.1242/jeb.114298.

Gallivan, J. P.; Dougherty, D. A. (1999): Cation- π interactions in structural biology. In *Proceedings of the National Academy of Sciences of the United States of America* 96 (17), pp. 9459–9464. DOI: 10.1073/pnas.96.17.9459.

- Gasteiger, Elisabeth; Hoogland, Christine; Gattiker, Alexandre; Duvaud, S'everine; Wilkins, Marc R.; Appel, Ron D.; Bairoch, Amos (2005): Protein Identification and Analysis Tools on the ExPASy Server. In John M. Walker (Ed.): *The Proteomics Protocols Handbook*. Totowa, NJ: Humana Press Inc (Methods in Molecular Biology), pp. 571–607.
- Gillespie, C. M.; Asthagiri, D.; Lenhoff, A. M. (2014): Polymorphic Protein Crystal Growth: Influence of Hydration and Ions in Glucose Isomerase. In *Crystal Growth & Design* 14 (1), pp. 46–57. DOI: 10.1021/cg401063b.
- Glover, Karen; Li, Yue; Mukhopadhyay, Shreya; Leuthner, Zoe; Chakravarthy, Srinivas; Colbert, Christopher L.; Sinha, Sangita C. (2017): Structural transitions in conserved, ordered Beclin 1 domains essential to regulating autophagy. In *The Journal of Biological Chemistry* 292 (39), pp. 16235–16248. DOI: 10.1074/jbc.M117.804195.
- Goldschmidt, Lukasz; Cooper, David R.; Derewenda, Zygmunt S.; Eisenberg, David (2007): Toward rational protein crystallization: A Web server for the design of crystallizable protein variants. In *Protein Science: a Publication of the Protein Society* 16 (8), pp. 1569–1576. DOI: 10.1110/ps.072914007.
- Grob, Phillip; Huber, Max; Walla, Brigitte; Hermann, Johannes; Janowski, Robert; Niessing, Dierk et al. (2020): Crystal Contact Engineering Enables Efficient Capture and Purification of an Oxidoreductase by Technical Crystallization. In *Biotechnology Journal*, e2000010. DOI: 10.1002/biot.202000010.
- Hammerschmidt, Nikolaus; Hintersteiner, Beate; Lingg, Nico; Jungbauer, Alois (2015): Continuous precipitation of IgG from CHO cell culture supernatant in a tubular reactor. In *Biotechnology Journal* 10 (8), pp. 1196–1205. DOI: 10.1002/biot.201400608.
- Hammerschmidt, Nikolaus; Hobiger, Stefanie; Jungbauer, Alois (2016): Continuous polyethylene glycol precipitation of recombinant antibodies: Sequential precipitation and resolubilization. In *Process Biochemistry* 51 (2), pp. 325–332. DOI: 10.1016/j.procbio.2015.11.032.
- Hammerschmidt, Nikolaus; Tscheliessnig, Anne; Sommer, Ralf; Helk, Bernhard; Jungbauer, Alois (2014): Economics of recombinant antibody production processes at various scales: Industry-standard compared to continuous precipitation. In *Biotechnology Journal* 9 (6), pp. 766–775. DOI: 10.1002/biot.201300480.
- Harrison, Roger G.; Todd, Paul; Rudge, Scott R.; Petrides, Demetri P. (2015): *Bioseparations Science and Engineering*. Second edition. Oxford: Oxford University Press.
- Hartje, Luke F.; Bui, Hieu T.; Andales, David A.; James, Susan P.; Huber, Thaddaus R.; Snow, Christopher D. (2018): Characterizing the Cytocompatibility of Various Cross-Linking Chemistries for the Production of Biostable Large-Pore Protein Crystal Materials. In *ACS Biomater. Sci. Eng.* 4 (3), pp. 826–831. DOI: 10.1021/acsbiomaterials.8b00023.
- Hartje, Luke F.; Snow, Christopher D. (2018): Protein crystal based materials for nanoscale applications in medicine and biotechnology. In *Wiley Interdisciplinary Reviews. Nanomedicine and Nanobiotechnology*, e1547. DOI: 10.1002/wnan.1547.
- Hebel, Dirk; Huber, Sabine; Stanislawski, Bernd; Hekmat, Dariusch (2013b): Stirred batch crystallization of a therapeutic antibody fragment. In *Journal of Biotechnology* 166 (4), pp. 206–211. DOI: 10.1016/j.jbiotec.2013.05.010.
- Hebel, Dirk; Ürdingen, Mark; Hekmat, Dariusch; Weuster-Botz, Dirk (2013a): Development and Scale up of High-Yield Crystallization Processes of Lysozyme and Lipase Using Additives. In *Crystal Growth & Design* 13 (6), pp. 2499–2506. DOI: 10.1021/cg400212p.

- Heigl, R. J.; Longo, M.; Stellbrink, J.; Radulescu, A.; Schweins, R.; Schrader, T. E. (2018): Crossover from a Linear to a Branched Growth Regime in the Crystallization of Lysozyme. In *Crystal Growth & Design* 18 (3), pp. 1483–1494. DOI: 10.1021/acs.cgd.7b01433.
- Hekmat, Dariusch (2015b): Large-scale crystallization of proteins for purification and formulation. In *Bioprocess and Biosystems Engineering* 38 (7), pp. 1209–1231. DOI: 10.1007/s00449-015-1374-y.
- Hekmat, Dariusch; Breitschwerdt, Peter; Weuster-Botz, Dirk (2015c): Purification of proteins from solutions containing residual host cell proteins via preparative crystallization. In *Biotechnology Letters* 37 (9), pp. 1791–1801. DOI: 10.1007/s10529-015-1866-5.
- Hekmat, Dariusch; Huber, Max; Lohse, Christian; den Eichen, Nikolas von; Weuster-Botz, Dirk (2017): Continuous Crystallization of Proteins in a Stirred Classified Product Removal Tank with a Tubular Reactor in Bypass. In *Crystal Growth & Design* 17 (8), pp. 4162–4169. DOI: 10.1021/acs.cgd.7b00436.
- Hekmat, Dariusch; Maslak, Dominik; Freiherr von Roman, Matthias; Breitschwerdt, Peter; Ströhle, Christoph; Vogt, Alexander et al. (2015a): Non-chromatographic preparative purification of enhanced green fluorescent protein. In *Journal of Biotechnology* 194, pp. 84–90. DOI: 10.1016/j.jbiotec.2014.11.027.
- Henzler, H. J. (2000): Particle stress in bioreactors. In *Advances in Biochemical Engineering/Biotechnology* 67, pp. 35–82. DOI: 10.1007/3-540-47865-5_2.
- Hermann, Johannes; Nowotny, Phillip; Schrader, Tobias E; Biggel, Philipp; Hekmat, Dariusch; Weuster-Botz, Dirk (2018): Neutron and X-ray crystal structures of *Lactobacillus brevis* alcohol dehydrogenase reveal new insights on hydrogen bonding pathways. *Acta Cryst F* 74: 754-764. DOI: 10.1107/S2053230X18015273
- Hermanson, Greg T. (2013): Zero-Length Crosslinkers. In G. T. Hermanson (Ed.): *Bioconjugate Techniques*: Elsevier, pp. 259–273.
- Hober, Sophia; Nord, Karin; Linhult, Martin (2007): Protein A chromatography for antibody purification. In *Journal of Chromatography. B, Analytical technologies in the biomedical and life sciences* 848 (1), pp. 40–47. DOI: 10.1016/j.jchromb.2006.09.030.
- Hofmeister, Franz (1888): Zur Lehre von der Wirkung der Salze. In *Archiv für experimentelle Pathologie und Pharmakologie* 24 (4-5), pp. 247–260. DOI: 10.1007/BF01918191.
- Hofmeister, Franz (1890): Über die Darstellung von krystallisiertem Eiralbumin und die Krystallisirbarkeit colloider Stoffe (14), p. 165.
- Hummel, Werner (1997): New alcohol dehydrogenases for the synthesis of chiral compounds. In T. Scheper, W. Babel, H. W. Blanch, Ch. L. Cooney, S.-O Enfors, K.-E. L. Eriksson et al. (Eds.): *New Enzymes for Organic Synthesis*, vol. 58. Berlin, Heidelberg: Springer Berlin Heidelberg (Advances in Biochemical Engineering/Biotechnology), pp. 145–184.
- Hünefeld, F. L. (1840): *Der Chemismus in der thierischen Organisation. Physiologisch-chemische Untersuchungen der materiellen Veränderungen oder des Bildungslebens im thierischen Organismus, insbesondere des Blutbildungsprocesses, der Natur der Blutkörperchen und ihrer Kernchen* (Brockhaus, 1840).
- Igarashi, Koichi; Azuma, Masayuki; Kato, Jyoji; Ooshima, Hiroshi (1999): The initial stage of crystallization of lysozyme: a differential scanning calorimetric (DSC) study. In *Journal of Crystal Growth* 204 (1-2), pp. 191–200. DOI: 10.1016/S0022-0248(99)00181-5.

- Ingham, Kenneth C. (1990): Precipitation of proteins with polyethylene glycol. In: Guide to Protein Purification, vol. 182: Elsevier (Methods in Enzymology), pp. 301–306.
- Jacobsen, C.; Garside, J.; Hoare, M. (1998): Nucleation and growth of microbial lipase crystals from clarified concentrated fermentation broths. In *Biotechnology and Bioengineering* 57 (6), pp. 666–675. DOI: 10.1002/(SICI)1097-0290(19980320)57:6<666::AID-BIT4>3.0.CO;2-J.
- Jenkins, T. M.; Hickman, A. B.; Dyda, F.; Ghirlando, R.; Davies, D. R.; Craigie, R. (1995): Catalytic domain of human immunodeficiency virus type 1 integrase. Identification of a soluble mutant by systematic replacement of hydrophobic residues. In *Proceedings of the National Academy of Sciences of the United States of America* 92 (13), pp. 6057–6061.
- Johnson, Paley (1949): “Crystalline enzymes.” Northrop, Kunitz, and Herriott. Columbia Univ. Press, New York, 1948, 352 pp., \$7.50. In *J. Polym. Sci.* 4 (4), pp. 543–544. DOI: 10.1002/pol.1949.120040414.
- Jones, S.; Thornton, J. M. (1996): Principles of protein-protein interactions. In *Proceedings of the National Academy of Sciences of the United States of America* 93 (1), pp. 13–20. DOI: 10.1073/pnas.93.1.13.
- Joosten, Robbie P.; Long, Fei; Murshudov, Garib N.; Perrakis, Anastassis (2014): The PDB_REDO server for macromolecular structure model optimization. In *IUCr* 1 (Pt 4), pp. 213–220. DOI: 10.1107/S2052252514009324.
- Judge, R. A.; Johns, M. R.; White, E. T. (1995): Protein purification by bulk crystallization: the recovery of ovalbumin. In *Biotechnology and Bioengineering* 48 (4), pp. 316–323. DOI: 10.1002/bit.260480404.
- Kabsch, Wolfgang (2010): Integration, scaling, space-group assignment and post-refinement. In *Acta Crystallographica. Section D, Biological Crystallography* 66 (Pt 2), pp. 133–144. DOI: 10.1107/S0907444909047374.
- Kleber, Will; Bautsch, Hans-Joachim; Bohm, Joachim (2010): Einführung in die Kristallographie. München: Oldenbourg. Available online at <http://www.reference-global.com/doi/book/10.1515/9783486598858>.
- Kohlmann, Christina; Leuchs, Susanne; Greiner, Lasse; Leitner, Walter (2011): Continuous biocatalytic synthesis of (*R*)-2-octanol with integrated product separation. In *Green Chemistry* 13 (6), p. 1430. DOI: 10.1039/C0GC00790K.
- Laemmli, U. K. (1970): Cleavage of structural proteins during the assembly of the head of bacteriophage T4. In *Nature* 227 (5259), pp. 680–685. DOI: 10.1038/227680a0.
- Laganowsky, Arthur; Zhao, Minglei; Soriaga, Angela B.; Sawaya, Michael R.; Cascio, Duilio; Yeates, Todd O. (2011): An approach to crystallizing proteins by metal-mediated synthetic symmetrization. In *Protein Science: a Publication of the Protein Society* 20 (11), pp. 1876–1890. DOI: 10.1002/pro.727.
- Lalonde, Jim J.; Govardhan, Chandrika; Khalaf, Nazer; Martinez, Aldo G.; Visuri, Kalevi; Margolin, Alexey L. (1995): Cross-Linked Crystals of *Candida rugosa* Lipase: Highly Efficient Catalysts for the Resolution of Chiral Esters. In *J. Am. Chem. Soc.* 117 (26), pp. 6845–6852. DOI: 10.1021/ja00131a006.
- Lawson, D. M.; Artymiuk, P. J.; Yewdall, S. J.; Smith, J. M.; Livingstone, J. C.; Treffry, A. et al. (1991): Solving the structure of human H ferritin by genetically engineering intermolecular crystal contacts. In *Nature* 349 (6309), pp. 541–544. DOI: 10.1038/349541a0.

- Lee, Timothy S.; Vaghjiani, Jeetendra D.; Lye, Gary J.; Turner, Michael K. (2000): A systematic approach to the large-scale production of protein crystals. In *Enzyme and Microbial Technology* 26 (8), pp. 582–592. DOI: 10.1016/s0141-0229(99)00194-5.
- Leuchs, S.; Greiner, L. (2011): Alcohol Dehydrogenase from *Lactobacillus brevis*: A Versatile Robust Catalyst for Enantioselective Transformations. In *Chemical and Biochemical Engineering Quarterly*. 25.
- Longenecker, K. L.; Garrard, S. M.; Sheffield, P. J.; Derewenda, Z. S. (2001): Protein crystallization by rational mutagenesis of surface residues. Lys to Ala mutations promote crystallization of RhoGDI. In *Acta Crystallographica. Section D, Biological Crystallography* 57 (Pt 5), pp. 679–688.
- Luiz de Mattos, I. (2001): Evaluation of glucose biosensors based on Prussian Blue and lyophilised, crystalline and cross-linked glucose oxidases (CLEC®). In *Talanta* 54 (5), pp. 963–974. DOI: 10.1016/s0039-9140(01)00367-8.
- Machielsen, Ronnie; Looger, Loren L.; Raedts, John; Dijkhuizen, Sjoerd; Hummel, Werner; Hennemann, Hans-Georg et al. (2009): Cofactor engineering of *Lactobacillus brevis* alcohol dehydrogenase by computational design. In *Eng. Life Sci.* 9 (1), pp. 38–44. DOI: 10.1002/elsc.200800046.
- Mähler, Christoph; Kratzl, Franziska; Vogel, Melina; Vinnenberg, Stefan; Weuster-Botz, Dirk; Castiglione, Kathrin (2019): Loop Swapping as a Potent Approach to Increase Ene Reductase Activity with Nicotinamide Adenine Dinucleotide (NADH). In *Adv. Synth. Catal.* DOI: 10.1002/adsc.201900073.
- Margolin, Alexey L.; Navia, Manuel A. (2001): Protein Crystals as Novel Catalytic Materials. In *Angewandte Chemie Int. Ed.* 40 (12), pp. 2204–2222. DOI: 10.1002/1521-3773(20010618)40:12<2204::AID-ANIE2204>3.0.CO;2-J.
- Matthews, B. W. (1968): Solvent content of protein crystals. In *Journal of Molecular Biology* 33 (2), pp. 491–497. DOI: 10.1016/0022-2836(68)90205-2.
- McCoy, Airlie J.; Grosse-Kunstleve, Ralf W.; Adams, Paul D.; Winn, Martyn D.; Storoni, Laurent C.; Read, Randy J. (2007): Phaser crystallographic software. In *Journal of Applied Crystallography* 40 (Pt 4), pp. 658–674. DOI: 10.1107/S0021889807021206.
- McElroy, H. E.; Sisson, G. W.; Schoettlin, W. E.; Aust, R. M.; Villafranca, J. E. (1992): Studies on engineering crystallizability by mutation of surface residues of human thymidylate synthase. In *Journal of Crystal Growth* 122 (1-4), pp. 265–272. DOI: 10.1016/0022-0248(92)90255-H.
- McGaughey, G. B.; Gagné, M.; Rappé, A. K. (1998): pi-Stacking interactions. Alive and well in proteins. In *The Journal of Biological Chemistry* 273 (25), pp. 15458–15463. DOI: 10.1074/jbc.273.25.15458.
- McPherson, A.; Malkin, A. J.; Kuznetsov, YuG (2000): Atomic force microscopy in the study of macromolecular crystal growth. In *Annual Review of Biophysics and Biomolecular Structure* 29, pp. 361–410. DOI: 10.1146/annurev.biophys.29.1.361.
- McPherson, Alexander (1999): Crystallization of biological macromolecules. Cold Spring Harbor, NY: Cold Spring Harbor Laboratory Press.
- McPherson, Alexander (2009): Introduction to macromolecular crystallography. 2nd ed. Hoboken, NJ: Wiley-Blackwell. Available online at <http://opac.ub.tum.de/InfoGuideClient.tumsis/start.do?Login=wotum07&Query=540=978-0-470-18590-2>.

- McPherson, Alexander; Gavira, Jose A. (2014): Introduction to protein crystallization. In *Acta crystallographica. Section F, Structural Biology Communications* 70 (Pt 1), pp. 2–20. DOI: 10.1107/S2053230X13033141.
- Merkle, Hans P.; Jen, Anna (2002): A crystal clear solution for insulin delivery. In *Nature Biotechnology* 20 (8), pp. 789–790. DOI: 10.1038/nbt0802-789.
- Murshudov, Garib N.; Skubák, Pavol; Lebedev, Andrey A.; Pannu, Navraj S.; Steiner, Roberto A.; Nicholls, Robert A. et al. (2011): REFMAC5 for the refinement of macromolecular crystal structures. In *Acta Crystallographica. Section D, Biological Crystallography* 67 (Pt 4), pp. 355–367. DOI: 10.1107/S0907444911001314.
- Natarajan, Venkatesh; Zydney, Andrew L. (2013): Protein A chromatography at high titers. In *Biotechnology and Bioengineering* 110 (9), pp. 2445–2451. DOI: 10.1002/bit.24902.
- Neel, Andrew J.; Hilton, Margaret J.; Sigman, Matthew S.; Toste, F. Dean (2017): Exploiting non-covalent π interactions for catalyst design. In *Nature* 543 (7647), pp. 637–646. DOI: 10.1038/nature21701.
- Newman, Janet; Xu, Jian; Willis, Michael C. (2007): Initial evaluations of the reproducibility of vapor-diffusion crystallization. In *Acta Crystallographica. Section D, Biological Crystallography* 63 (Pt 7), pp. 826–832. DOI: 10.1107/S0907444907025784.
- Niefind, K.; Riebel, B.; Müller, J.; Hummel, W.; Schomburg, D. (2000): Crystallization and preliminary characterization of crystals of R-alcohol dehydrogenase from *Lactobacillus brevis*. In *Acta Crystallographica. Section D, Biological Crystallography* 56 (Pt 12), pp. 1696–1698. DOI: 10.1107/S0907444900011860.
- Niefind, Karsten; Müller, Jörg; Riebel, Bettina; Hummel, Werner; Schomburg, Dietmar (2003): The Crystal Structure of R-specific Alcohol Dehydrogenase from *Lactobacillus brevis* Suggests the Structural Basis of its Metal Dependency. In *Journal of Molecular Biology* 327 (2), pp. 317–328. DOI: 10.1016/S0022-2836(03)00081-0.
- Noritomi, Hidetaka; Koyama, Kazutake; Kato, Satoru; Nagahama, Kunio (1998): Increased thermostability of cross-linked enzyme crystals of subtilisin in organic solvents. In *Biotechnology Techniques* 12 (6), pp. 467–469. DOI: 10.1023/A:1008863407130.
- Northrop, J. H. (1930): Crystalline pepsin. In *Science* (69), p. 580.
- Nowotny, Phillip; Hermann, Johannes; Li, Jianing; Krautenbacher, Angela; Klöpfer, Kai; Hekmat, Dariusch; Weuster-Botz, Dirk (2019): Rational Crystal Contact Engineering of *Lactobacillus brevis* Alcohol Dehydrogenase To Promote Technical Protein Crystallization. In *Crystal Growth & Design* 19 (4), pp. 2380–2387. DOI: 10.1021/acs.cgd.9b00067.
- Ooshima, H.; Urabe, S.; Igarashi, K.; Azuma, M.; Kato, J. (1997): Mechanism of Crystal Growth of Protein: Differential Scanning Calorimetry of Thermolysin Crystal Suspension. In Gregory D. Botsaris, Ken Toyokura (Eds.): *Separation and Purification by Crystallization*, vol. 667. Washington, DC: American Chemical Society (ACS Symposium Series), pp. 18–27.
- Ostermann, Andreas; Schrader, Tobias (2015): BIODIFF: Diffractometer for large unit cells. In *Journal of Large-scale Research Facilities*. DOI: 10.17815/jlsrf-1-19.
- Pace, C. Nick; Fu, Hailong; Fryar, Katrina Lee; Landua, John; Trevino, Saul R.; Shirley, Bret A. et al. (2011): Contribution of hydrophobic interactions to protein stability. In *Journal of Molecular Biology* 408 (3), pp. 514–528. DOI: 10.1016/j.jmb.2011.02.053.

Pace, C. Nick; Fu, Hailong; Lee Fryar, Katrina; Landua, John; Trevino, Saul R.; Schell, David et al. (2014): Contribution of hydrogen bonds to protein stability. In *Protein Science: a Publication of the Protein Society* 23 (5), pp. 652–661. DOI: 10.1002/pro.2449.

Pifat-Mrzljak, Greta (2007): *Supramolecular Structure and Function* 9. Dordrecht: Springer. Available online at <http://site.ebrary.com/lib/alltitles/docDetail.action?docID=10210734>.

Przybycien, Todd M.; Pujar, Narahari S.; Steele, Landon M. (2004): Alternative bioseparation operations: life beyond packed-bed chromatography. In *Current Opinion in Biotechnology* 15 (5), pp. 469–478. DOI: 10.1016/j.copbio.2004.08.008.

Radel, B.; Funck, M.; Nguyen, T. H.; Nirschl, H. (2019): Determination of filtration and consolidation properties of protein crystal suspensions using analytical photocentrifuges with low volume samples. In *Chemical Engineering Science* 196, pp. 72–81. DOI: 10.1016/j.ces.2018.12.019.

Riebel, Bettina (1997): *Biochemische und molekularbiologische Charakterisierung neuer mikrobieller NAD(P)-abhängiger Alkoholdehydrogenasen*. Egelsbach: Hänsel-Mikroedition (Deutsche Hochschulschriften, 2478).

Riesenberg, Dieter (1991): High-cell-density cultivation of *Escherichia coli*. In *Current Opinion in Biotechnology* 2 (3), pp. 380–384. DOI: 10.1016/s0958-1669(05)80142-9.

Riley, Kevin E.; Hobza, Pavel (2013): On the importance and origin of aromatic interactions in chemistry and biodisciplines. In *Accounts of Chemical Research* 46 (4), pp. 927–936. DOI: 10.1021/ar300083h.

Sauter, Andrea; Roosen-Runge, Felix; Zhang, Fajun; Lotze, Gudrun; Jacobs, Robert M. J.; Schreiber, Frank (2015): Real-time observation of nonclassical protein crystallization kinetics. In *Journal of the American Chemical Society* 137 (4), pp. 1485–1491. DOI: 10.1021/ja510533x.

Schlieben, Nils Helge (2001): *Die Kristallstruktur eines ternären Komplexes der R-spezifischen Alkoholdehydrogenase aus Lactobacillus brevis in atomarer Auflösung*. Universität zu Köln, Köln.

Schmideder, Andreas; Hensler, Samantha; Lang, Marina; Stratmann, Ansgar; Giesecke, Ulrich; Weuster-Botz, Dirk (2016): High-cell-density cultivation and recombinant protein production with *Komagataella pastoris* in stirred-tank bioreactors from milliliter to cubic meter scale. In *Process Biochemistry* 51 (2), pp. 177–184. DOI: 10.1016/j.procbio.2015.11.024.

Schmidt, S.; Havekost, D.; Kaiser, K.; Kauling, J.; Henzler, H.-J. (2005): Crystallization for the Downstream Processing of Proteins. In *Engineering in Life Sciences* 5 (3), pp. 273–276. DOI: 10.1002/elsc.200500116.

Shenoy, B.; Wang, Y.; Shan, W.; Margolin, A. L. (2001): Stability of crystalline proteins. In *Biotechnology and Bioengineering*. 73 (5), pp. 358–369. DOI: 10.1002/bit.1069.

Shimamura, Tatsuro; Nitani, Yasushi; Uchiyama, Takuro; Matsuzawa, Hiroshi (2009): Improvement of crystal quality by surface mutations of beta-lactamase Toho-1. In *Acta Crystallographica. Section F, Structural Biology and Crystallization Communications* 65 (Pt 4), pp. 379–382. DOI: 10.1107/S1744309109008240.

Shu, F.; Ramakrishnan, V.; Schoenborn, B. P. (2000): Enhanced visibility of hydrogen atoms by neutron crystallography on fully deuterated myoglobin. In *Proceedings of the National Academy of Sciences of the United States of America* 97 (8), pp. 3872–3877. DOI: 10.1073/pnas.060024697.

- Shukla, Abhinav A.; Thömmes, Jörg (2010): Recent advances in large-scale production of monoclonal antibodies and related proteins. In *Trends in Biotechnology* 28 (5), pp. 253–261. DOI: 10.1016/j.tibtech.2010.02.001.
- Siezen, R. J.; Fisch, M. R.; Slingsby, C.; Benedek, G. B. (1985): Opacification of gamma-crystalline solutions from calf lens in relation to cold cataract formation. In *Proceedings of the National Academy of Sciences of the United States of America* 82 (6), pp. 1701–1705. DOI: 10.1073/pnas.82.6.1701.
- Smejkal, Benjamin; Agrawal, Neeraj J.; Helk, Bernhard; Schulz, Henk; Giffard, Marion; Mechelke, Matthias et al. (2013b): Fast and scalable purification of a therapeutic full-length antibody based on process crystallization. In *Biotechnology and Bioengineering* 110 (9), pp. 2452–2461. DOI: 10.1002/bit.24908.
- Smejkal, Benjamin; Helk, Bernhard; Rondeau, Jean-Michel; Anton, Sabine; Wilke, Angelika; Scheyerer, Peter et al. (2013a): Protein crystallization in stirred systems-scale-up via the maximum local energy dissipation. In *Biotechnology and Bioengineering*. 110 (7), pp. 1956–1963. DOI: 10.1002/bit.24845.
- Sommer, Morten O. A.; Larsen, Sine (2005): Crystallizing proteins on the basis of their precipitation diagram determined using a microfluidic formulator. In *Journal of Synchrotron Radiation* 12 (Pt 6), pp. 779–785. DOI: 10.1107/S0909049505002621.
- Sommer, Ralf; Tscheliessnig, Anne; Satzer, Peter; Schulz, Henk; Helk, Bernhard; Jungbauer, Alois (2015): Capture and intermediate purification of recombinant antibodies with combined precipitation methods. In *Biochemical Engineering Journal* 93, pp. 200–211. DOI: 10.1016/j.bej.2014.10.008.
- St. Clair, Nancy L.; Navia, Manuel A. (1992): Cross-linked enzyme crystals as robust biocatalysts. In *Journal of the American Chemical Society*. 114 (18), pp. 7314–7316. DOI: 10.1021/ja00044a064.
- Sumner, J. B. (1926): The isolation and crystallization of the enzyme urease. In *Journal of Biological Chemistry* (69), pp. 435–441.
- Takakura, Tomoaki; Ito, Takaomi; Yagi, Shigeo; Notsu, Yoshihide; Itakura, Takashi; Nakamura, Takumi et al. (2006): High-level expression and bulk crystallization of recombinant *L*-methionine gamma-lyase, an anticancer agent. In *Applied Microbiology and Biotechnology* 70 (2), pp. 183–192. DOI: 10.1007/s00253-005-0038-2.
- van Driessche, Alexander E. S.; van Gerven, Nani; Bomans, Paul H. H.; Joosten, Rick R. M.; Friedrich, Heiner; Gil-Carton, David et al. (2018): Molecular nucleation mechanisms and control strategies for crystal polymorph selection. In *Nature* 556 (7699), pp. 89–94. DOI: 10.1038/nature25971.
- Vekilov, Peter G. (2010): Nucleation. In *Crystal Growth & Design* 10 (12), pp. 5007–5019. DOI: 10.1021/cg1011633.
- Vekilov, Peter G.; Chernov, Alexander A. (2003): The Physics of Protein Crystallization. In: *Solid State Physics*, vol. 57, pp. 1–147.
- Vekilov, Peter G.; Feeling-Taylor, Angela R.; Yau, Siu Tung; Petsev, Dimiter (2002): Solvent entropy contribution to the free energy of protein crystallization. In *Acta Crystallographica. Section D, Biological Crystallography* 58 (Pt 10 Pt 1), pp. 1611–1616. DOI: 10.1107/S0907444902014312.
- Winn, Martyn D.; Ballard, Charles C.; Cowtan, Kevin D.; Dodson, Eleanor J.; Emsley, Paul; Evans, Phil R. et al. (2011): Overview of the CCP4 suite and current developments. In *Acta Crystallographica. Section D, Biological Crystallography* 67 (Pt 4), pp. 235–242. DOI: 10.1107/S0907444910045749.

Wolberg, Michael; Hummel, Werner; Müller, Michael (2001): Biocatalytic Reduction of β,δ -Diketo Esters: A Highly Stereoselective Approach to All Four Stereoisomers of a Chlorinated β,δ -Dihydroxy Hexanoate. In *Chemistry – A European Journal*. 7 (21), pp. 4562–4571. DOI: 10.1002/1521-3765(20011105)7:21<4562::AID-CHEM4562>3.0.CO;2-4.

Yang, Mark X.; Shenoy, Bhama; Distler, Matthew; Patel, Reena; McGrath, Margaret; Pechenov, Sergey; Margolin, Alexey L. (2003): Crystalline monoclonal antibodies for subcutaneous delivery. In *Proceedings of the National Academy of Sciences of the United States of America* 100 (12), pp. 6934–6939. DOI: 10.1073/pnas.1131899100.

Younger, Andrew K. D.; Su, Peter Y.; Shepard, Andrea J.; Udani, Shreya V.; Cybulski, Thaddeus R.; Tyo, Keith E. J.; Leonard, Joshua N. (2018): Development of novel metabolite-responsive transcription factors via transposon-mediated protein fusion. In *Protein Engineering, Design & Selection: PEDS* 31 (2), pp. 55–63. DOI: 10.1093/protein/gzy001.

Zheng, Lei; Baumann, Ulrich; Reymond, Jean-Louis (2004): An efficient one-step site-directed and site-saturation mutagenesis protocol. In *Nucleic Acids Research* 32 (14), e115. DOI: 10.1093/nar/gnh110.

Zhou, X-X; Wang, Y-B; Pan, Y-J; Li, W-F (2008): Differences in amino acids composition and coupling patterns between mesophilic and thermophilic proteins. In *Amino Acids* 34 (1), pp. 25–33. DOI: 10.1007/s00726-007-0589-x.

Appendices

A. Material

In the following, all chemicals, consumables, buffers/solutions/gels, culture media, bacterial strains, proteins/DNA, primers, crystallization equipment, software, and commercial kits used in this work are listed.

Table A.1: List of chemicals.

Chemical	Product details	Provider
2-propanol	≥99.8% p.a., ACS, ISO	Carl Roth GmbH & Co. KG (Karlsruhe, Germany)
Acetic acid	ROTIPURAN ≥99%, p.a.	Carl Roth GmbH & Co. KG (Karlsruhe, Germany)
Acetophenone	puriss, p.a., ≥99.0% (GC)	Sigma-Aldrich (Deisenhofen, Germany)
Agar-agar	BioScienceGrade, powder	Carl Roth GmbH & Co. KG (Karlsruhe, Germany)
Agarose	Rotigarose for DNA/RNA electrophoresis	Carl Roth GmbH & Co. KG (Karlsruhe, Germany)
Ammonium peroxodisulfate (APS)	≥98%, p.a., ACS	Carl Roth GmbH & Co. KG (Karlsruhe, Germany)
Bromophenol	Sodium salt, for electrophoresis	Carl Roth GmbH & Co. KG (Karlsruhe, Germany)
CaCl₂	Dihydrate, ≥99%, p.a., ACS	Carl Roth GmbH & Co. KG (Karlsruhe, Germany)
Coomassie	brillant blue R250	Merck Millipore (Darmstadt, Germany)
Dimethyl Sulfoxide (DMSO)	>99.9%	New England Biolabs (Ipswich, USA)
Ethylenediaminetetraacetic acid (EDTA)	≥99 %, p.a.	Carl Roth GmbH & Co. KG (Karlsruhe, Germany)
Gel Loading Dye	Purple, 6x	New England Biolabs (Ipswich, USA)
Glucose monohydrate	D(+), >99.5%	Carl Roth GmbH & Co. KG (Karlsruhe, Germany)
Glycerin	ROTIPURAN, ≥99.5% p.a., water free	Carl Roth GmbH & Co. KG (Karlsruhe, Germany)
HCl	ACS Reagent, 37%	Honeywell (Bucharest, Romania)
HEPES	≥99.5%	Carl Roth GmbH & Co. KG (Karlsruhe, Germany)
Imidazole	PUFFERAN, ≥99%, p.a., Ultra Quality	Carl Roth GmbH & Co. KG (Karlsruhe, Germany)
IPTG	≥99%, for biochemistry	Carl Roth GmbH & Co. KG (Karlsruhe, Germany)
K₂HPO₄	pure EP	Labochem international (Heidelberg, Germany)
Kanamycin sulfate	≥750I.U./mg, for biochemistry	Carl Roth GmbH & Co. KG (Karlsruhe, Germany)

Chemical	Product details	Provider
KCl	≥99.5%, p.a., ACS, ISO	Carl Roth GmbH & Co. KG (Karlsruhe, Germany)
KH₂PO₄	Water free, ≥99.5%	Carl Roth GmbH & Co. KG (Karlsruhe, Germany)
MgCl₂	Hexahydrate, ≥99%	Carl Roth GmbH & Co. KG (Karlsruhe, Germany)
Midori Green	MIDORIGreen Advance	Nippon Genetics Europe GmbH (Düren, Germany)
MnCl₂	Tetrahydrate, ReagentPlus, ≥99%	Sigma-Aldrich (Deisenhofen, Germany)
Na₂HPO₄	Water free, ≥95%	Carl Roth GmbH & Co. KG (Karlsruhe, Germany)
NaCl	CELLPURE, ≥99.8%	Carl Roth GmbH & Co. KG (Karlsruhe, Germany)
NADPH	Tetrasodium salt, ≥97%	Carl Roth GmbH & Co. KG (Karlsruhe, Germany)
NaH₂PO₄	Dihydrate, pure, pharma grade	AppliChem GmbH (Darmstadt, Germany)
NaOH	Pellet, ≥98%	Carl Roth GmbH & Co. KG (Karlsruhe, Germany)
Peptone	from casein tryptic digest, for microbiology	Carl Roth GmbH & Co. KG (Karlsruhe, Germany)
Phenylmethylsulfonyl fluoride (PMSF)	≥99%	Carl Roth GmbH & Co. KG (Karlsruhe, Germany)
Polyethylene glycol (PEG) 550 MME	Poly(ethylene glycol) methyl ether, average Mn 550	Sigma-Aldrich (Deisenhofen, Germany)
Pure water	LC-MS Reagent	Carl Roth GmbH & Co. KG (Karlsruhe, Germany)
SDS running buffer	Rotiphorese 10X SDS-Page	Carl Roth GmbH & Co. KG (Karlsruhe, Germany)
Sodium acetate	≥99%, p.a., ACS, water free	Carl Roth GmbH & Co. KG (Karlsruhe, Germany)
Sodium lauryl sulfate (SDS)	SDS / sodium lauryl sulfate, ≥99%, for biochemistry	Carl Roth GmbH & Co. KG (Karlsruhe, Germany)
SYPRO Orange	Protein gel stain	Sigma-Aldrich (Deisenhofen, Germany)
TAE buffer	Rotiphorese 50x TAE Puffer	Carl Roth GmbH & Co. KG (Karlsruhe, Germany)
TEMED	≥98.5%	Carl Roth GmbH & Co. KG (Karlsruhe, Germany)
Tris base	≥99.9%	Carl Roth GmbH & Co. KG (Karlsruhe, Germany)
Tris-HCl	≥99%	Carl Roth GmbH & Co. KG (Karlsruhe, Germany)
Yeast extract	Gistex® Standard Powder AGGL	DMS Food Specialties (Delft, Netherland)
β-mercaptoethanol	≥99%	Carl Roth GmbH & Co. KG (Karlsruhe, Germany)

Table A.2: List of consumables.

Consumable	Product details	Provider
96 well hanging/sitting drop crystallization plate	ComboPlate, optionally with 45µL Crystalbridges	Jean Bioscience GmbH (Jena, Germany)
+ Crystalbridges for ComboPlates	45µL volume	Jean Bioscience GmbH (Jena, Germany)
+ Cover slides for CompoPlates	diameter 18 mm	Jean Bioscience GmbH (Jena, Germany)
+ Baysilon sealing grease	Highly viscous	GE Bayer Silicones GmbH & Co. KG (Leverkusen, Germany)
96 well batch crystallization plate	MRC Under Oil Crystallization Plate	Jean Bioscience GmbH (Jena, Germany)
Sealing tape for crystallization plates	Crystal Clear Duck Tape, 7.6 cm	Duck Brand (Avon, USA)
96 well microtiter plate	Flat bottom, Nunc	Thermo Fisher Scientific (Roskilde, DK)
Bottle top filter	Steritop Threaded Bottle Top Filter, 0.22 µm	Merck Millipore (Darmstadt, Germany)
Centrifugal concentrator	Vivaspin Turbo 15 and 500, 10,000 kDa MWCO	Sartorius Stedim Lab Ltd. (Stonehouse, UK)
Cultivation tubes	Tube 13 mL, 100 x 16 mm, PP	Sarstedt AG & Co. KG (Nürnberg, Germany)
Culture dishes	CELLSTAR® Cell Culture Dishes	Greiner Bio-One (Kremsmünster, Austria)
Cuvette for OD measurement	Ratiolab® CUVETTES Semi-Mirco, 1.6 mL, UV	Ratiolab GmbH (Dreieich, Germany)
Dialysis tubing	Membra-Cel, 34 mm, MWCO 14000	Carl Roth GmbH & Co. KG (Karlsruhe, Germany)
His Trap columns (1 mL, 5 mL)	His trap high performance histidine-tagged protein purification columns	GE Healthcare (Buckinghamshire, U.K.)
Optical PCR tubes and caps	8x Strip, 120 count	Agilent Technologies (Ditcot, U.K.)
Pipette tips (10 µL, 200 µL, 1 mL, 10 mL)	1.0 mm, 15-well	Brand (Wertheim, Germany)
Polypropylen tubes	15 mL, 50 mL	Greiner Bio-One (Frickenhausen, Germany)
Safe-lock tubes	(1,5 mL, 2 mL)	Eppendorf AG (Hamburg, Germany)

Table A.3: List of Buffers, solutions, and gels.

Buffer/Solution/Gel	Composition
Agarose gel	1 g agarose
	100 mL TAE buffer
Crystallization buffer	0.1 M Tris-HCl, pH 7.0
	25–200 g L ⁻¹ PEG 550 MME
	25–100 mM MgCl ₂
	Filtration (0.2 µm)
Dissolution buffer	Protein buffer + 1 M MgCl ₂

Buffer/Solution/Gel	Composition
Fairbanks A	250 mL L ⁻¹ 2-propanol
	0.5 g L ⁻¹ Coomassie Brilliant blue
	100 mL L ⁻¹ acetic acid
Fairbanks B	100 mL L ⁻¹ 2-propanol
	0.5 g L ⁻¹ Coomassie Brilliant blue
	100 mL L ⁻¹ acetic acid
IMAC Binding buffer	500 mM NaCl
	20 mM NaH ₂ PO ₄ /Na ₂ HPO ₄
	40 mM imidazole
	pH 7.5 with HCl
	Filtration (0.22 µm)
IMAC Elution buffer	500 mM NaCl
	20 mM NaH ₂ PO ₄ /Na ₂ HPO ₄
	500 mM Imidazole
	pH 7.5 with HCl
	Filtration (0.22 µm)
Laemmli (5x)	10% (w/v) SDS
	50% (v/v) glycerin
	300 mM Tris-HCl
	β-mercaptoethanol
	0.05% (w/v) bromophenol
Mastermix for enzymatic activity assay	20 mM HEPES, pH 7.0
	1 mM MgCl ₂
	0.5 mM NADPH
	10 mM Acetophenone
Phosphate-buffered saline (PBS) (10x)	80 g L ⁻¹ NaCl
	2 g L ⁻¹ KCl
	14.4 g L ⁻¹ Na ₂ HPO ₄
	2.4 g L ⁻¹ KH ₂ PO ₄
	pH 7.4 adjustment by adding 1 M NaOH
Protein/Dialysis buffer	20 mM HEPES
	1 mM MgCl ₂
	pH 7.0 with 1 M NaOH
SDS Collecting gel	87.5 mL L ⁻¹ (Bis-)acrylamide solution
	500 mL L ⁻¹ 2x collecting gel
	0.5 M Tris; 4 g L ⁻¹ SDS; pH 6.8
	dye with bromophenol
	5 mL L ⁻¹ APS solution (100 g L ⁻¹)
	500 µL L ⁻¹ TEMED

Appendices

Buffer/Solution/Gel	Composition
SDS Separating gel	312.5 mL L ⁻¹ (Bis-)acrylamide solution
	250 mL L ⁻¹ 4x separating buffer
	(1.5 M Tris; 8 g L ⁻¹ SDS; pH 8.8)
	2.5 mL L ⁻¹ APS solution (100 g L ⁻¹)
Solution I for competent cells	250 µL L ⁻¹ TEMED
	10 mM sodium acetate
	50 mM MnCl ₂
	5 mM NaCl
Solution II for competent cells	Sterile filtration (ø 0.2 µm)
	10 mM NaAc
	5% (w/v) glycerin
	70 mM CaCl ₂
Solution II for competent cells	5 mM MnCl ₂
	Sterilization: 30 min at 121°C and 2 bar

Table A.4: List of culture media.

Culture media	Composition
LB medium	5 g L ⁻¹ yeast extract
	10 g L ⁻¹ peptone from casein
	5 g L ⁻¹ NaCl
	pH adjusted to 7.4 with NaOH
	Sterilization: 30 min at 121°C and 2 bar
LB agar	LB medium
	15 g L ⁻¹ agar-agar
	Sterilization: 30 min at 121°C and 2 bar
SOC Medium	5 g L ⁻¹ yeast extract
	20 g L ⁻¹ tryptone
	0.6 g L ⁻¹ NaCl
	Sterilization: 30 min at 121°C and 2 bar
	20 mM Glucose (sterile filtrated, ø 0.2 µm)
TB Medium	10 mM MgCl ₂ (sterile filtrated, ø 0.2 µm)
	10 mM MgSO ₄ (sterile filtrated, ø 0.2 µm)
	24 g L ⁻¹ yeast extract
	12 g L ⁻¹ peptone from casein
	5 g L ⁻¹ glycerin
	Sterilization: 30 min at 121°C and 2 bar
	17 mM KH ₂ PO ₄ (sterile filtrated, ø 0.2 µm)
72 mM K ₂ HPO ₄ (sterile filtrated, ø 0.2 µm)	

Culture media	Composition
Riesenberg medium (Riesenberg <i>et al.</i> 1991)	
	13,3 g L ⁻¹ KH ₂ PO ₄
	4 g L ⁻¹ (NH ₄) ₂ HPO ₄
	1,7 g L ⁻¹ citric acid
	pH adjusted to 7.4 with KOH
	Supplements
	25 g L ⁻¹ Glucose * H ₂ O
	1,2 g L ⁻¹ MgSO ₄ * 7 H ₂ O
	1 mL L ⁻¹ Antifoam 204
	Thiamin-HCL (1 M) (1000x)
	1 mL L ⁻¹ trace element solution
	Trace element solution
	0,125 g L ⁻¹ CoCl ₂ · 6 H ₂ O
	0,75 g L ⁻¹ MnCl ₂ · 4 H ₂ O
	0,075 g L ⁻¹ CuCl ₂ · 2 H ₂ O
	0,15 g L ⁻¹ H ₃ BO ₃
	0,125 g L ⁻¹ Na ₂ MoO ₄ · 2 H ₂ O
	0,42 g L ⁻¹ EDTA
	0,4 g L ⁻¹ Zn(CH ₃ COO) ₂ · 2 H ₂ O
	3 g L ⁻¹ Fe(III)citrate

Table A.5: List of bacterial strains.

Bacterial strain	Genotype
<i>E. coli</i> BL21(DE3)	B F-ompT gal dcm lon hsdSB(rB-mB-) λ(DE3 [lacI lacUV5- T7p07 ind1 sam7 nin5]) [malB ⁺]K-2(λS)
<i>E. coli</i> DH5α	F ⁻ Φ80lacZΔM15 Δ(lacZYA-argF) U169 recA1 endA1 hsdR17 (rK ⁻ , mK ⁺) phoA supE44 λ ⁻ thi-1 gyrA96 relA1

Table A.6: List of proteins and DNA.

Protein/DNA	Product details	Provider
2log DNA Marker	0.1-10.0 kb	New England Biolabs (Ipswich, USA)
DNase	Deoxyribonuclease I from bovine pancreas lyophilized powder, Protein ≥85%, ≥400 U/mg protein	Sigma-Aldrich (Deisenhofen, Germany)
Deoxynucleotide (dNTP) Solution Mix	10 mM each	New England Biolabs (Ipswich, USA)
DNA plasmid	pET-28a(+)	Novagen, Merck Millipore (Darmstadt, Germany)
DpnI	20,000 U/mL	New England Biolabs (Ipswich, USA)
HindIII	100,000 U/mL	New England Biolabs (Ipswich, USA)

Appendices

Protein/DNA	Product details	Provider
Justblue Protein Marker	Prestained Protein Marker	NIPPON Genetics Europe (Düren, Germany)
Lysozyme	>35,000 FTP U/mg	Carl Roth GmbH & Co. KG (Karlsruhe, Germany)
NcoI	50,000 U/mL	New England Biolabs (Ipswich, USA)
Phusion High-Fidelity DNA Polymerase	2,000 U/mL	New England Biolabs (Ipswich, USA)
T4 DNA Ligase	400,000 U/mL	New England Biolabs (Ipswich, USA)

Table A.7: List of primers.

Mutation	Forward primer (5' - 3')	Reverse primer (5' - 3')
L16W	GTGGTACGTGGGTATCGGTTTAGC	GATACCCACGTACCACCTGTAATG
E28A	GTTCTGTCAGAAAGGGGCTAAG	CCTTCGCAACGAACTTCGTGGC
K32A	GGGCTGCGGTCATGATTACC	CATGACCGCAGCCCCCTTCTTC
R38A	GATTACCGGCGCGCACAGCGATGTTGGTGAAAAAG	CAACATCGCTGTGCGCGCCGGTAATCATGACC
H39A	GGCCGGGCCAGCGATGTTGGTGAAAAAG	CAACATCGCTGGCCCGCCGGTAATCATG
H39D	CGGGACAGCGATGTTGGTG	GCTGTCCCGCCGGTAATC
H39E	CGGGAGAGCGATGTTGGTG	GCTCTCCCGCCGGTAATC
H39F	GGCCGGTTCAGCGATGTTGGTGAAAAAGCAGC	CGCTGAACCGCCGGTAATCATGACCTTAGC
H39Y	CCGGTACAGCGATGTTGGTG	GCTGTACCGCCGGTAATC
H39W	CATCGCTCCACCGCCGGTAATCATGAC	GGCCGGTTCAGCGATGTTGGTGAAAAAGCAGC
D41A	CAGCGCTGTGGTGAAAAAGC	CAACAGCGCTGTGCCGGC
D41F	GGCACAGCTTCGTGGTGAAAAAGCAGCTAAG	CTTTTACCAACGAAGCTGTGCCGGCCG
E44A	GTTGGTGAAAAGCAGCTAAG	GCTGCTTTTGACCAACATCG
K45A	GATGTTGGTGAAGCAGCAGCTAAGAGTGTCG	CTTAGTGCTGCTTACCAACATCGCTGTG
K45F	GGTGAATTCGCAGCTAAGAGTGTCGGCACTC	GCTGCGAATTCACCAACATCGCTGTGCCGG
K45R	GAAAGAGCAGCTAAGAGTGTCGGC	GCTGCTCTTTCACCAACATCGC
K45Y	GGTGAATATGCAGCTAAGAGTGTCGGC	GCTGCATATTCACCAACATCGCTGTG
K45W	GTTGGTGAATGGGCAGCTAAGAGTGTCGGC	CTTAGTGCCATTACCAACATCGCTGTG
K48A	GCAGCTGCGAGTGTCGGCACTC	AGCCACTCGCAGCTGCTTTTTTC
K48R	GCAGCTAGGAGTGTCGGCAC	GACACTCTAGCTGCTTTTTTCACC
T52A	GAGTGTCGGCGCTCCTGATCAGATTC	CAGGAGCGCCGACACTCTTAGCTG
D54A	CACTCCTGCTCAGATTCAATTTTTCC	GAATCTGAGCAGGAGTGCCGACACTC
D54C	CACTCCTGTGCAGATTCAATTTTTCC	GAATCTGACAAGGAGTGCCGACACTC
D54E	CACTCCTGAGCAGATTCAATTTTTCC	GAATCTGCTCAGGAGTGCCGACACTC
D54F	CACTCCTTCCAGATTCAATTTTTCC	GAATCTGAAAAGGAGTGCCGACAC
D54G	CACTCCTGGTCAGATTCAATTTTTCC	GAATCTGACCAGGAGTGCCGACACTC
D54H	CACTCCTCATCAGATTCAATTTTTCC	GAATCTGATGAGGAGTGCCGACACTC
D54I	CACTCCTATTCAGATTCAATTTTTCC	GAATCTGAATAGGAGTGCCGACACTC
D54K	CACTCCTAAACAGATTCAATTTTTCC	GAATCTGTTTAGGAGTGCCGACAC

Mutation	Forward primer (5' - 3')	Reverse primer (5' - 3')
D54L	CACTCCTCTGCAGATTCAATTTTTCC	GAATCTGCAGAGGAGTGCCGACACTC
D54M	CACTCCTATGCAGATTCAATTTTTCC	GAATCTGCATAGGAGTGCCGACACTC
D54N	CACTCCTAATCAGATTCAATTTTTCC	GAATCTGATTAGGAGTGCCGACACTC
D54P	CACTCCTCCGCAGATTCAATTTTTCC	GAATCTGCGGAGGAGTGCCGACACTC
D54Q	CACTCCTCAGCAGATTCAATTTTTCC	GAATCTGCTGAGGAGTGCCGACACTC
D54R	CACTCCTCGTCAGATTCAATTTTTCC	GAATCTGACGAGGAGTGCCGACAC
D54S	CACTCCTTCTCAGATTCAATTTTTCC	GAATCTGAGAAGGAGTGCCGACACTC
D54T	CACTCCTACCCAGATTCAATTTTTCC	GAATCTGGGTAGGAGTGCCGACACTC
D54V	CACTCCTGTGCAGATTCAATTTTTCC	GAATCTGCACAGGAGTGCCGACACTC
D54W	CACTCCTGGCAGATTCAATTTTTCC	GAATCTGCCAAGGAGTGCCGACACTC
D54Y	CACTCCTTATCAGATTCAATTTTTCC	GAATCTGATAAGGAGTGCCGACAC
Q55A	CTCCTGATGCGATTCAATTTTTCCAAC	GAATCGCATCAGGAGTGCCGACAC
Q55E	CTCCTGATGAGATTCAATTTTTCCAAC	GAATCTCATCAGGAGTGCCGACAC
D65Y	CTTCCTATGAAGACGGCTGG	CGTCTTCATAGGAAGAATCATG
E66D	CCGATGATGACGGCTGGACG	CCAGCCGTCATCATCGGAAGAATC
E66F	CCGATTTTCGACGGCTGGACGAAATTATTCGATGC	CCGTCGAAATCGGAAGAATCATGTTGGAAAAATTG
E66W	CCGATTTGGACGGCTGGACGAAATTATTCG	CCGTCCAATCGGAAGAATCATGTTGG
D67A	CTCCGATGAAGCGGGCTGGACGAAATTATTC	GTCCAGCCCCTTCATCGGAAGAATCATGTTG
T70F	CGGCTGGTTCAAATTATTCGATGCAACGGAAAAAG	CATCGAATAATTTGAACCAGCCGCTTTCATCG
K71A	GACGGCATTATTCGATGCAACG	GAATAATGCCGTCCAGCCGTC
K71H	GGACGCATTATTCGATGCAACGG	CGAATAAATGCGTCCAGCCGTC
K71F	GGCTGGACGTTTTTATTCGATGCAACGG	CGAATAAAAACGTCCAGCCGCTTTCATC
K71R	GGACGAGATTATTCGATGCAACGG	CGAATAATCTCGTCCAGCCGTC
D74E	CGAAATTATTCGAAGCAACGGAAAAAGC	CCGTTGCTTCGAATAATTTCTGTC
F80A	CGGAAAAAGCCGCTGGCCAGTTTC	GCCAGCGGCTTTTTCCGTTGCATCG
E100A	CAAGAGTGTGGAAGCGACCACGACTGCTGAATG	GTCGTGGTCTGCTCGACACTCTGTGAACCG
T102E	GAAACCGAGACTGCTGAATGGC	GCAGTCTCGGTTTCTTCGACAC
T103D	GAAACCGAGACTGCTGAATGGC	GCATCCGTGTTTCTTCGACAC
T103F	CCACGTTTGCTGAATGGCGTAAATTATTAG	CCATTCAGCAAACGTGGTTTCTTCG
R122F	CTTCGGTACCTTCTTAGGATTCAACGGATG	GAATCCCTAAGAAGGTACCGAAGAAGACACC
R122W	CGGTACCTGGTTAGGATTCAACGGATG	CCCTAACCGGTACCGAAGAAGACACC
Q126F	GGGATTTCCGGATGAAGAACAAAGGCTTAG	GTTCTTCATCCGGAAAAATCCCTAATCGGGTAC
Q126H	GGATTCATCGGATGAAGAACAAAGGC	CGATGAATCCCTAATCGGGTACCG
Q126K	GGATTAACCGATGAAGAACAAAGGC	CGTTTAATCCCTAATCGGGTACCG
R127A	GATTCAAGCGATGAAGAACAAAGGCTTAGGG	CTTCATCGCTTGAATCCCTAATCGGGTACC
R127F	GGATTCAATTTATGAAGAACAAAGGCTTAG	CTTCATAAATTGAATCCCTAATCGGGTAC
R127Y	GGGATTCATATATGAAGAACAAAGGCTTAGG	CTTCATATATTGAATCCCTAATCGGGTACCG
D197E	GGTTGATGAACTACCAGGGGCC	CCTGGTAGTTCATCAACCAATGGTG
D197F	GGTTGATTTTCTACCAGGGGCCGAAGAA	GTAGAAAATCAACCAATGGTGTCTTGATGTAGCC

Appendices

Mutation	Forward primer (5' - 3')	Reverse primer (5' - 3')
D197H	GTTGATCACCTACCAGGGGCCGAAGAAGCG	GGTAGGTGATCAACCAATGGTGTCTTGATGTAGCC
D197W	GGTTGATTGGCTACCAGGGGCCGAAGAA	GGTAGCCAATCAACCAATGGTGTCTTGATGTAGC
D197Y	TGGTTGATTATCTACCAGGGGCCGAAGAAG	CTGGTAGATAATCAACCAATGGTGTCTTGATGTAG
Q207D	CGATGTCAGATCGGACCAAGACGCCAATG	CTGGTCCGATCTGACATCGCTTCTTCG
Q207E	CGATGTCAGAACGGACCAAGACGCCAATG	CTGGTCCGTTCTGACATCGCTTCTTCG
Q207F	CGATGTCATTCCGGACCAAGACGCCAATG	CTGGTCCGAATGACATCGCTTCTTCG
Q207W	CGATGTCATGGCGGACCAAGACGCCAATG	CTGGTCCGCCATGACATCGCTTCTTCG
Q207Y	CGATGTCATACCGGACCAAGACGCCAATG	CTGGTCCGGTATGACATCGCTTCTTCG

Table A.8: List of crystallization equipment.

Equipment	Product details	Provider
<i>μL-scale</i>		
Camera	DS-2Mv; No. MQA12000 or DS-Fi3; No. MQA18000	Nikon Instruments Europe BV (Amsterdam, The Netherlands)
Dual video port module	Y-IDP; No. MBB74105	Nikon Instruments Europe BV (Amsterdam, The Netherlands)
Incubator (20°C)	Kb115	Binder (Tuttlingen, Germany)
Lens A	Plan Chromat 4x/ 0.10; No. MRL00042	Nikon Instruments Europe BV (Amsterdam, The Netherlands)
Lens B	Plan Fluor 10x / 0.3; No. MRH00101	Nikon Instruments Europe BV, (Amsterdam, The Netherlands)
Microscope	Eclipse 50i/ No. MBA85020	Nikon Instruments Europe BV (Amsterdam, The Netherlands)
<i>mL-scale</i>		
Power adapter	72W power adapter (24V 3A)	Salcar GmbH (Leipzig, Germany)
DC cable	with switch DCKSW	Sertronics GmbH (Berlin, Germany)
Jack adapter	2.1 * 5.5 mm	Foxonov (Shenzhen, China)
Microcontroller	Arduino UNO Rev 3	Arduino
Protoboard	TW-E40-1020	Twins Industry (Munich, Germany)
Screw board	Adafruit Proto-Screw shield for Arduino	Adafruit (New York, USA)
Stepper motor driver	Big easy driver	SparkFun Electronics (Niwtot, France)
Stepper motor	ST2818L1006-B	Nanotech (Feldkirchen, Germany)

Table A.9: List of software

Software	Version	Provider
Arduino	1.8.10	Arduino LLC
ChemDraw	19.0	PerkinElmer
GelAnalyzer	19.1	Istvan Lazar Jr.
GenomeCompiler		www.genomecompiler.com

Software	Version	Provider
NIS Elements Advanced Research	3.22.15	Nikon Instruments Europe BV
Origin	2020	OriginLab Corporation
Office 365	2016	Microsoft
Unicorn	3	GE Healthcare Life Science
PyMol	2.1	Schroedinger
ProtParam		web.expasy.org/protparam
Skanit Software	3.1, Research Edition for Multiskan FC	Thermo Fischer Scientific GmbH (Munich, Germany)
TA Instruments Advantage	5.5.24	TA Instruments Inc (Delaware, USA)

Table A.10: List of commercial kits

Kit	Product details	Provider
BCA Assay	Pierce BCA Protein Assay Kit	ThermoFischer Scientific GmbH (Munich, Germany)
HCP-ELISA	<i>E. coli</i> BL21 360, Type D	BioGenes GmbH (Berlin, Germany)
PCR product preparation	FastGene Gel/PCR Extraction Kit	Nippon Genetics Europe GmbH (Düren, Germany)
Plasmid preparation	FastGene Plasmid Mini Kit	NIPPON Genetics Europe (Düren, Germany)

B. Arduino script

This script was used to control the stirrer speed in the mL-crystallizers.

```
//Declare pin functions on Arduino
#define stp 2 //Step pin
#define dir 3 //Direction pin
#define MS1 4
#define MS2 5
#define MS3 6
#define EN 7

//Main section
void setup() {
  pinMode(stp, OUTPUT);
  pinMode(dir, OUTPUT);
  pinMode(MS1, OUTPUT);
  pinMode(MS2, OUTPUT);
  pinMode(MS3, OUTPUT);
  pinMode(EN, OUTPUT);
  digitalWrite(EN, LOW);
  digitalWrite(dir, LOW);
  digitalWrite(MS1, HIGH);
  digitalWrite(MS2, HIGH);
  digitalWrite(MS3, HIGH);
  Serial.begin(9600); //Open Serial connection for debugging
}

void loop() {
  digitalWrite(stp,HIGH); //Trigger one step forward
  delayMicroseconds(62); //Delay between high and low state. This determines rotation speed
  digitalWrite(stp,LOW); //Pull step pin low so it can be triggered again
  delayMicroseconds(62); //Delay between high and low state. This determines rotation speed
}
```


D. Crystallization microphotographs

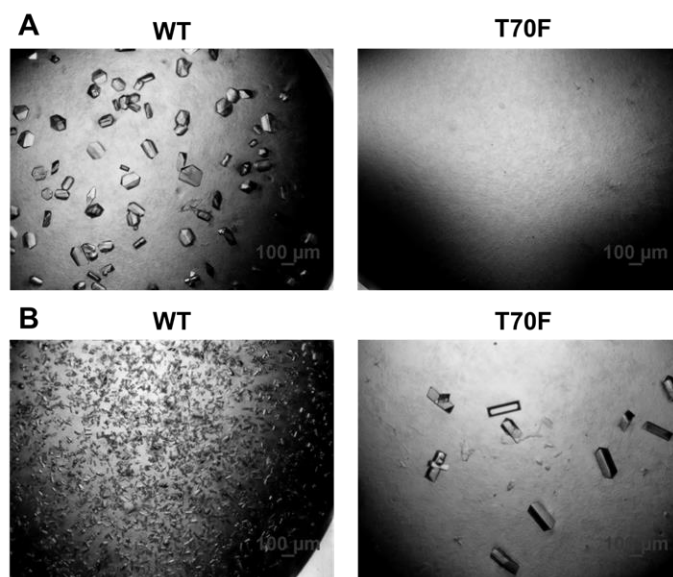


Figure D.1: Crystallization microphotographs of *LbADH* WT and mutant T70F at two different PEG concentrations (μL -scale). (A) Crystallization with 5 g L^{-1} *LbADH* and 75 g L^{-1} PEG and (B) with 5 g L^{-1} *LbADH* and 87.5 g L^{-1} PEG. Microphotographs were taken after 24 h.

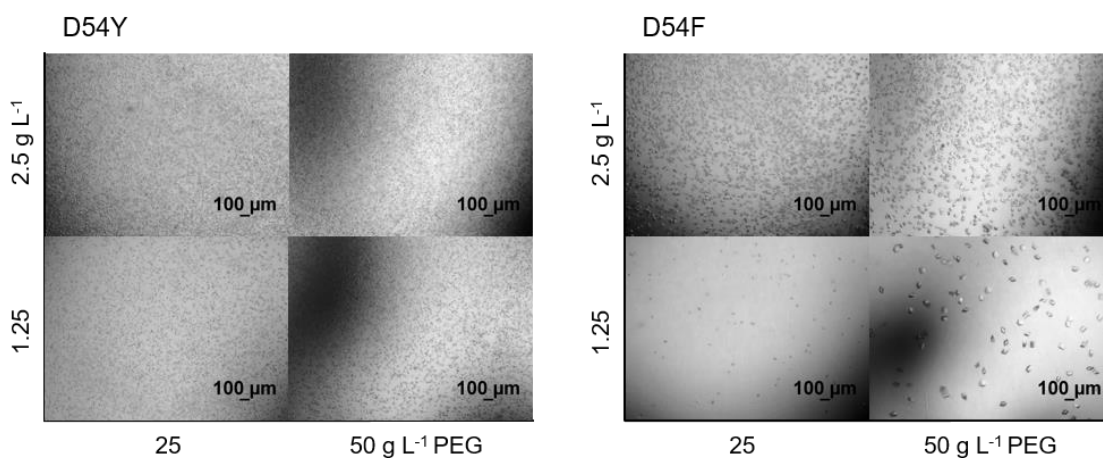


Figure D.2: Crystallization microphotographs of *LbADH* single mutants D54Y and D54F illustrating comparable crystallization behavior (μL -scale). Microphotographs were taken after 24 h.

E. Enzymatic activities

Table E.1: Relative maximum enzymatic activities (in %) of *Lb*ADH mutants compared to the WT activity. V_{\max} of *Lb*ADH WT is $24.9 \pm 3.0 \text{ U mg}^{-1}$ (10 mM acetophenone, 0.5 mM NADPH; T = 25 °C; pH = 7.0). Standard deviations were calculated from triplicate measurements or three biological replicates.

<i>Lb</i> ADH mutant	Enzymatic activity, %	<i>Lb</i> ADH mutant	Enzymatic activity, %
L16W_T70F	104.7 ±13.5	D54Q	101.8 ±6.0
E28A	58.1 ±15.3	D54R	108.6 ±0.2
K32A	118.2 ±5.5	D54S	84.8 ±6.4
K32A_Q126K	102.0 ±5.0	D54T	83.6 ±3.7
K32A_T102E	89.3 ±3.5	D54V	91.2 ±1.2
K32A_Q126H	71.1 ±8.9	D54W	90.6 ±2.6
R38A	9.9 ±1.9	D54Y	62.0 ±2.9
H39A	121.0 ±20.9	D54Y_Q126H	33.6 ±2.9
H39D	144.7 ±6.8	D54Y_Q126K	43.4 ±2.9
H39E	169.5 ±59.1	E66D	57.9 ±11.9
H39F	75.0 ±23.3	E66F	32.9 ±12.7
H39W	48.2 ±10.1	E66W	64.5 ±6.6
D41A	60.0 ±10.2	D67A	33.9 ±2.5
D41F	75.1 ±5.9	T70F	106.5 ±6.4
D41F_Q126F	78.3 ±13.6	K71A	88.9 ±4.2
E44A	67.2 ±5.1	K71H	70.0 ±5.6
K45A	97.5 ±6.0	K71R	76.4 ±5.0
K45R	76.5 ±2.9	D74E	83.5 ±4.3
K45W_T103F	3.6 ±3.1	E100A	72.5 ±10.2
K45W_R122F	0.0 ±0.1	T103F_R122F	1.8 ±0.1
K45W_R122W	0.0 ±0.1	T102E	103.1 ±2.4
K45Y_R122F	0.5 ±0.3	T102E_Q126H	71.7 ±1.7
K48A*	108.5 ±4.4	T102E_Q126K	77.3 ±2.3
K48R	88.2 ±7.4	T103D	3.7 ±0.6
D54A	111.2 ±5.6	T103F	50.9 ±3.7
D54C	47.5 ±1.8	R122F	1.0 ±0.1
D54E	116.4 ±2.7	R122W	0.0 ±0.2
D54F	98.3 ±7.1	Q126F	96.2 ±17.9
D54F_T102E	69.3 ±1.5	Q126H	80.8 ±5.3
D54F_Q126H	73.1 ±5.2	Q126K	95.1 ±6.8
D54F_Q126K	104.3 ±3.3	D197A	40.8 ±4.6
D54G	84.1 ±3.2	D197E	89.5 ±1.8
D54H	95.2 ±6.3	D197F	14.0 ±7.5
D54I	82.6 ±3.5	D197W	8.3 ±5.3
D54K	n.a.	Q207D	32.2 ±0.3
D54L	86.8 ±3.3	Q207E	48.2 ±2.9
D54M	113.8 ±8.2	Q207F	6.7 ±1.4
D54N	96.6 ±7.5	Q207W	3.1 ±0.6
D54P	94.0 ±10.6	Q207Y	4.7 ±0.4

F. Stability measurements

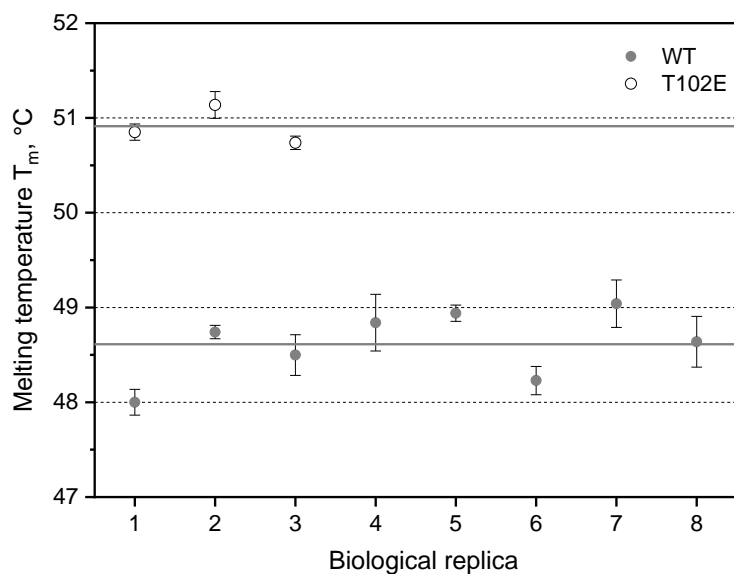


Figure F.1: Melting temperatures (T_m) of three and eight biological replicates for *LbADH* mutant T102E and WT, respectively, demonstrating the high reproducibility of the TSA. A thermal gradient was applied from 25–95 °C. SYPRO Orange was used as fluorescent dye (λ_{ex} 492 nm / λ_{em} 568 nm). Grey solid lines depict the mean of both variants.

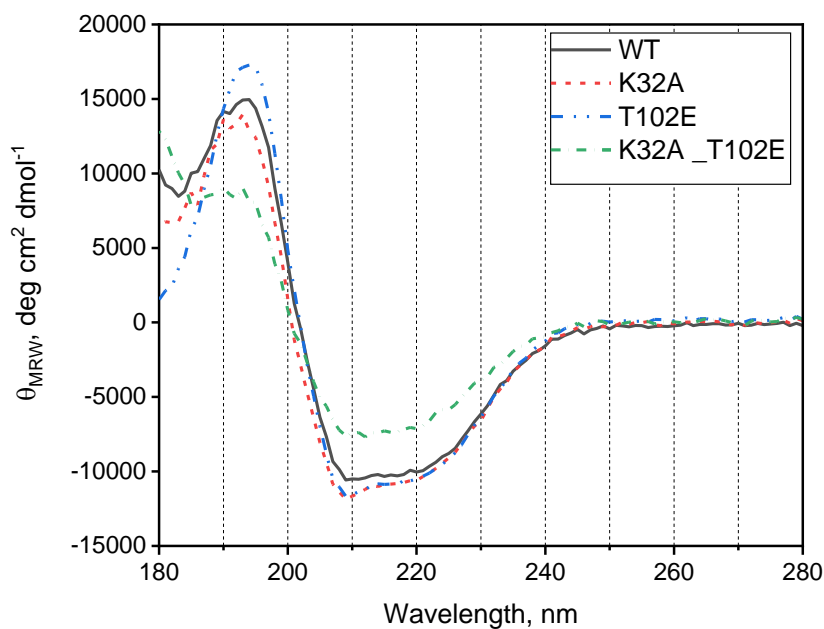


Figure F.2: CD spectra of *LbADH* WT and the single mutant K32A and T102E. Measurements were conducted with protein, which was stored at 30 days at 20 °C. Far UV range of 180–280 nm was measured ten times per sample and results were averaged.

G. Crystallization screens

Table G.1: Evaluation of the MPD crystallization screening. Crystals were counted after 24h. '+' refers to a higher crystal number of *Lb*ADH mutant T102E, '-' refers to higher crystal number of *Lb*ADH WT. Blank space indicates that neither of the two variants crystallized.

#	Salt	Buffer	Precipitant	+/-	WT crystals	T102E crystals
1	0.2M Cadmium chloride		40%(v/v) MPD	+	10	20
2	0.2M Potassium fluoride		40%(v/v) MPD	+	2	20
3	0.2M Ammonium fluoride		40%(v/v) MPD			
4	0.2M Lithium chloride		40%(v/v) MPD		-	
5	0.2M Magnesium chloride		40%(v/v) MPD		-	
6	0.2M Sodium chloride		40%(v/v) MPD		-	
7	0.2M Calcium chloride		40%(v/v) MPD			
8	0.2M Potassium chloride		40%(v/v) MPD		-	
9	0.2M Ammonium chloride		40%(v/v) MPD		-	
10	0.2M Sodium iodide		40%(v/v) MPD			
11	0.2M Potassium iodide		40%(v/v) MPD	+	1	50
12	0.2M Ammonium iodide		40%(v/v) MPD	+	5	20
13	0.2M Sodium thiocyanate		40%(v/v) MPD	+	3	20
14	0.2M Potassium thiocyanate		40%(v/v) MPD	+	6	20
15	0.2M Lithium nitrate		40%(v/v) MPD	+	5	12
16	0.2M Magnesium nitrate		40%(v/v) MPD			
17	0.2M Sodium nitrate		40%(v/v) MPD	-	100	50
18	0.2M Potassium nitrate		40%(v/v) MPD			
19	0.2M Ammonium nitrate		40%(v/v) MPD	+	1	30
20	0.2M Zinc sulfate		40%(v/v) MPD	+	0	30
21	0.2M Sodium formate		40%(v/v) MPD	+	2	20
22	0.2M Potassium formate		40%(v/v) MPD			
23	0.2M Ammonium formate		40%(v/v) MPD			
24	0.2M Lithium acetate		40%(v/v) MPD			
25	0.2M Magnesium acetate		40%(v/v) MPD			
26	0.2M Sodium malonate		40%(v/v) MPD			
27	0.2M Sodium acetate		40%(v/v) MPD			
28	0.2M Calcium acetate		40%(v/v) MPD			
29	0.2M Potassium acetate		40%(v/v) MPD			
30	0.2M Ammonium acetate		40%(v/v) MPD			
31	0.2M Lithium sulfate		40%(v/v) MPD	+	3	20
32	0.2M Magnesium sulfate		40%(v/v) MPD			
33	0.2M Cesium chloride		40%(v/v) MPD			
34	0.2M Nickel chloride		40%(v/v) MPD			
35	0.2M Ammonium sulfate		40%(v/v) MPD			
36	0.2M di-Sodium tartrate		40%(v/v) MPD			
37	0.2M K/Na tartrate		40%(v/v) MPD			
38	0.2M di-Ammonium tartrate		40%(v/v) MPD			
39	0.2M Sodium phosphate		40%(v/v) MPD			
40	0.2M Potassium bromide		40%(v/v) MPD			
41	0.2M Sodium bromide		40%(v/v) MPD	+	5	30
42	0.2M di-Potassium phosphate		40%(v/v) MPD	+	2	50
43	0.2M Ammonium phosphate		40%(v/v) MPD			
44	0.2M di-Ammonium phosphate		40%(v/v) MPD			
45	0.2M tri-Lithium citrate		40%(v/v) MPD			
46	0.2M tri-Sodium citrate		40%(v/v) MPD			

Appendices

#	Salt	Buffer	Precipitant	+/-	WT crystals	T102E crystals
47	0.2M tri-Potassium citrate		40%(v/v) MPD			
48	0.18M tri-Ammonium citrate		40%(v/v) MPD			
49		0.1M Citric acid pH 4	10%(v/v) MPD			
50		0.1M Sodium acetate pH 5	10%(v/v) MPD			
51		0.1M MES pH 6	10%(v/v) MPD			
52		0.1M HEPES pH 7	10%(v/v) MPD			
53		0.1M Tris pH 8	10%(v/v) MPD			
54		0.1M Bicine pH 9	10%(v/v) MPD			
55		0.1M Citric acid pH 4	20%(v/v) MPD			
56		0.1M Sodium acetate pH 5	20%(v/v) MPD			
57		0.1M MES pH 6	20%(v/v) MPD			
58		0.1M HEPES pH 7	20%(v/v) MPD			
59		0.1M Tris pH 8	20%(v/v) MPD			
60		0.1M Bicine pH 9	20%(v/v) MPD			
61		0.1M Citric acid pH 4	40%(v/v) MPD			
62		0.1M Sodium acetate pH 5	40%(v/v) MPD	+	0	30
63		0.1M MES pH 6	40%(v/v) MPD	-	1000	200
64		0.1M HEPES pH 7	40%(v/v) MPD			
65		0.1M Tris pH 8	40%(v/v) MPD			
66		0.1M Bicine pH 9	40%(v/v) MPD			
67		0.1M Sodium acetate pH 4	65%(v/v) MPD			
68		0.1M Sodium acetate pH 5	65%(v/v) MPD	+	0	20
69		0.1M MES pH 6	65%(v/v) MPD			
70		0.1M HEPES pH 7	65%(v/v) MPD			
71		0.1M Tris pH 8	65%(v/v) MPD			
72		0.1M Bicine pH 9	65%(v/v) MPD			
73	0.1 M tri-Sodium citrate	0.1 M HEPES sodium salt pH 7.5	10% (w/v) MPD			
74	0.05 M Magnesium chloride	0.1 M Tris-HCl pH 8.5	12% (w/v) MPD			
75	0.02 M Calcium chloride	0.1 M Sodium acetate pH 4.6	15% (w/v) MPD			
76		0.1 M Imidazole-HCl pH 8.0	15% (w/v) MPD; 5% (w/v) PEG 4000			
77	0.2 M Ammonium acetate	0.1 M tri-Sodium citrate pH 5.6	15% (w/v) MPD			
78	0.2 M Magnesium acetate	0.1 M MES sodium salt pH 6.5	15% (w/v) MPD			
79	0.2 M tri-Sodium citrate	0.1 M HEPES sodium salt pH 7.5	15% (w/v) MPD			
80	0.1 M tri-Sodium citrate	0.1 M HEPES sodium salt pH 7.5	20% (w/v) MPD			
81		0.1 M Imidazole-HCl pH 8.0	20% (w/v) MPD			
82	0.2 M Sodium chloride		20% (w/v) MPD; 4% (w/v) Glycerol			
83	0.02 M Calcium chloride	0.1 M Sodium acetate pH 4.6	30% (w/v) MPD	+	0	15
84	0.2 M Ammonium acetate	0.1 M tri-Sodium citrate pH 5.6	30% (w/v) MPD			
85	0.2 M Magnesium acetate	0.1 M MES sodium salt pH 6.5	30% (w/v) MPD			
86	0.5 M Ammonium sulfate	0.1 M HEPES sodium salt pH 7.5	30% (w/v) MPD			
87	0.2 M tri-Sodium citrate	0.1 M HEPES sodium salt pH 7.5	30% (w/v) MPD			
88		0.1 M HEPES sodium salt pH 7.5	30% (w/v) MPD; 5% (w/v) PEG 4000	+	0	40
89		0.1 M Imidazole-HCl pH 8.0	30% (w/v) MPD; 10% (w/v) PEG 4000	+	1	30
90			30% (w/v) MPD; 20% (w/v) Ethanol	-	50	30
91			35% (w/v) MPD			
92		0.1 M Imidazole-HCl pH 8.0	35% (w/v) MPD			
93		0.1 M Tris-HCl pH 8.5	40% (w/v) MPD			
94		0.1 M HEPES sodium salt pH 7.5	47% (w/v) MPD	+	3	30
95			47% (w/v) MPD; 2% (w/v) tert-Butanol			
96			50% (w/v) MPD			

Table G.2: Evaluation of the JCSG+ crystallization screening. Crystals were counted after 24h. ‘+’ refers to a higher crystal number of *LbADH* mutant T102E, ‘-’ refers to higher crystal number of *LbADH* WT. Blank space indicates that neither of the two variants crystallized.

#	Salt	Buffer	Precipitant	+/-	WT crystals	T102E crystals
1	0.2 M lithium sulfate	0.1 M sodium acetate pH 4.5	50 % (v/v) PEG 400	-	15	5
2		0.1 M sodium citrate pH 5.5	20 % (w/v) PEG 3000	+	5	20
3	0.18 M ammonium citrate		20 % (w/v) PEG 3350			
4	0.02 M calcium chloride	0.1 M sodium acetate pH 4.6	30 % (v/v) MPD	+	0	30
5	0.2 M magnesium formate		20 % (w/v) PEG 3350	+	0	40
6	0.2 M lithium sulfate	0.1 M phosphate citrate pH 4.2	20 % (w/v) PEG 1000			
7		0.1 M ches pH 9.5	20 % (w/v) PEG 8000			
8	0.2 M ammonium formate		20 % (w/v) PEG 3350	+	0	10
9	0.2 M ammonium chloride		20 % (w/v) PEG 3350	+	0	40
10	0.2 M potassium formate		20 % (w/v) PEG 3350	+	0	40
11	0.2 M ammonium phosphate	0.1 M TRIS pH 8.5	50 % (v/v) MPD			
12	0.2 M potassium nitrate		20 % (w/v) PEG 3350	+	0	40
13	0.8 M ammonium sulfate	0.1 M citric acid pH 3.5				
14	0.2 M sodium thiocyanate		20 % (w/v) PEG 3350	+	3	30
15		0.1 M bicine pH 8.5	20 % (w/v) PEG 6000			
16		0.1 M HEPES pH 7.5	10 % (w/v) PEG 8000; 8 % (v/v) ethylene glycol			
17		0.1 M cacodylate pH 6.5	40 % (v/v) MPD; 5 % (w/v) PEG 8000	+	10	40
18		0.1 M phosphate citrate pH 4.2	40 % (v/v) ethanol; 5 % (w/v) PEG 1000	+	0	40
19		0.1 M sodium acetate pH 4.6	8 % (w/v) PEG 4000	+	0	15
20	0.2 M magnesium chloride	0.1 M tris pH 7.0	10 % (w/v) PEG 8000	+	0	20
21		0.1 M citric acid pH 4.0	20 % (w/v) PEG 6000	+	0	50
22	0.2 M magnesium chloride	0.1 M cacodylate pH 6.5	50 % (v/v) PEG 200			
23		1.6 M sodium citrate pH 6.5				
24	0.2 M potassium citrate		20 % (w/v) PEG 3350			
25	0.2 M sodium chloride	0.1 M phosphate citrate pH 4.2	20 % (w/v) PEG 8000	+	0	100
26	1.0 M lithium chloride	0.1 M citric acid pH 4.0	20 % (w/v) PEG 6000			
27	0.2 M ammonium nitrate		20 % (w/v) PEG 3350	-	500	100
28		0.1 M HEPES pH 6.5	10 % (w/v) PEG 6000			
29	0.8 M / 0.8 M K/Na phosphate	0.1 M HEPES pH 7.5				
30		0.1 M phosphate citrate pH 4.2	40 % (v/v) PEG 300	+	2	30
31	0.2 M zinc acetate	0.1 M sodium acetate pH 4.5	10 % (w/v) PEG 3000			
32		0.1 M TRIS pH 8.5	20 % (v/v) ethanol			
33		0.1 M K/Na phosphate pH 6.2	25 % (v/v) propanediol; 10 % (v/v) glycerol			
34		0.1 m bicine pH 9.0	10 % (w/v) PEG 20000. 2 % (v/v) 1,4-dioxane			
35	2.0 M ammonium sulfate	0.1 M sodium acetate pH 4.6				
36			10 % (w/v) PEG 1000; 10 % (w/v) PEG 8000	-	1000	50
37			24 % (w/v) PEG 1500; 20 % (w/v) glycerol			
38	0.2 M magnesium chloride	0.1 M HEPES pH 7.5	30 % (v/v) PEG 400			
39	0.2 M sodium chloride	0.1 M K/Na phosphate pH 6.2	50 % (v/v) PEG 200			
40	0.2 M lithium sulfate	0.1 M sodium acetate pH 4.5	30 % (w/v) PEG 8000			
41		0.1 M HEPES PH 7.5	70 % (v/v) MPD			
42	0.2 M magnesium chloride	0.1 M TRIS pH 8.5	20 % (w/v) PEG 8000	+	2	30
43	0.2 M lithium sulfate	0.1 M TRIS pH 8.5	40 % (v/v) PEG 400			
44		0.1 M TRIS pH 8.0	40 % (v/v) MPD			
45	0.17 M ammonium sulfate		25.5 % (w/v) PEG 4000; 15 % (v/v) glycerol			
46	0.2 M calcium acetate	0.1 M cacodylate pH 6.5	40 % (v/v) PEG 300			
47	0.14 M calcium chloride	0.07 M sodium acetate pH 4.6	14 % (v/v) isopropanol; 30 % (v/v) glycerol			
48	0.04 M potassium phosphate		16 % (w/v) PEG 8000; 20 % (v/v) glycerol	-	200	50

Appendices

#	Salt	Buffer	Precipitant	+/-	WT crystals	T102E crystals
49	1.0 M sodium citrate	0.1 M cacodylate pH 6.5				
50	0.2 M sodium chloride; 2.0 M ammonium sulfate	0.1 M cacodylate pH 6.5				
51	0.2 M sodium chloride	0.1 M HEPES pH 7.5	10 % (v/v) isopropanol			
52	0.2 M lithium sulfate; 1.26 M ammonium sulfate	0.1 M TRIS pH 8.5				
53		0.1 M caps pH 10.5	40 % (v/v) MPD			
54	0.2 M zinc acetate	0.1 M imidazole pH 8.0	20 % (w/v) PEG 3000			
55	0.2 M zinc acetate	0.1 M cacodylate pH 6.5	10 % (v/v) isopropanol			
56	1.0 M ammonium phosphate	0.1 M sodium acetate pH 4.5				
57	1.6 M magnesium sulfate	0.1 M MES pH 6.5				
58		0.1 M bicine pH 9.0	10 % (w/v) PEG 6000			
59	0.16 M calcium acetate	0.08 M cacodylate pH 6.5	14.4 % (w/v) PEG 8000; 20 % (v/v) glycerol	+	0	40
60		0.1 M imidazole pH 8.0	10 % (w/v) PEG 8000			
61	0.05 M cesium chloride	0.1 M MES pH 6.5	30 % (v/v) jeffamine m-600	+	5	20
62	3.2 M ammonium sulfate	0.1 M citric acid pH 4.0				
63		0.1 M TRIS pH 8.5	20 % (v/v) MPD			
64		0.1 M HEPES pH 7.5	20 % (v/v) jeffamine m-600			
65	0.2 M magnesium chloride	0.1 M TRIS pH 8.5	50 % (v/v) ethylene glycol			
66		0.1 M bicine pH 8.5	10 % (v/v) MPD			
67		0.8 M succinic acid pH 7.0				
68		2.1 M malic acid pH 7.0				
69		2.4 M sodium malonate pH 7.0				
70	1.1 M sodium malonate	0.1 M HEPES pH 7.0	0.5 % (v/v) jeffamine ed-2001			
71	1.0 M succinic acid	0.1 M HEPES pH 7.0	1 % (w/v) PEG 2000 MME			
72		0.1 M HEPES pH 7.0	30 % (v/v) jeffamine m-600			
73		0.1 M HEPES pH 7.0	30 % (v/v) jeffamine ed-2001			
74	0.02 M magnesium chloride	0.1 M HEPES pH 7.5	22 % (w/v) sodium polyacrylate 5100			
75	0.01 M cobalt chloride	0.1 M TRIS pH 8.5	20 % (w/v) polyvinylpyrrolidone k15			
76		0.1 M TRIS pH 8.5	20 % (w/v) PEG 2000 MME; 0.2 M trimethylamine n-oxide	+	0	40
77	0.005 M cadmium chloride; 0.005 M cobalt chloride; 0.005 M magnesium chloride; 0.005 M nickel chloride	0.1 M HEPES pH 7.5	12 % (w/v) PEG 3350	+	0	20
78		0.24 M sodium malonate pH 7.0	20 % (w/v) PEG 3350	+	0	40
79		0.1 M succinic acid pH 7.0	15 % (w/v) PEG 3350			
80		0.15 M malic acid pH 7.0	20 % (w/v) PEG 3350	+	0	15
81	0.1 M potassium thiocyanate		30 % (w/v) PEG 2000 MME	+	0	30
82	0.15 M potassium bromide		30 % (w/v) PEG 2000 MME	+	0	40
83	2.0 M ammonium sulfate	0.1 M BIS-TRIS pH 5.5				
84	3.0 M sodium chloride	0.1 M BIS-TRIS pH 5.5				
85	0.3 M magnesium formate	0.1 M BIS-TRIS pH 5.5				
86	1.0 M ammonium sulfate	0.1 M BIS-TRIS pH 5.5	1 % (w/v) PEG 3350			
87	0.1 M sodium acetate pH 4.5	0.1 M BIS-TRIS pH 5.5	25 % (w/v) PEG 3350	+	0	40
88	0.2 M calcium chloride	0.1 M BIS-TRIS pH 5.5	45 % (v/v) MPD			
89	0.2 M ammonium acetate	0.1 M BIS-TRIS pH 5.5	45 % (v/v) MPD	+	5	10
90	0.1 M ammonium acetate	0.1 M BIS-TRIS pH 5.5	17 % (w/v) PEG 10000	+	0	30
91	0.2 M ammonium sulfate	0.1 M BIS-TRIS pH 5.5	25 % (w/v) PEG 3350	+	0	50
92	0.2 M sodium chloride	0.1 M BIS-TRIS pH 5.5	25 % (w/v) PEG 3350	+	0	40
93	0.2 M lithium sulfate	0.1 M BIS-TRIS pH 5.5	25 % (w/v) PEG 3350	+	0	20
94	0.2 M ammonium acetate	0.1 M BIS-TRIS pH 5.5	25 % (w/v) PEG 3350	+	0	30
95	0.2 M magnesium chloride	0.1 M BIS-TRIS pH 5.5	25 % (w/v) PEG 3350	+	2	50
96	0.2 M ammonium acetate	0.1 M HEPES pH 7.5	45 % (v/v) MPD			